

POLITECNICO DI TORINO

Corso di Laurea in Nanotechnologies for ICTs

Master Degree Thesis

Refractometric sensing

Comparison between plasmonic and high index dielectric nanoparticles for
refractometric sensing



Supervisor
Prof. Emiliano Descrovi

Candidate
Noemi Bosio
matricola: s244191

Internship Tutor
Chalmers insitute of technology
Prof. Mikael Käll
Staff scientist Ruggero Verre

ANNO ACCADEMICO 2017 – 2018

In this master thesis we performed an unbiased comparison between two sensing platform based on metallic and high index dielectric (HID) nanoparticles.

After a brief introduction, in *Chapter 2* we explain the theory behind the project. We underline the theoretical differences between metallic nanoparticles, which support localized surface plasmon resonances (LSPR) and HID nanoparticles which support the so-called Mie or geometrical resonances. We try then to explain the differences in the optical response of these materials, focusing on the different optical modes excited in the two structures and on the dependences of the resonances on the shape, size and surrounding refractive index. We introduce then the concept of refractometric sensing, of its working principle and of the parameters that we will use to compare the two platforms. We enlight then the differences between the two types of refractometric sensing experiments we performed in this project, bulk and local sensing.

After the introduction of the theoretical and generical concepts needed in this project, in *Chapter 3* we present the experimental methods that have been used. In a first part we focus on the working principle of the different machines and physical process used during the samples' fabrication.

Particular attention is then put in the explanation of the fabrication process, the hole-mask colloidal lithography (HCL), which took place in the cleanroom. The process can be used for the fabrication of both gold and silicon nanodisks, even if some differences in the process are needed, which are enlightened in this chapter.

We describe then the optical and microfluidic setup used for the measurements and the different variables that we decided to track. In the last part of this chapter we describe the experimental protocol used for the bulk and local sensing experiments.

In *Chapter 4* we present the collected data and a discussion of them. We present a separated section for gold and silicon, in which first of all a comparison between different samples of the same material is presented, to conclude with a comparison between the performances of the different materials.

To conclude this master project we present in *Chapter 5* a brief summary and the conclusions we got, underling some possible outlooks and future experiments.

Acknowledgements

I would like to thank Chalmers university of technology, and in particular the bionanophotonics division, where I found kind and nice people always willing to help and to give advices.

I would like to thanks in particular Nils Odebo, wich performed a lot of simulations for me and was always up to help me with my numeoruos theoretical doubts, and Steve Jones who became a dear friend and helped me both when experiments were thought and when life was hard.

I would also like to thank my family which supported me during my studies, and that always believed in me while I was doubting my self. I thank all my friends, in particular Erika Fontana, that spent with me most of the time during these years; without her things would have been more difficult.

For this master's thesis project I aknowledge the support by Politecnico di Torino which gives his student the possibility to study abroad, an experience that I have enjoyed in the good and bad moments.

List of Figures

2.1	Plasmon oscillations.	20
2.2	Extinction, Scattering and Absorption efficiencies in air ($n=1$). a) Gold nanosphere with 50 nm of diameter. b) Silicon nanosphere with 150 nm of diameter.	28
2.3	Ratio between absorption and extinction efficiency. a) Gold nanosphere with 50 nm of diameter. b) Silicon nanosphere with 150 nm of diameter.	29
2.4	Extinction, Scattering and Absorption efficiencies changing the nanosphere diameter, in water ($n \simeq 1.33$). a) Gold nanosphere. b) Silicon nanosphere.	30
2.5	Extinction efficiency in dependency of radius and wavelength in water ($n \simeq 1.33$). a) Gold nanosphere. b) Silicon nanosphere.	30
2.6	Absorption efficiency in dependency of radius and wavelength in water ($n \simeq 1.33$). a) Gold nanosphere. b) Silicon nanosphere.	31
2.7	Extinction, Scattering and Absorption efficiencies changing the refractive index from 1.33 to 1.9. a) Gold nanosphere with 50 nm of diameter. b) Silicon nanosphere with 150 nm of diameter.	31
2.8	Extinction efficiency in dependency of refractive index and wavelength in water ($n \simeq 1.33$). a) Gold nanosphere. b) Silicon nanosphere.	32
2.9	Absorption efficiency in dependency of refractive index and wavelength in water ($n \simeq 1.33$). a) Gold nanosphere. b) Silicon nanosphere.	32
2.10	Extinction, Absorption and Scattering efficiency in water ($n \simeq 1.33$). a) Gold nanodisk with diameter 80 nm and thickness 125 nm b) Silicon nanodisk with diameter 175 nm and thickness 140 nm.	35
2.11	Extinction efficiency increasing refractive index from 1.3 to 1.45. a) Gold nanodisk with diameter 80 nm and thickness 125 nm b) Silicon nanodisk with diameter 175 nm and thickness 140 nm.	35
2.12	a) Dielectric function of gold as a function of wavelength b) Dielectric function of gold as a function of energy. Datas taken from [8].	37
2.13	Real and Imaginary part of the dielectric function [3].	39

2.14	a) Dielectric function of silicon as a function of wavelength b) Dielectric function of silicon as a function of energy. Data taken from [8].	40
2.15	Field patterns for normal modes [3].	41
2.16	a) Gold efficiencies for nanodisks of 150 nm of diameter and 30 nm of thickness. b) Silicon efficiencies for nanodisks of 170 nm of diameter and 144 nm of thickness. For both the spectra we have in yellow the extinction, in blue the absorption and in orange the scattering efficiency. The lines represent the different wavelengths associated to the mode for which the electric field has been calculated.	42
2.17	$ E ^2$ for Gold nanodisk corresponding to the electric dipole mode, calculated for $\lambda = 770 \text{ nm}$ a) Field along the XY plane b) Field along the XZ plane c) field along the YZ plane.	42
2.18	$ E ^2$ for Silicon nanodisk corresponding to the magnetic dipole mode, calculated for $\lambda = 700 \text{ nm}$ a) Field along the XY plane b) Field along the XZ plane c) field along the YZ plane.	43
2.19	$ E ^2$ for Silicon nanodisk corresponding to the electric dipole mode, calculated for $\lambda = 590 \text{ nm}$ a) Field along the XY plane b) Field along the XZ plane c) field along the YZ plane.	43
2.20	$ E ^2$ for Silicon nanodisk corresponding to the magnetic quadrupole mode, calculated for $\lambda = 520 \text{ nm}$ a) Field along the XY plane b) Field along the XZ plane c) field along the YZ plane.	44
3.1	Thickness of the spin coated PMMA A4 film versus spin velocity [4].	48
3.2	Silicon master for microfluidics	53
3.3	Scanning electron microscope schematic [23]	54
3.4	a) Cleaned substrate b) PMMA spin coating c) O_2 plasma etch d) PDDA coating e) PS deposition f) 10 nm Gold deposition g) tape stripping h) O_2 plasma etch i) O_2 PMMA etch j) Metal deposition k) Lift off	57
3.5	Gold nanodisks with diameter 100nm and height 30nm at different magnifications.	57
3.6	Silicon nanodisks with diameter 200nm and height 144nm at different magnifications.	58
3.7	a) Cleaned substrate b) amorphous Si deposition c) Nitrogen annealing d) PMMA spin coating e) O_2 plasma etch f) PDDA coating g) PS deposition h) 10 nm Gold deposition i) tape stripping j) O_2 plasma etch k) O_2 PMMA etch l) Ni deposition m) Lift off n) ICP etching of the poly-Si with Cl o) structure after the etching p) wet etching of the remaining Ni	59
3.8	Optical setup sketch.	60
3.9	Optical setup used for the measurements	61
3.10	Spectrometer schematic	62
3.11	PDMS structure	63
3.12	Left) Gold finished sample Right) Silicon finished sample	64
3.13	Parameters used in the centroid calculation [7].	66
3.14	Refractive indices of aqueous ethylene glycol solutions at 25°C.	67
3.15	a) Resonance peak variation with static flow b) Resonance peak variation with a $20 \frac{\mu\text{l}}{\text{min}}$ flow.	68

3.16	a) Resonance peak variation with $50 \frac{\mu l}{min}$ b) Resonance peak variation with $80 \frac{\mu l}{min}$	69
3.17	Schematic of the protocol used to grow the BSA layer on the samples' surface. From left to right: nanodisk, growth of the first BSA layer, adsorption of DS molecules, growth of the second BSA layer.	70
4.1	a) Extinction spectrum in air of gold nanodisks with diameter 100 nm b) Extinction spectrum in air of gold nanodisks with diameter 150 nm.	72
4.2	a) Extinction spectra of Silicon nanodisks in dependence of the diameter for a thickness of 144 nm b) Extinction spectra of Silicon nanodisks in dependence of the thickness for 170 nm diameter.	73
4.3	Variation of wavelength at which the magnetic and electric dipole modes appear in dependence of the diameter.	74
4.4	a) Gold nanodisk diam=100 nm b) Gold nanodisk diam=150 nm. The blue line represents the spectra in air while the red line represents the spectra in DI water.	75
4.5	a) Gold nanodisk diam=100 nm b) Gold nanodisk diam=150 nm. Variation in time of the resonance peak in dependence of ethylen glicole concentration.	76
4.6	a) Extinction spectra of gold nanodisks with diam=100 nm b) a) Extinction spectra of gold nanodisks with diam=150 nm. c) d) Intensity differencies as a function of time and wavelength.	77
4.7	a) Gold nanodisk diam=100 nm b) Gold nanodisk diam=150 nm. Intensities differences for each wavelength with reduced range.	78
4.8	a) Gold nanodisk diam=100 nm b) Gold nanodisk diam=150 nm. Intensities differences for each wavelength and refractive index variation.	78
4.9	a) Gold nanodisk diam=100 nm b) Gold nanodisk diam=150 nm. Sensitivity calculated at the resonance wavelength.	79
4.10	a) Gold nanodisk diam=100 nm b) Gold nanodisk diam=150 nm. Sensitivity as a function of the wavelength.	80
4.11	Extinction spectra in air and DI water. Blu line spectra in air, red line spectra in DI water. a) Silicon nanodisk d=150 nm b) Silicon nanodisk d=170 nm. c) Silicon nanodisk, d=200 nm.	81
4.12	Variation of intensity when changing refractive index from DI water to different concentrations of ethylen glicole a) Silicon nanodisk d=150 nm b) Silicon nanodisk d=170 nm. c) Silicon nanodisk, d=200 nm.	82
4.13	Variation of intensity when changing refractive index from DI water to different concentrations of ethylen glicole a) Silicon nanodisk d=150 nm b) Silicon nanodisk d=170 nm.	83
4.14	Sensitivity with respect to intensity when changing refractive index from DI water to different concentrations of ethylen glicole a) Silicon nanodisk d=150 nm b) Silicon nanodisk d=170 nm.	84
4.15	Sensitivity with respect to resonance wavelength when changing refractive index from DI water to different concentrations of ethylen glicole a) Silicon nanodisk d=150 nm b) Silicon nanodisk d=170 nm.	85

4.16	Intensities differences with respect to time and wavelength a) Silicon nanodisk d=150 nm b) Silicon nanodisk d=170 nm c) Silicon nanodisk d=200 nm.	86
4.17	Intensities differences with respect to time and wavelength a) Silicon nanodisk d=150 nm b) Silicon nanodisk d=170 nm c) Silicon nanodisk d=200 nm.	87
4.18	Sensitivity defined as $\frac{\Delta I}{\Delta n}$ for each wavelength a) Silicon nanodisk d=150 nm b) Silicon nanodisk d=170 nm c) Silicon nanodisk d=200 nm. Disk height = 144 nm.	88
4.19	Sensitivity defined as $\frac{\Delta I}{\Delta n}$ calculated at λ_{res} a) Silicon nanodisk d=150 nm b) Silicon nanodisk d=170 nm. Disk height = 200 nm.	89
4.20	Sensitivity defined as $\frac{\Delta \lambda}{\Delta n}$ calculated at λ_{res} a) Silicon nanodisk d=150 nm b) Silicon nanodisk d=170 nm. Disk height = 200 nm.	89
4.21	Sensitivity defined as $\frac{\Delta I}{\Delta n}$ for each wavelength a) Silicon nanodisk d=150 nm b) Silicon nanodisk d=170 nm. Disk height = 200 nm.	90
4.22	Shift of the lowest energy resonance peak as a function of time, when growing different BSA layers. The number of steps corresponds to the number of grown layers. a) Gold nanodisk d=150 nm b) Silicon nanodisk d=170 nm, disk height = 200 nm.	92
4.23	Exponential fit of the resonance peak wavelength as a function of number of BSA layers. a) Gold nanodisk d=150 nm b) Silicon nanodisk d=170 nm, disk height = 200 nm.	93

List of Tables

Gold nanodisks	80
Silicon nanodisks with thickness 144 nm	90
Silicon nanodisks with thickness 200 nm	90

Contents

List of Figures	7
List of Tables	12
1 Introduction	16
1.1 Refractometric sensing	16
1.2 Plasmonic and high index dielectric	17
1.3 Purpose and aim	17
2 Theory	19
2.1 Localized surface plasmon resonance	20
2.2 Mie theory	21
2.2.1 Maxwell's equations	21
2.2.2 Absorption and Scattering	24
2.2.3 Absorption and Scattering by a sphere	26
2.2.4 Quasi-static approximation	33
2.2.5 Ellipsoid in the electrostatic approximation	33
2.3 Dielectric function	36
2.3.1 Gold dielectric function: Drude model	36
2.3.2 Silicon dielectric function: Lorentz model	38
2.4 Mode analysis and near field	41
2.5 Refractometric sensing	45
3 Experimental methods	47
3.1 Fabrication	47
3.1.1 Spin coating	48
3.1.2 Evaporation	49
3.1.3 Oxygen plasma etching	49
3.1.4 ICP etching	51
3.1.5 Wet chemical etching	52

3.1.6	Cryo etching	52
3.1.7	SEM	53
3.1.8	HCL process	56
3.2	Measurements procedure and setup	60
3.2.1	Microfluidic	63
3.3	Transient measurements	65
3.3.1	Resonance wavelength and Intensity	65
3.3.2	Bulk sensing: experimental procedure	67
3.3.3	Bio-sensing: experimental procedure	70
4	Results and discussion	71
4.1	Extinction spectra	72
4.1.1	Extinction spectra of Gold	72
4.1.2	Extinction spectra of Silicon	73
4.2	Bulk sensing	75
4.2.1	Gold	75
4.3	Silicon	81
4.4	Local sensing	92
5	Conclusion and outlook	95
5.0.1	Summary and conclusions	95
5.0.2	Outlooks	96

CHAPTER 1

Introduction

In nowadays life sensing has gained a lot of importance since it has become more and more important to check on the purity or on the contamination level of different things. There are many fields in which sensing can be a useful instrument: it can be used for environmental control, to check on the purity of air or water, it can be used in agriculture or food industry, it can be used in the biomedical industry to obtain a fast diagnosis tool. There are many different types of sensors based on the use of nanoparticles, and the main difference between them is in the transduction system they use.

Mainly, we can have mechanical, electrical or optical transduction. In this project we will focus on optical nanosensors, an on the different technologies that can be used in this sense.

1.1 Refractometric sensing

A particular kind of optical sensing is refractometric sensing. This is a surface sensitive technique which detects variations in the refractive index of the sensor's surrounding medium through an optical readout. This is a very powerful technique since it allows for label-free sensing and for real time detection. Label-free detection is usefull since it eliminates the need to manipulate the solution before the experiment. This kind of detection is then easier and do not suffer of quenching problems. Anyway labels can be used in a second moment to enhance the signal collection. Real time detection is also an important requirement in biological sensing. In this way real time data on the binding event can be collected. This is possible since in refractometric sensing the variations in a physical property of the system are tracked.

1.2 Plasmonic and high index dielectric

One of the widely used platform for refractometric sensing is based on metallic nanoparticles. These kind of nanoparticles support plasmons. Plasmons are excitation of the conduction electrons of the metal coupled with the incident electromagnetic wave. Due to the restoring force feeled by the plasma a resonance can occur [19]. These resonances change when the surrounding refractive index changes, translating in energy (or wavelength). The problems of this kind of materials, is that at optical frequencies they have a finite conductivity which leads to energy dissipation, which manifests in heating [17]. Heating can be often detrimental; it can lead to a reshape of the nanoparticles or to its distruction. Furthermore, it can be a huge problem when we talk about bio-sensing, since the behaviour of the molecules we're studying can significantly change with temperature. To overcome this problem, recently, high index dielectric materials [18] have been proposed for sensing purposes. These kind of materials has reached high interest for metamaterial research since in these materials electric and magnetic multipolar resonances have been observed, which lead to a possible enhancement of the magnetic field, difficult to achieve in plasmonic structures, due to the electric dipole nature of the resonances [28][15]. In the last years different kind of sensor based on these materials, in particular silicon, have been studied [11] [30] [22]. Anyway this is still a young research field and despite encouraging results more experiments are needed.

1.3 Purpose and aim

The purpose of this project is to provide an unbiased comparison between two sensing platforms based on these two different kind of materials, which exploit different physical properties. Among the possible materials we chose gold and silicon. This because these materials are the one exploiting the best optical properties in plasmonic and high index dielectric fields respectively.

Since there are not much data related to HID used for sensing, and since we want to understand if this sensing platform can be a good alternative to the well known plasmonic one, we decided to perform this comparison in the easiest possible way, to provide an experiment easily reproducible.

We decided then to use one of the easiest geometry to study and to fabricate: nanodisks. For the same reason, the measurements were obtained with a transmission optical setup. The aim is to find positive results that would open the way to further possible experiments, to overcome the problems linked to plasmonic-based sensors.

CHAPTER 2

Theory

In this chapter we will go through the theory that has been involved in this project. With the intention to compare two different kind of materials, which exploit different properties, we will briefly explain the principles of Localized surface plasmon resonance, a property typical of metals, and then we will try to describe the Mie theory, a theory which can describe the behaviour of both conductors and insulators.

Simulations' results will be provided together with the theory.

The differences between these materials are then briefly described in terms of differences in their optical properties.

We will then describe how refractometric sensing works, and the differences between bulk and local sensing.

2.1 Localized surface plasmon resonance

Localized surface plasmon is the result of the interaction between light and the free electrons present in a metal particle. When a metal particle smaller than the wavelength of light is shone, the free electrons cloud starts to oscillate, driven by the incident electric field and a plasmon resonance occurs.

When the electrons clouds starts to oscillate, it will feel a restoring force due to the positive ion lattice of the particle, due to Coulomb attraction. A simple schematic can be seen in fig. 2.1. Taking at first into consideration a small sphere, with radius $r \ll \lambda$, we can

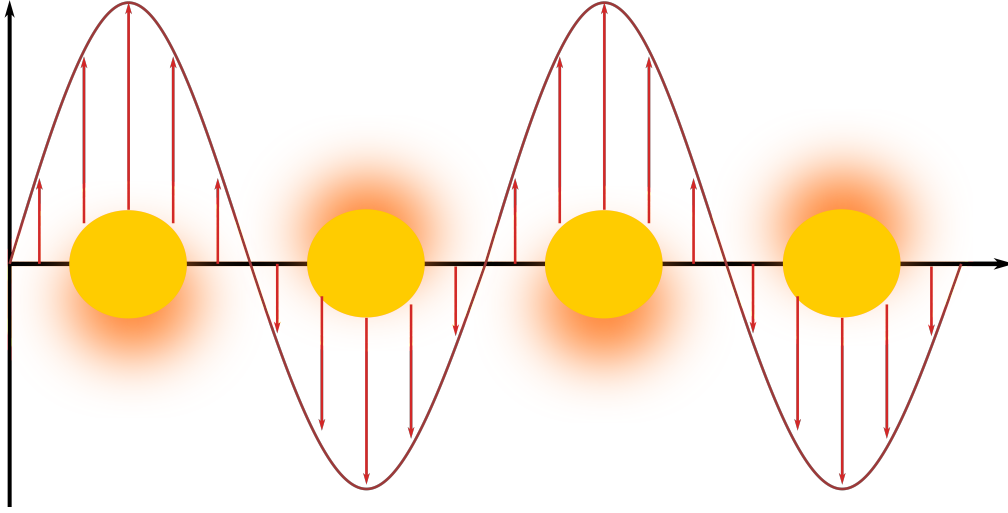


Figure 2.1: Plasmon oscillations.

use the so called quasi-static approximation to describe this phenomenon. If the particle is subjected to an incident electric field $E_0 = E_0 e^{-i\omega t}$ the induced dipole moment of the sphere will be:

$$P = \epsilon_0 \epsilon_d \alpha E_0 \quad (2.1)$$

where α represents the polarizability function of the sphere, given by:

$$\alpha = 4\pi r^3 \frac{\epsilon_m - \epsilon_d}{\epsilon_m + 2\epsilon_d} \quad (2.2)$$

In these equations ϵ_0 is the vacuum permittivity, ϵ_d represents the dielectric function of the particle's surrounding environment, ϵ_m is the dielectric function of the metal. A strong interaction between the electromagnetic field of LSPR and the incident wave, a resonance, will occur when the denominator of the polarizability is minimized, so when the so called *Fröhlich condition* is matched. In a spherical particle, this occur when

$$\epsilon_m(\lambda) = -2\epsilon_d \quad (2.3)$$

When the nanoparticle has a different shape, but the dimensions are such that we can consider the quasi-static approximation, what changes is the polarizability in equation 2.2. If we consider a disk, so an elongated particle, it turns out that the resonance is red shifted. This is due to the fact that changing the particle's shape, the restoring force from the lattice will also change. This force will be reduced along the elongated axis, which translates in a resonance occurring at a longer wavelength. For a spheroid the polarizability results to be:

$$\alpha = 4\pi abc \frac{\epsilon_m - \epsilon_d}{3\epsilon_d + 3L(\epsilon_m - \epsilon_d)} \quad (2.4)$$

where again ϵ_m is the permittivity of the particle and ϵ_d is the permittivity of the surrounding medium.

In the latter equation L represents the form factor, which changes in dependence on the illumination direction. If the applied field is parallel to the semi axis c of the spheroid, the form factor will be:

$$L = L_3 = \frac{abc}{2} \int_0^\infty \frac{dq}{(c^2 + q)f(q)} \quad (2.5)$$

Our structure is a so called oblate spheroid, a disk, so in this particular case $a = b$ [19].

2.2 Mie theory

When we are dealing with dielectrics nanoparticles, instead that metallic one, we need a different theory to describe the interaction with light. Dielectrics in fact, do not have free electrons, so the reason of the appearance of resonances cannot be due to LSPR.

The solution of Maxwell's equations provided by Gustav Mie, describes the scattering of an electromagnetic wave by an homogeneous sphere. The theory has then been extended to different particle's shapes.

2.2.1 Maxwell's equations

As we said Mie theory presents a solution of Maxwell's equations, to describe scattering and absorption by a particle when shone with an incident wave.

To describe the solution we'll start from the same point.

$$\nabla \cdot D = \rho_F \quad (2.6)$$

$$\nabla \times E + \frac{\partial B}{\partial t} = 0 \quad (2.7)$$

$$\nabla \cdot B = 0 \quad (2.8)$$

$$\nabla \times H = J_F + \frac{\partial D}{\partial t} \quad (2.9)$$

where E is the electric field and B is the magnetic induction. The electric displacement D and the magnetic field H are defined as:

$$D = \epsilon_0 E + P \quad (2.10)$$

$$H = \frac{B}{\mu_0} - M \quad (2.11)$$

where P is the electric polarization and M the magnetization, while ϵ_0 and μ_0 represents the free space permittivity and permeability respectively.

The charge density and current density, ρ_F and J_F , are associated with the free charges. To have a complete picture we still need some constitutive relations. The current density is defined as:

$$J_F = \sigma E \quad (2.12)$$

And last, we need a relation for the electric polarizability and for the magnetic induction:

$$P = \epsilon_0 \chi E \quad (2.13)$$

$$B = \mu H \quad (2.14)$$

Where σ , μ and χ represent respectively the conductivity, the permeability and the electric susceptibility. These three values depend on the medium that is being considering, but in this work will be assumed independent on the fields, position and direction, which means that the medium is considered linear, homogeneous and isotropic.

However they depend on the frequency. These values in fact, represent the response of the material to the electromagnetic field, and the response of a mechanical system to a periodic driving force is sensitive to the frequency.

The general form for a time harmonic field is given by:

$$E = A \cos \omega t + B \sin \omega t \quad (2.15)$$

which can be written as $E = \text{Re}\{E_c\}$ where

$$E_c = C e^{-i\omega t} \quad (2.16)$$

and

$$C = A + iB \quad (2.17)$$

Substituting (2.12)-(2.14) into (2.6)-(2.9) we obtain:

$$\nabla \cdot (\epsilon E_c) = 0 \quad (2.18)$$

$$\nabla \times E_c = i\omega \mu H_c \quad (2.19)$$

$$\nabla \cdot H_c = 0 \quad (2.20)$$

$$\nabla \times H_c = -i\omega \epsilon E_c \quad (2.21)$$

where ϵ is the complex permittivity defined as:

$$\epsilon = \epsilon_0(1 + \chi) + i \frac{\sigma}{\omega} \quad (2.22)$$

Both the conductivity and the susceptibility contribute to the imaginary part of the permittivity:

$$\text{Im}\{\epsilon\} = \text{Im}\{\chi\} + \text{Re}\{\sigma/\omega\} \quad (2.23)$$

When the imaginary part of the permittivity is nonzero, this translates in absorption of the electromagnetic wave in the medium. Equations from (2.18)-(2.22) will be the starting point for scattering problems. From now on the subscript c , for the complex field, will be omitted.

We'll look now at plane-wave solutions to the Maxwell's equations. We start from electromagnetic plane waves:

$$E_c = E_0 e^{ik \cdot x - i\omega t} \quad (2.24)$$

$$H_c = H_0 e^{ik \cdot x - i\omega t} \quad (2.25)$$

where the wave vector k is assumed to be complex

$$k = k' + ik'' \quad (2.26)$$

Substituting the complex wave vector we find:

$$E_c = E_0 e^{-k'' \cdot x} e^{ik' \cdot x - i\omega t} \quad (2.27)$$

$$H_c = H_0 e^{-k'' \cdot x} e^{ik' \cdot x - i\omega t}$$

where $E_c = E_0 e^{-k'' \cdot x}$ and $H_c = H_0 e^{-k'' \cdot x}$ are the amplitudes of the electric and magnetic field, while $\phi = k' \cdot x - i\omega t$ represents the phase of the wave. If we study the propagation of a constant phase surface in a time interval Δt we'll find that it will move of a distance Δz :

$$k' z - \omega t = k' (z + \Delta z) - \omega (t + \Delta t) = \phi \quad (2.28)$$

Thus the phase velocity results in:

$$v = \frac{\Delta z}{\Delta t} = \frac{\omega}{k'} \quad (2.29)$$

For plane waves the Maxwell's equations are:

$$k \cdot E_0 = 0 \quad (2.30)$$

$$k \cdot H_0 = 0 \quad (2.31)$$

$$k \times E_0 = \omega \mu H_0 \quad (2.32)$$

$$k \times H_0 = -\omega \epsilon E_0 \quad (2.33)$$

From equations (2.30) and (2.31) we understand that the wave vector k is perpendicular both to E_0 and H_0 , while from (2.32) and (2.33) it's clear that E_0 and H_0 are perpendicular. Taking the vector product on both side of (2.32) with k as:

$$k \times (k \times E_0) = \omega \mu k \times H_0 = -\omega^2 \epsilon \mu E_0 \quad (2.34)$$

and from the vector identity:

$$A \times (B \times C) = B(A \cdot C) - C(A \cdot B) \quad (2.35)$$

with equation (2.30) we find:

$$k \cdot k = \omega^2 \epsilon \mu \quad (2.36)$$

From this analysis we understood that planes waves satisfy Maxwell's equations when k , E_0 and H_0 are perpendicular and that the wave vector satisfy eq. (2.36).

The latter equation requires that:

$$k = k' + ik'' = \frac{\omega N}{c} \quad (2.37)$$

where c is the speed of light in free space while N is the complex refractive index expressed as:

$$N = c\sqrt{\epsilon\mu} = \sqrt{\frac{\epsilon\mu}{\epsilon_0\mu_0}} \quad (2.38)$$

which can also be written as:

$$N = n + ik \quad (2.39)$$

where both n and k are non negative. The imaginary part of the refractive index tell us how a wave is attenuated propagating through a medium, while the real part determines the phase velocity.

2.2.2 Absorption and Scattering

Now that we have find a solution for the Maxwell's equations we can set the problem. What we want is to find the electromagnetic field at all points, both in the particle and in its surrounding medium. The field inside the particle will be denoted by (E_1, H_1) , while the field in the surrounding medium (E_2, H_2) , will be the superposition of the incident and scattered field, respectively (E_i, H_i) and (E_s, H_s) :

$$\begin{aligned} E_2 &= E_i + E_s \\ H_2 &= H_i + H_s \end{aligned} \quad (2.40)$$

The fields must satisfy Maxwell's equation in all points where ϵ and μ are continuous. Taking the curl of the third and fourth Maxwell's equation we get:

$$\nabla \times (\nabla \times E) = i\omega\mu\nabla \times H = \omega^2\epsilon\mu E \nabla \times (\nabla \times H) = -i\omega\mu\nabla \times E = \omega^2\epsilon\mu H \quad (2.41)$$

that, when using the vector identity

$$\nabla \times (\nabla \times A) = \nabla(\nabla \cdot A) - \nabla \cdot (\nabla A) \quad (2.42)$$

results is

$$\nabla^2 E + k^2 E = 0, \nabla^2 H + k^2 H = 0 \quad (2.43)$$

where

$$k^2 = \omega^2\epsilon\mu, \nabla^2 A = \nabla \cdot (\nabla A) \quad (2.44)$$

So E and H satisfy Maxwell's equation.

Since we are considering a particle immersed in a medium, when crossing the boundaries between the particle and the surrounding medium there will be a sudden change in ϵ and μ . We need then to impose some boundary conditions on the fields:

$$[E_2(x) - E_1(x)] \times \hat{n} = 0 [H_2(x) - H_1(x)] \times \hat{n} = 0 \quad (2.45)$$

where \hat{n} is the normal to the surface of the particle.

These boundary conditions require that the tangential components of the fields are continuous.

Due to the linearity of Maxwell's equations and to the boundary conditions we find that if E_a and E_b are solutions to the field equations also their sum, $E_a + E_b$ will be a solution. We now suppose that one or more particles are shone by an electromagnetic field, and we denote by U the rate at which the electromagnetic energy is received by a detector. The power received when the particles are not present is U_0 and we'll have $U_0 > U$. The incident beam is exinted by the presence of the particles. Supposing that the surrounding medium is non absorbing the difference between U_0 and U will be given by absorption and scattering in/by the particles. The extinction depends by different factor among which the shape and, the size and the chemical composition of the particles and by the surrounding medium.

We'll consider now the extinction by a single particle in a non absorbing surrounding medium. The net rate at which the surface A is crossed by the electromagnetic energy will be given by:

$$W_a = - \int_A S \cdot \hat{e}_r dA \quad (2.46)$$

where r is the radius of an imaginary sphere surrounding the particle. Since we are considering a non absorbing medium, this will correspond to the energy absorbed in the considered sphere. W_a is > 0 since otherwise, this would lead to the conclusion that energy is being created crossing the sphere. The rate of absorbed energy can be written as the sum of three terms:

$$W_a = W_i - W_s + W_{ext} \quad (2.47)$$

where:

$$W_i = - \int_A S_i \cdot \hat{e}_r dA, W_s = - \int_A S_s \cdot \hat{e}_r dA, W_{ext} = - \int_A S_{ext} \cdot \hat{e}_r dA \quad (2.48)$$

For non absorbing medium W_i vanishes, while W_s represents the rate at which energy is scattered accross the surface of the sphere. From these considerations we understand that W_{ext} is the sum of the absorption and scattering energy rate.

$$W_{ext} = W_s + W_a \quad (2.49)$$

After some algebraic manipulation we find that:

$$W_{ext} = I_i \frac{4\pi}{k^2} Re \{ (X \cdot \hat{e}_x)_{\theta=0} \} \quad (2.50)$$

where I_i represents the incident irradiance. If we take the ratio between the extinction energy rate and the irradiance we find a quantity with the dimensions of an area:

$$C_{ext} = \frac{W_{ext}}{I_i} \quad (2.51)$$

It follows that

$$C_{ext} = C_{sca} + C_{abs} \quad (2.52)$$

For all these terms, extinction, absorption and scattering we can define dimensionless quantity, efficiencies, defined as:

$$Q_{ext} = \frac{C_{ext}}{G}, Q_{sca} = \frac{C_{sca}}{G}, Q_{abs} = \frac{C_{abs}}{G} \quad (2.53)$$

where G represents the area projected by the particle onto a plane perpendicular to the incident beam. For a sphere G is equal to πr^2 .

2.2.3 Absorption and Scattering by a sphere

Mie theory present an analytical solution for a sphere of radius r and refractive index n . In the previous subsection we have seen that the electromagnetic field must satisfy the wave equation, and be divergence free. We have also seen that the electric and magnetic field are not independent. If we suppose to have a scalar function ψ and a constant vector c we can build a vector function M as:

$$M = \nabla \times (c\psi) \quad (2.54)$$

where $\nabla \cdot M = 0$. Using some vector identities we can obtain:

$$\nabla^2 M + k^2 M = \nabla \times [c(\nabla^2 \psi + k^2 \psi)] \quad (2.55)$$

which means that M satisfy the wave equation if ψ is a solution to the scalar wave equation

$$\nabla^2 \psi + k^2 \psi = 0 \quad (2.56)$$

If we build M from another vector function we may write:

$$N = \frac{\nabla \times M}{k} \quad (2.57)$$

which has zero divergence, so also N satisfy the wave equation and we also have that

$$\nabla \times N = kM \quad (2.58)$$

We have in this way, two vector function with all the properties of an electromagnetic field. We have moved the problem to find the solutions to the field equations, to find the solutions to the scalar wave equation. Since we are now looking for solutions to the scattering due to a sphere, the function ψ is chosen to satisfy the wave equation in spherical coordinates r, θ, ϕ . M is taken as:

$$M = \nabla \times (r\psi) \quad (2.59)$$

the scalar wave equation in spherical coordinates is

$$\frac{1}{r^2} \frac{\partial}{\partial r} \left(r^2 \frac{\partial \psi}{\partial r} \right) + \frac{1}{r^2 \sin \theta} \frac{\partial}{\partial \theta} \left(\sin \theta \frac{\partial \psi}{\partial \theta} \right) + \frac{1}{r^2 \sin^2 \theta} \frac{\partial^2 \psi}{\partial \phi^2} + k^2 \psi = 0 \quad (2.60)$$

The solutions we look for are of the form

$$\psi(r, \theta, \phi) = R(r)\Theta(\theta)\Phi(\phi) \quad (2.61)$$

That if substituted in (2.60) leads to three different equations. Solutions to these equations are spherical Bessel functions of first and second kind. The generating functions that satisfy the scalar wave equations can be written as:

$$\psi_{emn} = \cos m\phi P_n^m(\cos\theta) z_n(kr) \quad (2.62)$$

$$\psi_{omn} = \sin m\phi P_n^m(\cos\theta) z_n(kr) \quad (2.63)$$

where z_n is one of the four spherical Bessel functions.

The vector spherical harmonics that are generated by these functions are:

$$\begin{aligned} M_{emn} &= \nabla \times (r\psi_{emn}), N_{emn} = \frac{\nabla \times M_{emn}}{k} \\ M_{omn} &= \nabla \times (r\psi_{omn}), N_{omn} = \frac{\nabla \times M_{omn}}{k} \end{aligned} \quad (2.64)$$

We need now to expand in spherical harmonics the incident plane wave, which results in:

$$E_i = \sum_{n=1}^{\infty} (B_{oln} M_{oln} + A_{eln} N_{eln}) \quad (2.65)$$

After quite a while of mathematics to identify A_{eln} and B_{oln} the plane wave expansion results:

$$E_i = E_0 \sum_{n=1}^{\infty} i^n \frac{2n+1}{n(n+1)} (M_{oln} - iN_{eln}) \quad (2.66)$$

Taking the curl of the electric field we can find as well the expansion in spherical harmonics of the magnetic field. The same expansion can be done for the scattered and internal field. Imposing some boundary conditions, we find that the electric and magnetic field generated inside the sphere can be written as:

$$\begin{aligned} E_1 &= \sum_{n=1}^{\infty} E_n (c_n M_{oln} - i d_n N_{eln}) \\ H_1 &= \frac{-k_1}{\omega \mu_1} \sum_{n=1}^{\infty} E_n (d_n M_{eln} - i c_n N_{oln}) \end{aligned} \quad (2.67)$$

While the scattered electric and magnetic field result in:

$$\begin{aligned} E_s &= \sum_{n=1}^{\infty} E_n (i a_n N_{eln} - b_n M_{oln}) \\ H_s &= \frac{k}{\omega \mu} \sum_{n=1}^{\infty} E_n (i b_n N_{oln} + a_n M_{eln}) \end{aligned} \quad (2.68)$$

For each n we have four coefficients that act as weight for the spherical harmonics. For each n then, we need four equations that can be obtained from the boundary conditions. Solving these equations we can find the coefficients related to the internal field:

$$\begin{aligned} c_n &= \frac{\mu_1 j_n(x) [x h_n(x)]' - \mu_1 h_n(x) [x j_n(x)]'}{\mu_1 j_n(mx) [x h_n(x)]' - \mu_1 h_n(x) [m x j_n(x)]'} \\ d_n &= \frac{\mu_1 m j_n(x) [x h_n(x)]' - \mu_1 h_n(x) [x j_n(x)]'}{\mu_1 m^2 j_n(mx) [x h_n(x)]' - \mu_1 h_n(x) [m x j_n(x)]'} \end{aligned} \quad (2.69)$$

and the ones related to the scattered field:

$$\begin{aligned}
 a_n &= \frac{\mu m^2 j_n(mx) [x j_n(x)]' - \mu_1 j_n(x) [m x j_n(mx)]'}{\mu m^2 j_n(mx) [x h_n(x)]' - \mu_1 h_n(x) [m x j_n(x)]'} \\
 b_n &= \frac{\mu_1 j_n(mx) [x j_n(x)]' - \mu_1 j_n(x) [m x j_n(mx)]'}{\mu_1 j_n(mx) [x h_n(x)]' - \mu h_n(x) [m x j_n(mx)]'}
 \end{aligned} \tag{2.70}$$

When one of the denominator tend to be very small, for some n , the corresponding normal mode will dominate.

Doing the same analysis as in the previous subsection, we can calculate the different energy rates, to obtain the various cross sections. What we obtain is:

$$\begin{aligned}
 C_{sca} &= \frac{2\pi}{k^2} \sum_{n=1}^{\infty} (2n+1) (|a_n|^2 + |b_n|^2) \\
 C_{ext} &= \frac{2\pi}{k^2} \sum_{n=1}^{\infty} (2n+1) Re \{a_n + b_n\}
 \end{aligned} \tag{2.71}$$

Now that we have found the expressions for the different cross sections, we have performed some simulations, to better understand what to expect from the experiments. These first simulations were performed using an open source code [21],[20], that has been modified to get the parameters we were interested in.

First of all we plotted the different efficiencies for both Gold and Silicon, which can be seen in fig. 2.2.

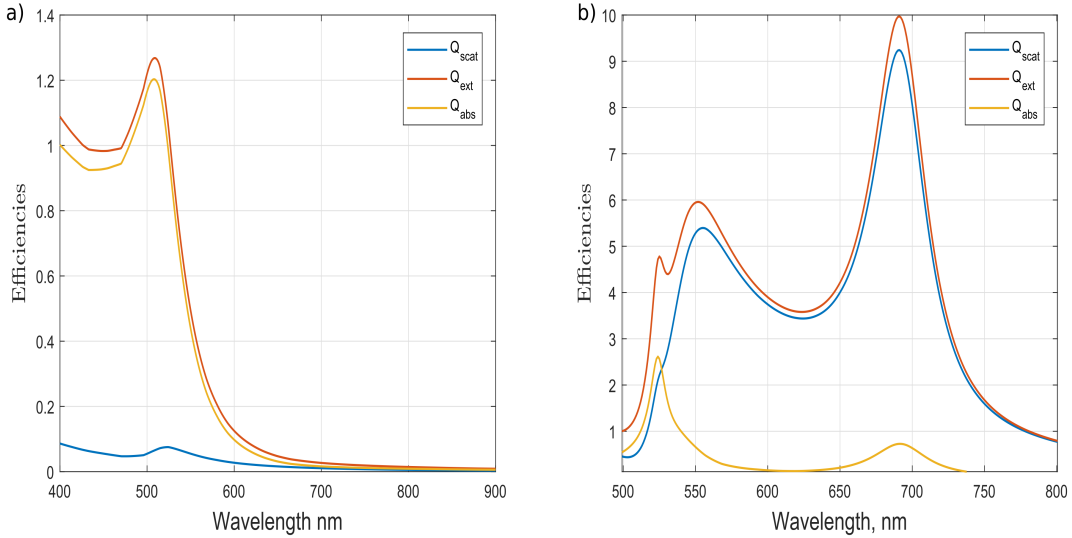


Figure 2.2: Extinction, Scattering and Absorption efficiencies in air ($n=1$). a) Gold nanosphere with 50 nm of diameter. b) Silicon nanosphere with 150 nm of diameter.

As we can see, the spectra looks quite different. We notice that the two materials present a different number of peaks. We also can see that the efficiency that dominates is different in the two cases: in Gold we have a strong predominance of the absorption while in Silicon what prevails is scattering. As said before, one of the reason to compare Gold and Silicon nanoparticles for sensing purposes, is that metallic nanoparticles supporting plasmons present high losses, linked to absorption. In fig. 2.3 we can see the ratio between the absorption and the extinction efficiency.

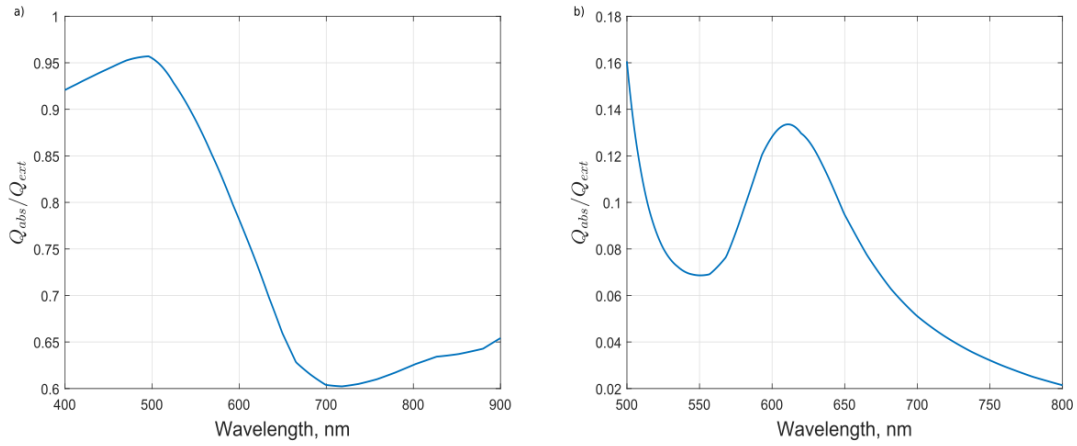


Figure 2.3: Ratio between absorption and extinction efficiency. a) Gold nanosphere with 50 nm of diameter. b) Silicon nanosphere with 150 nm of diameter.

This ratio tells us how much of the incident light is absorbed by the particle, which means, how much of the light goes into dissipation. As we can see this value for Silicon is much smaller with respect to gold.

Following Mie theory we understood that the efficiencies depend both on the size and on the refractive index of the surrounding medium. We wanted to see how a variation of these parameters change the spectra. In fig. 2.4 we can see the extinction dependency on the diameter of the sphere.

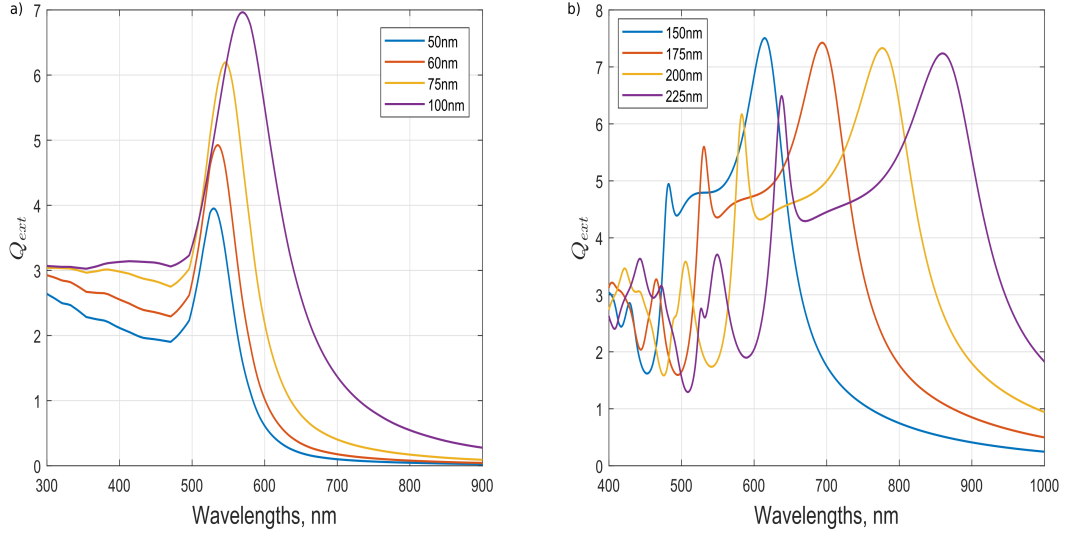


Figure 2.4: Extinction, Scattering and Absorption efficiencies changing the nanosphere diameter, in water ($n \simeq 1.33$). a) Gold nanosphere. b) Silicon nanosphere.

As expected the spectra changes.

Increasing the diameter we notice a red shift and a variation of the intensity related to the peaks. For a better understanding we can look at how the extinction and the absorption varies in dependency of both diameter and refractive index. This can be seen in fig. 2.5 and 2.6 respectively.

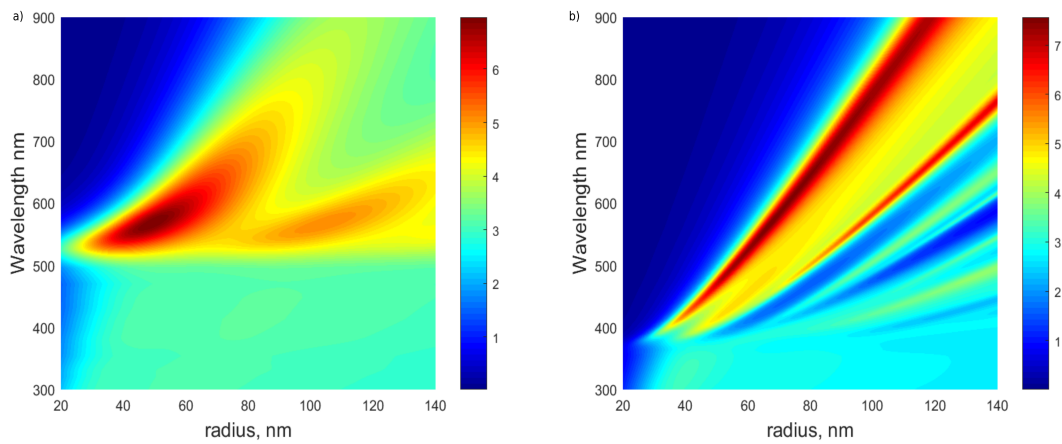


Figure 2.5: Extinction efficiency in dependency of radius and wavelength in water ($n \simeq 1.33$). a) Gold nanosphere. b) Silicon nanosphere.

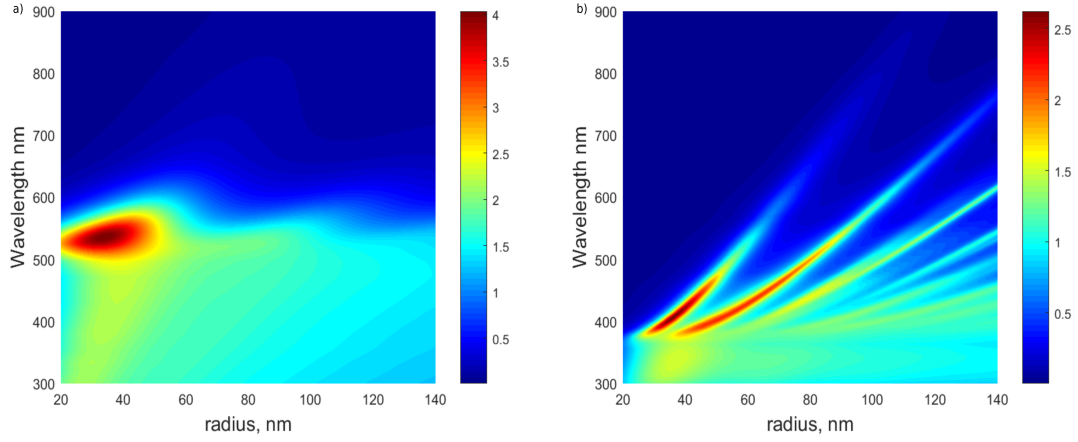


Figure 2.6: Absorption efficiency in dependency of radius and wavelength in water ($n \simeq 1.33$). a) Gold nanosphere. b) Silicon nanosphere.

In this way we easily summarize the differences in the efficiencies of the two materials when increasing the diameter of the nanosphere.

What we are more interested in for sensing purposes, is the variations of the spectra when changing the surrounding refractive index.

In fig. 2.7 we can see this dependency.

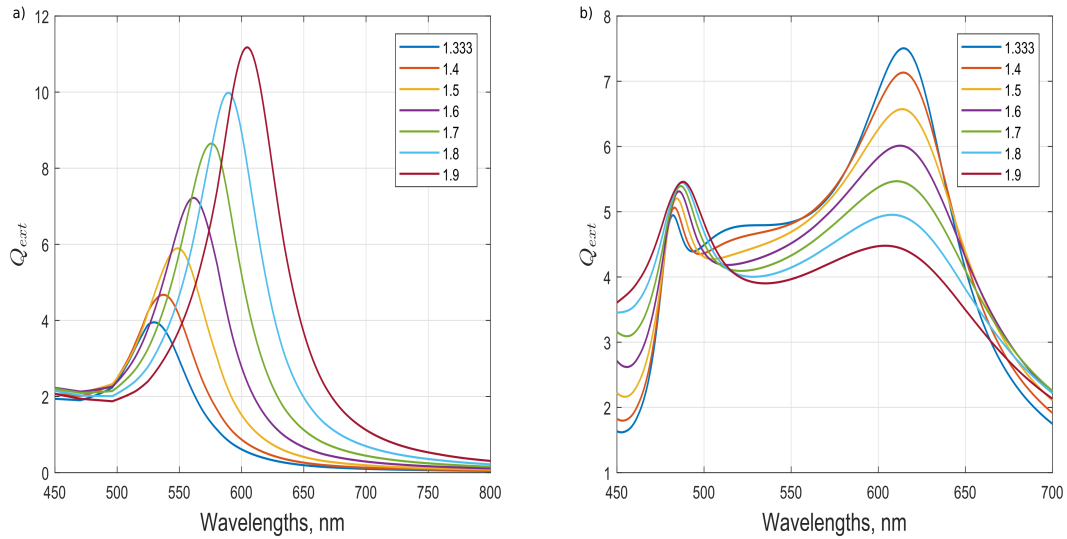


Figure 2.7: Extinction, Scattering and Absorption efficiencies changing the refractive index from 1.33 to 1.9. a) Gold nanosphere with 50 nm of diameter. b) Silicon nanosphere with 150 nm of diameter.

Increasing the refractive index of the surrounding medium we notice a different behaviour for the two materials. Gold nanospheres present a red shift of the extinction together with an increase of the intensity. In Silicon instead, the situation seems more

complicated and we see a different behaviour linked to different peaks. When we look at the lowest energy (highest wavelength) peak, the increase in the refractive index leads to a decrease in intensity, while a clear shift of the resonance wavelength cannot be observed. If we look instead at the highest energy (lowest wavelength) peak, the intensity increases increasing the refractive index, and we also see a red shift of the peak. As we have done before, we can plot the variations in extinction and absorption in dependency of both wavelength and refractive index.

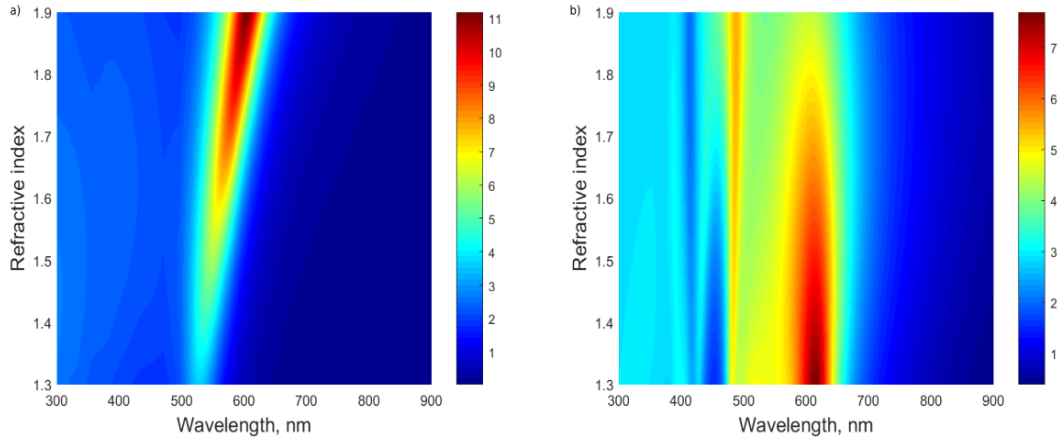


Figure 2.8: Extinction efficiency in dependency of refractive index and wavelength in water ($n \simeq 1.33$). a) Gold nanosphere. b) Silicon nanosphere.

In gold we notice a red shift of the resonance peak and an increase of the intensity while increasing the surrounding refractive index, while for Silicon the fundamental mode seems to not have a shift and presents a decrease of the intensity.

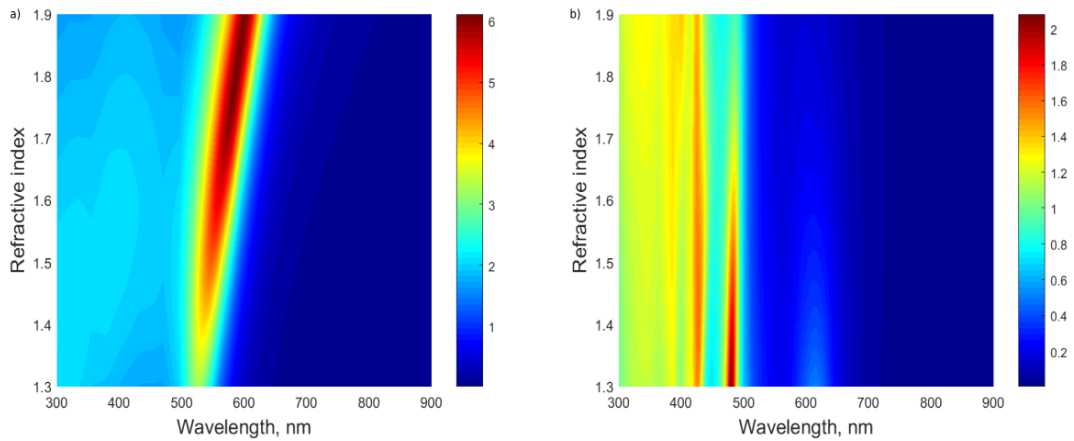


Figure 2.9: Absorption efficiency in dependency of refractive index and wavelength in water ($n \simeq 1.33$). a) Gold nanosphere. b) Silicon nanosphere.

2.2.4 Quasi-static approximation

If we are dealing with small spheres compared to the wavelength of the incident field, the Bessel functions and then the relative coefficients can be expanded in power series. We can consider just the first few terms, obtaining an accuracy of x^6 . Under these conditions the absorption and scattering efficiencies can be written as:

$$\begin{aligned} Q_{abs} &= 4x \operatorname{Im} \frac{\epsilon_m - \epsilon_d}{\epsilon_m + 2\epsilon_d} \\ Q_{sca} &= \frac{8}{3} x^4 \left| \frac{\epsilon_m - \epsilon_d}{\epsilon_m + 2\epsilon_d} \right|^2 \end{aligned} \quad (2.72)$$

Our sphere can be considered as immersed in a static electric field. The sphere and the surrounding medium have a different permittivity, which means that a charge will form on the sphere surface. The field outside the sphere will be, therefore, given by the superposition of the applied field and the field generated by an ideal dipole at the origin of the sphere. This dipole will have a dipole moment:

$$p = 4\pi\epsilon_d r^3 \frac{\epsilon_m - \epsilon_d}{\epsilon_m + 2\epsilon_d} E_0 \quad (2.73)$$

Which tell us that the applied field induce a dipole proportional to the field itself. The dipole moment can be also written as:

$$p = \epsilon d \alpha E_0 \alpha = 4\pi r^3 \frac{\epsilon_m - \epsilon_d}{\epsilon_m + 2\epsilon_d} \quad (2.74)$$

When trying to do the same dipolar analysis when the applied field is not static but time-dependent we obtain

$$\begin{aligned} C_{ext} &= k \operatorname{Im} \{ \alpha \} = \pi r^2 4x \operatorname{Im} \left\{ \frac{\epsilon_m - \epsilon_d}{\epsilon_m + 2\epsilon_d} \right\} \\ C_{sca} &= \frac{k^4}{6\pi} |\alpha|^2 = \pi r^2 \frac{8}{3} x^4 \left| \frac{\epsilon_m - \epsilon_d}{\epsilon_m + 2\epsilon_d} \right|^2 \end{aligned} \quad (2.75)$$

This description is accurate just if scattering is small compared with absorption.

2.2.5 Ellipsoid in the electrostatic approximation

The experiments in this project will be performed with samples composed of nanodisks. We need therefore something to describe these samples, going further than the description of absorption and scattering of a sphere. In the quasi static approximation it is possible to describe ellipsoid, in terms of Mie theory. The problem, in the quasi static approximation, is the one finding the dipole moment of an ellipsoid induced by an electrostatic field. To do so, we describe the ellipsoid with ellipsoidal coordinates (ξ, η, ζ)

$$\begin{aligned} \frac{x^2}{a^2 + \xi} + \frac{y^2}{b^2 + \xi} + \frac{z^2}{c^2 + \xi} &= 1, \quad -c^2 < \xi < \infty \\ \frac{x^2}{a^2 + \eta} + \frac{y^2}{b^2 + \eta} + \frac{z^2}{c^2 + \eta} &= 1, \quad -b^2 < \eta < -c^2 \\ \frac{x^2}{a^2 + \zeta} + \frac{y^2}{b^2 + \zeta} + \frac{z^2}{c^2 + \zeta} &= 1, \quad -a^2 < \zeta < -b^2 \end{aligned} \quad (2.76)$$

Looking for the potential inside and outside of a particle in an homogeneous electrostatic field aligned along the z axis, we in the end find a dipole moment which can be written as:

$$p = 4\pi\epsilon_d abc \frac{\epsilon_m - \epsilon_d}{3\epsilon_d + 3L(\epsilon_d - \epsilon_m)} E_0 \quad (2.77)$$

where in this case the form factor, $L = L_3$, considering the field aligned to the z axis

$$L_3 = \frac{abc}{2} \int_0^\infty \frac{dq}{(c^2 + q)f(q)} \quad (2.78)$$

From the expression of the dipole moment we recognize the polarizability, expressed as:

$$\alpha_3 = 4\pi abc \frac{\epsilon_d - \epsilon_m}{3\epsilon_d + 3L_3(\epsilon_d - \epsilon_m)} \quad (2.79)$$

When the field is aligned with one of the other axis, the polarizability has the same expression, what changes is the form factor.

To describe a disk, a special class of spheroid can be considered. Oblate spheroids, which have $b = a$ and $L_1 = L_2$, are generated by rotating an ellipse about its minor axis. For the oblate spheroid we have a particular expression for the form factor L_1

$$L_1 = \frac{g(e)}{2e^2} \left[\frac{\pi}{2} - \tan^{-1} g(e) \right] - \frac{g^2(e)}{2} \quad (2.80)$$

$$g(e) = \left(\frac{1 - e^2}{e^2} \right)^{\frac{1}{2}}, e^2 = 1 - \frac{c^2}{a^2}$$

The form factor is thus a function of the eccentricity. For a disk $e = 1$. The same expressions found in the previous subsection, for the different cross sections, can be used for an ellipsoid, replacing the proper polarizability expression [3]. Along this project the quasi static approximation could be used to describe the Gold samples, since the dimensions of the gold nanodisks are small enough. This is not true for the Silicon samples, which nanodisks dimension are larger. Simulations on the nanodisk structure anyway have been performed using a discret-time Fourier transform (DTFT) method, by Nils Odebo. From those simulations we have plotted the different efficiencies, as we did before.

The efficiencies of Gold and Silicon nanodisks can be seen in fig. 2.11.

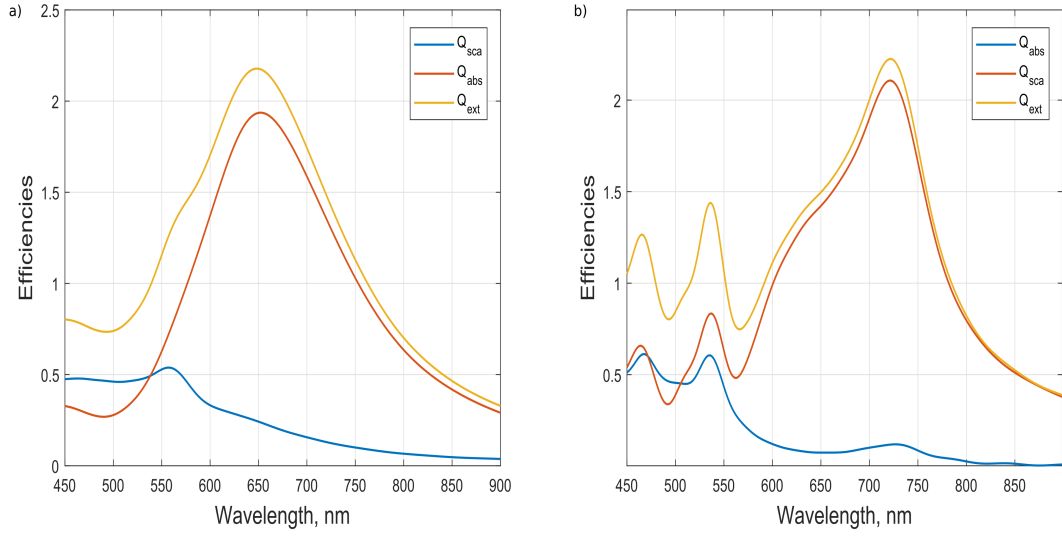


Figure 2.10: Extinction, Absorption and Scattering efficiency in water ($n \simeq 1.33$). a) Gold nanodisk with diameter 80 nm and thickness 125 nm b) Silicon nanodisk with diameter 175 nm and thickness 140 nm.

Also for nanodisks it appears that for Gold absorption is dominating, while in Silicon, the dominating efficiency is the scattering one.

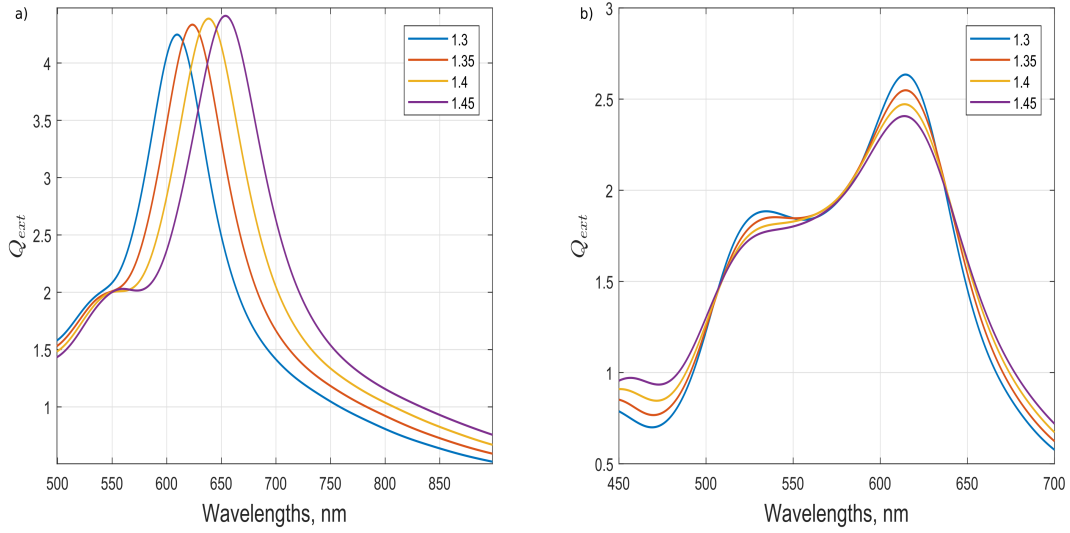


Figure 2.11: Extinction efficiency increasing refractive index from 1.3 to 1.45. a) Gold nanodisk with diameter 80 nm and thickness 125 nm b) Silicon nanodisk with diameter 175 nm and thickness 140 nm.

As for the nanosphere we notice the same behaviour for both the materials. A red shift of the resonance peak for gold with an increase of the intensity, while a decrease in intensity

with no resonance shift for the lowest energy peak of Silicon. These are the results that we expect to obtain from the experiments.

2.3 Dielectric function

Mie theory represents an efficient and quite easy tool to be used in this project. This mainly because it can be applied for study both metallic and dielectric nanoparticles. The differences between these two materials in fact, are taken into account in the differences in the dielectric function. The main difference between conductors and non conductors is find looking at the different energy bands. In conductors a band of electron states can be not totally filled, or an overlap in energy between a filled and an empty band can occur; this means that electrons can be excited into unoccupied states, by applying an electric field. This means that a conductor provides electron states in the same energy band, and this lead to intraband absorption. In non conductors we mainly have interband absorption that can occur just for impinging photons with energy greater than the energy gap. This lead to great differences in the optical properties: conductors are usually reflecting at visible and infrared wavelength and highly absorbig for low photon energies while non conductors tends to be transparent and weakly reflecting for photons with energies less than the band gap [2].

2.3.1 Gold dielectric function: Drude model

The Drude model is based on the assumption that the kinetik theory of gases can be applied to metals, considered as a gas of electrons, the "free" electrons. The assumption is that the positive charge present in the solid, can be considered immobile. Considering an applied time dependent electric field of the form:

$$E(t) = Re(E(\omega)e^{-i\omega t}) \quad (2.81)$$

the equation of motion for the momentum per electron can be written as:

$$\frac{dp}{dt} = -\frac{p}{\tau} - eE \quad (2.82)$$

What we look for is a steady solution of the form

$$p(t) = Re(p(\omega)e^{-i\omega t}) \quad (2.83)$$

Substituting we find that $p(\omega)$ must satisfy:

$$-i\omega p(\omega) = -\frac{p(\omega)}{\tau} - eE(\omega) \quad (2.84)$$

The current density become:

$$j(\omega) = -\frac{nep(\omega)}{m} = \frac{(ne^2/m)E(\omega)}{(1 - \tau) - i\omega} \quad (2.85)$$

and since $j(\omega) = \sigma(\omega)E(\omega)$ the frequency dependent conductivity results in:

$$\sigma(\omega) = \frac{\sigma_0}{1 - i\omega\tau}, \sigma_0 = \frac{ne^2\tau}{m} \quad (2.86)$$

At this point from Maxwell's equation, considering to have a certain current density j we can find that:

$$-\nabla^2 E = \frac{\omega^2}{c^2} \epsilon(\omega) E \quad (2.87)$$

with complex dielectric function

$$\epsilon(\omega) = 1 + \frac{4\pi i\omega}{\omega} \quad (2.88)$$

If we are in the condition in which $\omega\tau \gg 1$ then we can rewrite it as:

$$\epsilon(\omega) = 1 - \frac{\omega_p^2}{\omega^2} \quad (2.89)$$

where ω_p is the *plasma frequency*, given by:

$$\omega_p^2 = \frac{4\pi ne^2}{m} \quad (2.90)$$

The dielectric function can be seen in fig. 2.12 as a function of wavelength and energy.

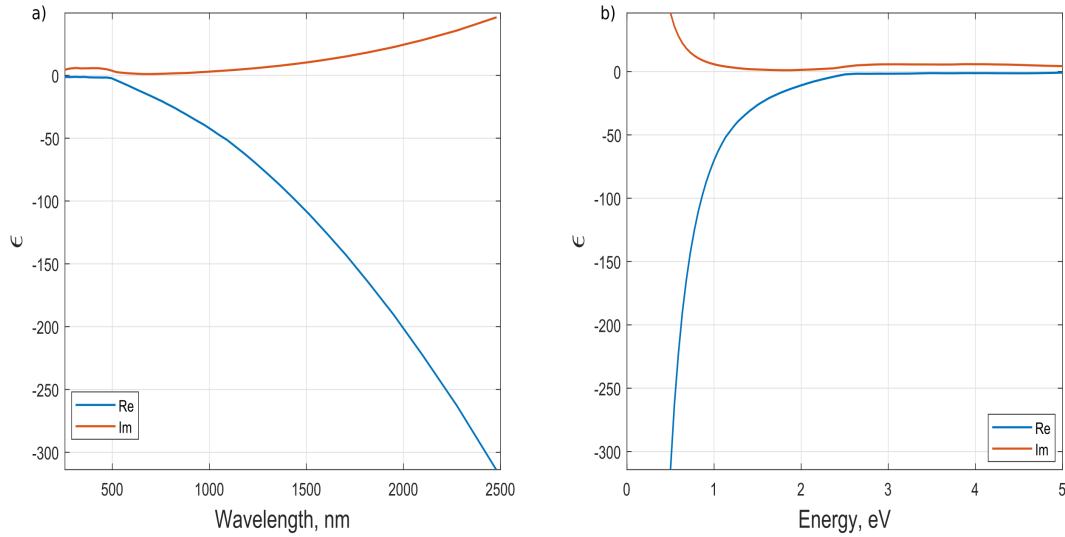


Figure 2.12: a) Dielectric function of gold as a function of wavelength b) Dielectric function of gold as a function of energy. Datas taken from [8].

2.3.2 Silicon dielectric function: Lorentz model

To describe the optical properties of materials, including dielectric, we can in principle start from the Lorentz model. This model is based on the classical theory of interaction between light and matter. In the Lorentz model, which describes the frequency dependent polarization which is due to bound charge, electrons and ions are treated as harmonic oscillators. These harmonic oscillators are subjected to the driving force of the applied electromagnetic field [29]. The equation of motion of these oscillators is:

$$m\ddot{x} + b\dot{x} + Kx = eE_{loc} \quad (2.91)$$

where E_{loc} is the local electric field acting on the electron. Kx represents the restoring force, where K is the spring constant and x is the displacement from equilibrium; $b\dot{x}$ is the damping force, where b represents the damping constant. The solution to this equation leads to two parts: a transient one, which dies due to the damping and an oscillatory one which oscillates with the same frequency of the driving field. The oscillatory part can be written as:

$$x = \frac{(e/m)E_{loc}}{\omega_0^2 - \omega^2 - i\gamma\omega} \quad (2.92)$$

where $\omega_0 = K/m$, $\gamma = b/m$. The induced dipole moment of a single oscillator is $p = xe$:

$$p = \frac{e^2 E_{loc}}{m} \frac{1}{(\omega_0^2 - \omega^2) - i\gamma\omega} \quad (2.93)$$

Which can be generalized if we have N oscillators per unit volume to $Np = Nex$ so that results:

$$P = \frac{\omega_p^2}{\omega_0^2 - \omega^2 - i\gamma\omega} \epsilon_0 E \quad (2.94)$$

The dielectric function of our system results in:

$$\epsilon = 1 + \chi = 1 + \frac{\omega_p^2}{\omega_0^2 - \omega^2 - i\gamma\omega} \quad (2.95)$$

which is complex. The real and imaginary part can be written as:

$$\begin{aligned} \epsilon' = 1 + \chi' &= 1 + \frac{\omega_p^2(\omega_0^2 - \omega^2)}{(\omega_0^2 - \omega^2)^2 + \gamma^2\omega^2} \\ \epsilon'' = \chi'' &= \frac{\omega_p^2\gamma\omega}{(\omega_0^2 - \omega^2)^2 + \gamma^2\omega^2} \end{aligned} \quad (2.96)$$

A plot of both these contribution can be seen in fig. 2.13

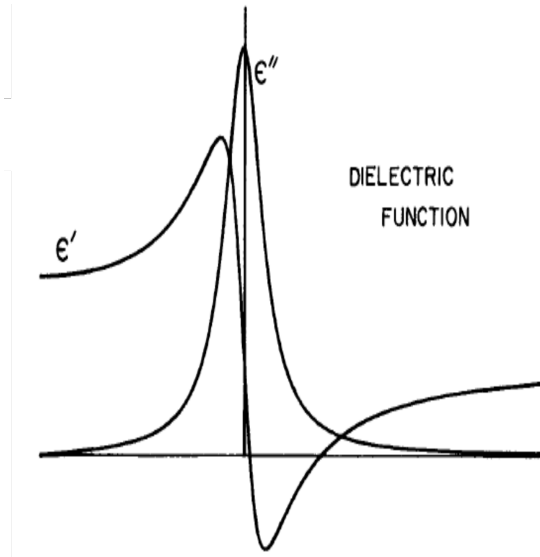


Figure 2.13: Real and Imaginary part of the dielectric function [3].

Lorentz model can be generalized to more than one kind of oscillator and anisotropic oscillators. An exact analytical model to describe the dielectric function of Silicon doesn't exist anyway, and the Lorentz model can be used just as a first approximation since its quantum mechanical analog takes into account just direct interband transition, but a corrected Lorentz model which including the differences in the oscillators and an approximate band structure gives results in fairly good agreement with experimental values. Different database providing measured Silicon dielectric function, as for gold, are present and can be used.

In the figure below the dielectric function of silicon in function of wavelength and energy can be seen.

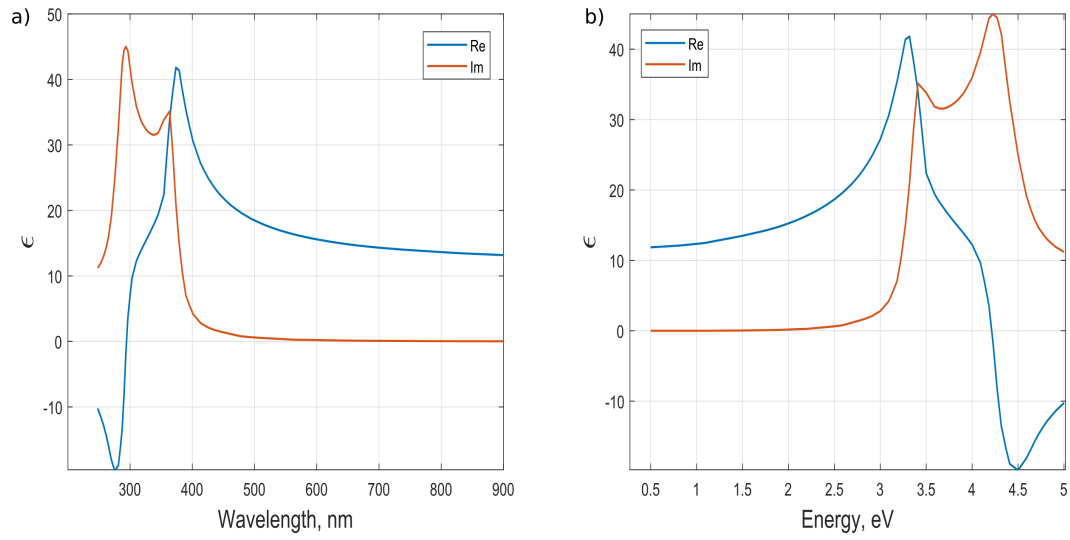


Figure 2.14: a) Dielectric function of silicon as a function of wavelength b) Dielectric function of silicon as a function of energy. Data taken from [8].

2.4 Mode analysis and near field

As seen in the previous subsections, the spectra for the gold and silicon nanostructures are greatly different. This is because when these structures are shone, different modes are excited. We have seen that these differences are principally due to the different dielectric function of the materials, which is taken into account in Mie theory. Following Mie theory, we have seen that the scattered field is written as an infinite series in the vector spherical harmonics, which represent the normal modes of the particles. In general the scattered field is a superposition of modes each weighted by the appropriate coefficient a_n or b_n . There are two different types of modes:

- Transverse magnetic mode: no radial magnetic field component
- Transverse electric mode: no radial electric field component

In this case what we see in gold is the first TM mode, the electric dipole mode, while in the silicon we always see both the electric and magnetic dipole and in some cases also the magnetic quadrupole mode is well visible.

A simple schematic of the field patterns for a sphere can be seen in fig. 2.15 To have a

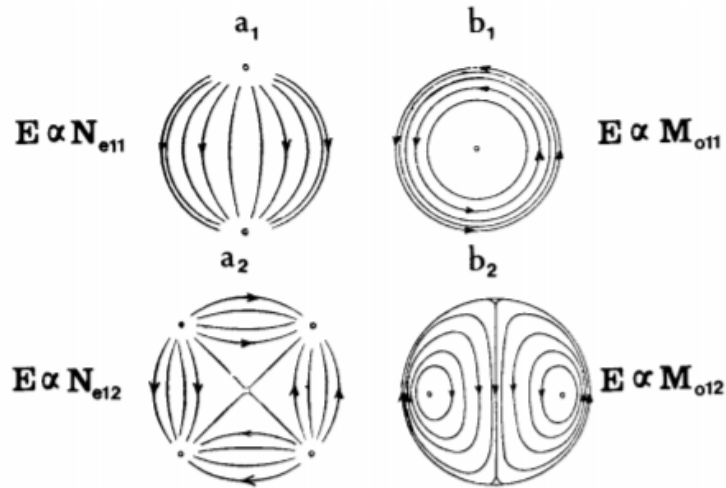


Figure 2.15: Field patterns for normal modes [3].

deeper vision of the modes in a disk shaped nanostructure some simulations have been performed to provide the near field of the structure. The extinction spectra will be shown as well.

Two example structures have been chosen: a gold nanodisk with diameter 150 nm and thickness 30 nm and a silicon nanodisk with diameter 170 nm and thickness 144 nm.

In figure 2.16 the spectra of the two structures can be seen.

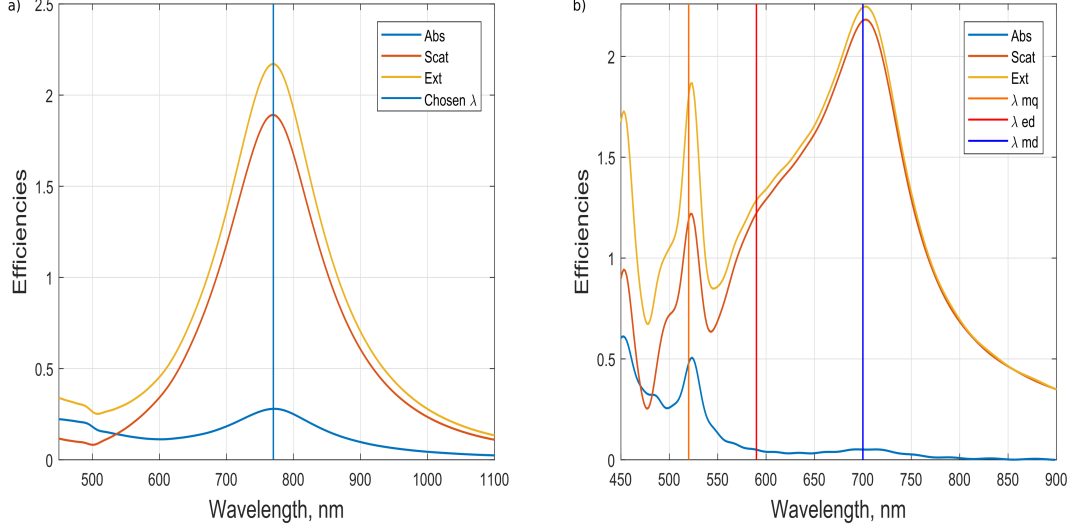


Figure 2.16: a) Gold efficiencies for nanodisks of 150 nm of diameter and 30 nm of thickness. b) Silicon efficiencies for nanodisks of 170 nm of diameter and 144 nm of thickness. For both the spectra we have in yellow the extinction, in blue the absorption and in orange the scattering efficiency. The lines represent the different wavelengths associated to the mode for which the electric field has been calculated.

For the gold nanostructures the only mode that is excited in the visible is the electric dipolar one; the reason is the different type of dielectric function between the two structures. The lowest energy resonance in gold occurs because the denominator in the electric dipole polarizability becomes near zero, where it follows from Mie theory that the electric dipole polarizability is proportional to a_1 . This is only possible because the real part of the dielectric function of gold is negative, which it isn't in silicon. The field has been calculated for $\lambda = 770 \text{ nm}$, which corresponds to the peak in the spectrum in fig. 2.16. The near field can be seen in fig. 2.17.

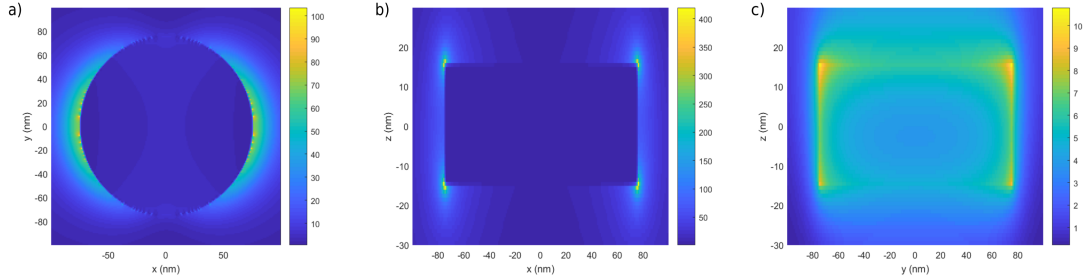


Figure 2.17: $|E|^2$ for Gold nanodisk corresponding to the electric dipole mode, calculated for $\lambda = 770 \text{ nm}$ a) Field along the XY plane b) Field along the XZ plane c) field along the YZ plane.

From the top view we can clearly see the dipolar behaviour of the field and its concentration on the surface of the particle. Along the XZ and YZ plane, a concentration of the field is visible on the corners of the structure. This is due to the so called *lightning rod effect*, which is a kind of field enhancement due to enhanced charge density localization at a tip or vertex of a nanoparticle. In the present case this has not real physical meaning since the real structure doesn't present such sharp corners.

As said before for Silicon things are different: for such a high refractive index dielectric structure, the extinction cross section, which is approximately equal to the scattering one due to the very low absorption cross section, features different peaks corresponding to both the magnetic and electric dipolar modes and a quadrupolar one. It's interesting to note, not only the different number of excited modes, but also that if for gold the lowest energy mode is an electric type, for silicon the lowest order peak correspond to the magnetic dipole mode (coefficient b_1) followed by the next higher order mode with coefficient a_1 , an electric type.

The same simulations have been done for silicon in correspondance of the three peaks that appears in the spectrum in fig. 2.16. The three wavelngts for the magnetic dipole, electric dipole and magnetic quadrupole are respectively $\lambda = 700 \text{ nm}$, $\lambda = 590 \text{ nm}$, $\lambda = 520 \text{ nm}$. The field corresponding to the magnetic dipole, electric dipole and magnetic quadrupole are shown in fig. 2.18, 2.19 and 2.20

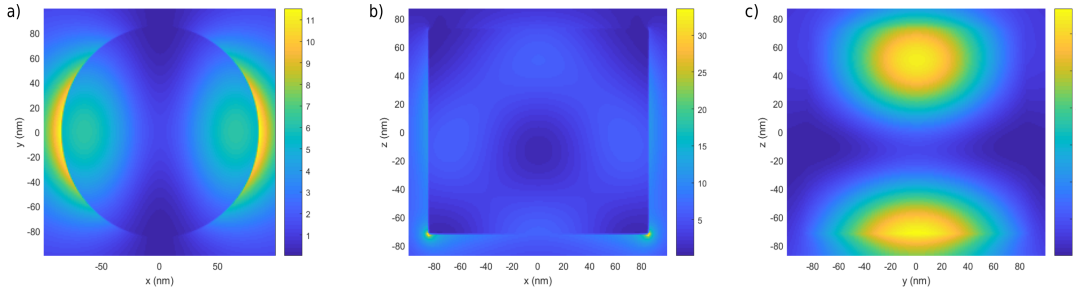


Figure 2.18: $|E|^2$ for Silicon nanodisk corresponding to the magnetic dipole mode, calculated for $\lambda = 700 \text{ nm}$ a) Field along the XY plane b) Field along the XZ plane c) field along the YZ plane.

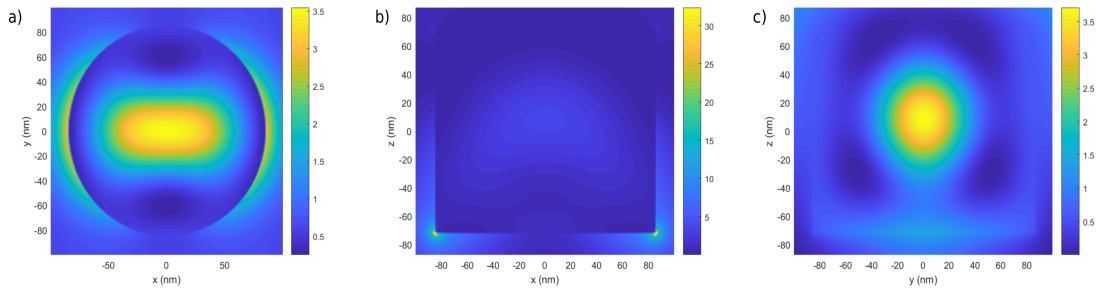


Figure 2.19: $|E|^2$ for Silicon nanodisk corresponding to the electric dipole mode, calculated for $\lambda = 590 \text{ nm}$ a) Field along the XY plane b) Field along the XZ plane c) field along the YZ plane.

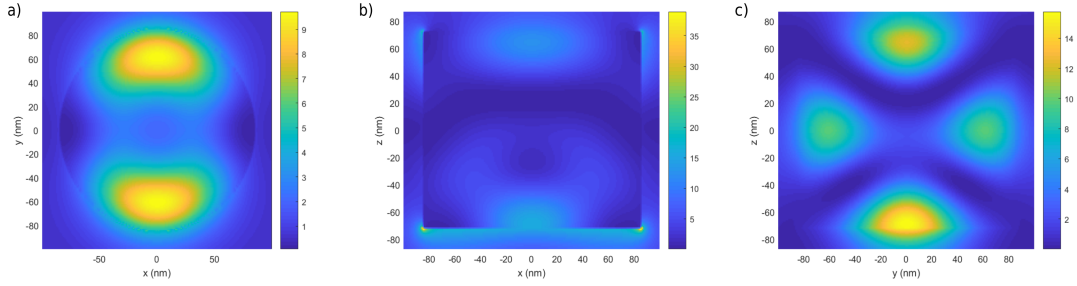


Figure 2.20: $|E|^2$ for Silicon nanodisk corresponding to the magnetic quadrupole mode, calculated for $\lambda = 520 \text{ nm}$ a) Field along the XY plane b) Field along the XZ plane c) field along the YZ plane.

From these plots a fundamental difference between the two structures can be derived. For the metal particles the field is concentrated at the surface, while in the dielectric case the field tends to remain in the interior of the particle. This already gives an hint in understanding why up to now metal nanoparticles, so plasmonic nanostructures, have been preferred for sensing purposes: the concentration of the field at the surface in fact, makes these kind of structure more sensitive to the surrounding environment.

It can also be noted that the field enhancement in the silicon structure is present but far lower with respect to the gold one.

Despite this, the strong electric and magnetic multipolar response of silicon nanostructures makes them interesting candidates as building blocks of magnetic materials.

2.5 Refractometric sensing

The optical properties of a material are defined as its interaction with electro-magnetic radiation. These properties depend on the nature of the material itself but also on the surrounding environment.

When an electromagnetic wave hits an object, the electric field generates a disturbance in the charge of the atoms in the material. This disturbance is proportional to the electric susceptibility of the material, and the same applies for the magnetic field. The charges in the material will start to follow the oscillation of the incident wave with the same frequency. The electromagnetic field generated by the oscillating charges in the medium will have the same frequency of the incident field, but a certain delay.

The resulting wave in the medium, will be the sum of the incident one and of the one generated by all the charges, and will have then the same frequency but a shorter wavelength. This results in a slowing of the wave's phase velocity.

The way in which light travels in a medium can be explained by the *refractive index*. This dimensionless number is defined as the ratio between the speed of light, and the phase velocity of light in the medium:

$$n = \frac{c}{v} \quad (2.97)$$

. The refractive index tell us how much the incident light is bent, when entering in a material.

This behaviour, *refraction*, is explained by the well known *Snell's law*, which tell us that the ratio between the sinus of the incidence and refraction angles is equal to the ratio between the refractive indices of the two materials taken into account:

$$\frac{\sin \theta_i}{\sin \theta_r} = \frac{n_r}{n_i} \quad (2.98)$$

The refractive index gives an idea on how much the speed and the wavelength of the incident wave are reduced with respect to their vacuum values, when entering in a material.

This explains why the environment and not only the material itself, plays a role in the interaction between light and objects. A wave hitting a medium after being in contact with another material, in fact, will produce a different reaction respect to the case of the same wave hitting directly the material, since the interaction with a medium different from vacuum, which means with a refractive index different from 1, will change the nature of the incident light.

This fundamental property of the light-matter interaction can be used to study the behaviour of a material in contact with a different environment, and the technique which exploit this property is the refractometric sensing.

Refractometric sensing is a surface sensitive technique which can detect changes in the refractive index through an optical readout.

This technique allows to overcome some of the problems that have been encountered with other sensing technique.

First of all this is a label free technique. This means that the solution to be sensed does not have to undergo to manipulations. Second it enables real time informations, since we monitor a physical property of the system.

In this project two different type or refractometric sensing have been used.

First of all the bulk refractometric sensing. In this case the refractive index of the hole surrounding medium was changed. In a second moment we focused on what we called local refractometric sensing. In this case we changed the refractive index just near the particles' surface.

In this chapter we describe the different experimental methods that have been used throughout this project.

The samples were fabricated with the so called hole-mask colloidal lithography (HCL) process. This method involves different steps that are described in the next subsections.

Finally we explain the HCL process and we pinpoint the differences between the fabrication of gold and silicon nanoparticles.

Afterwards, it is presented the experimental methods we developed in this process.

3.1 Fabrication

The entire fabrication process took place in the cleanroom.

The HCL process involves different steps:

- Spin coating
- Evaporation
- Oxygen plasma etching
- Inductively Coupled Plasma etching (ICP)
- Wet chemical etching
- Cryo etching
- SEM

3.1.1 Spin coating

The spin coating is one of the most common and easy technique which allows to deposit thin polymer film on a flat substrate.

The thickness of the deposited layer range from few nanometers to a few microns.

An amount of the desired solution is applied manually by a pipette onto the substrate which is then rotated at high speed in order to spread the fluid by centrifugal force.

The velocity, the acceleration, the rotational time and the viscosity of the polymer determine the final thickness of the layer, and can be tuned for specific applications.

The machine used for the spin coating technique is called spin coater or simply spinner.

For the HCL process we used polymethyl methacrylate (PMMA) resist 950k dissolved in anisole (4%). The spinning curve is shown in figure 3.1.

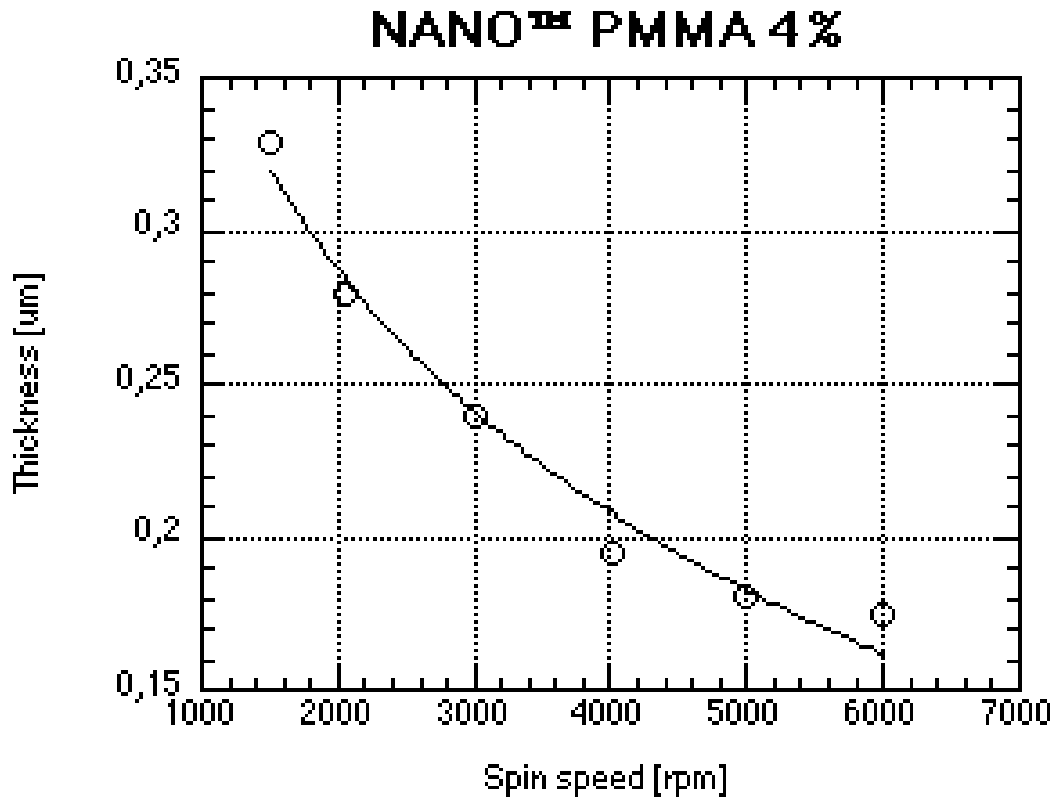


Figure 3.1: Thickness of the spin coated PMMA A4 film versus spin velocity [4].

3.1.2 Evaporation

Evaporation is a common technique typically used to deposit thin inorganic film onto a substrate. This process rely on the condensation of a gas/vapor phase on a surface, and is usually carried out in vacuum conditions.

In this project a physical vapor deposition (PVD) technique was used using a *LESKER PVD 225* evaporator.

In this kind of evaporator the source material is heated through an electron beam. The electrons are emitted by a tungsten filament via thermoionic emission and accelerated up to several kV.

The electron beam is then bent towards the source material by a magnet untill its evaporation.

The vapor particles in high vacuum travel directly onto the deposition target where they are adsorbed.

The most important parameters that can be controlled during the process are the base pressure the deposition rate and the deposition thickness.

The base pressure represents the minimum pressure that can be obtained in the chamber before starting the process and it directly influences the contamination level of the deposited film.

The thickness and the deposition rate are monitored in-situ by a quartz crystal microbalance inside the chamber.

3.1.3 Oxygen plasma etching

Oxygen plasma etching is a technique used to etch a surface by means of plasmas. Cold plasmas etchers are among the most commonly used tools to modify surfaces at the nanoscale.

A plasma is a gas in which a large enough fraction of the atoms or molecules has been ionized. It is a system containing several species, including:

- Neutral atoms and/or molecules
- Neutral radicals
- Ionized atoms and/or molecules (positive/negative ions)
- Ionized radicals
- Electrons
- Electromagnetic radiation (photons)

In a plasma process, only a fraction of the electrons will have enough energy to activate specific processes inside the gas mixture. The main processes activated by plasma electrons are:

- Ionization of atoms/molecules/radicals required to keep the plasma activated
- dissociation of gas molecules

- excitation of atoms/molecules/radicals
- attachment of an e^- to a atom/molecule with formation of a negative ion

Oxygen plasma is the most common plasma used in plasma cleaning or etching. The plasma is created by a RF excitation, that ionizes the gas. The electrons in the plasma are lighter and faster than the ions, so they are more easily adsorbed onto the wafer platter with respect to the ions, resulting in a net negative charge close to the target's surface. Due to this charge build up, the positive ions will be now attracted to the surface with a certain acceleration resulting in a chemical or physical etching (sputtering) of the target. All the etching performed with this technique were performed with a 50W power at a pressure of 250mTorr with a O_2 flow of 10sccm (standard cubic centimeter per minute). The overall reaction occurring when using the oxygen plasma to etch the PMMA resist is:



The machine used in this project is from *Plasmatherm* model *BatchTop m/95*.

3.1.4 ICP etching

ICP etching was used in this project to transfer the Nickel nanodisks pattern to the Silicon film, during the fabrication of the Silicon samples.

This is a reactive ion etching technique based on the use of an inductively coupled plasma source. The source creates a high-density plasma due to inductive coupling between a RF antenna and the plasma. This kind of discharge exploit a solenoid in which a RF current is flowing, producing:

- a time-varying magnetic field
- an induced non-conservative electric field

Both energize the electrons that participate in the ionization of gas molecules and atoms at low pressure.

The electric field is almost not present near the reactor walls, so that the walls don't undergo nor to ion bombardment nor to erosion.

For the inductive coils, different geometries exist; they can be:

- cylindrical: the generated magnetic field is uniform
- planar: the generated magnetic field is not uniform

This system typically runs at low pressure and uses two independent RF sources: one RF generator applies power to the ICP coil, which controls the ion flux, while a bias power is applied to the lower electrode to extract and accelerate ions and radicals from the plasma towards the substrate.

Etch conditions can be adjusted and optimized by tuning the settings of many process parameters such as RF power, pressure, and gas flows. In this project a *Plasmalab 100 ICP180* from *Oxford Plasma Technology* was used.

To etch the Silicon substrate chlorine is used. Chlorine atoms are chemisorbed one at a time on the silicon surface, eventually forming volatile $SiCl_4$.

The overall reaction is:



3.1.5 Wet chemical etching

Wet etching is usually performed in an acid bath in which the substrate is immersed; chemical reactions occur at the liquid-solid interface. The time required depends on the composition and on the thickness of the layer to be etched and also on the used chemical and on the temperature.

Wet etching is selective to specific target materials.

This technique is usually more common with respect to dry etching since it's both quicker and cheaper even though it can presents some difficulties; some materials in fact, for example silicon, exhibit anisotropic etching in certain chemicals, which means that certain crystalline planes are more etched than others. When the etching is isotropic, it usually causes undercutting of the mask layer.

One very important parameter in wet etching is then selectivity, which is defined as the ratio between the etch rate of the desired material and of the undesired one.

In this project wet etching has been used as last step in the Silicon HCL process to remove the Nickel metal mask.

The used chemical is based on ceric ammonium nitrate, which has an etch rate of $40 \frac{\text{\AA}}{\text{sec}}$ at room temperature.

3.1.6 Cryo etching

Cryogenic etching is a particular deep reactive ion etching (DRIE) technique and was used in this project to fabricate the silicon master used in the fabrication of the microfluidic channels.

DRIE is a very-high aspect-ratio silicon etching method that usually relies on a high-density plasma source and an alternating process of etching and protective polymer deposition to achieve anisotropy on the order of 30:1; it is commonly used to create deep penetration, steep-sided holes and trenches in wafers/substrates.

This process is usually referred as *Bosch process*.

An alternative technique to the Bosch process involves etching substrates at cryogenic temperatures. The main reactions that occur in reactive ion etching (RIE) are the chemical reactions at the surface to be etched, and the ion sputtering. To create an highly anisotropic etching, as in the *Bosch process*, the chemical reactions need to be considerably slowed down; this can be accomplished by controlling the substrate temperature, since a lower temperature will reduce the reaction probability.

The machine used in this project is *PlasmaPro 100 Cobra ICP 180* from *Oxford Instruments*. To etch the Silicon substrate of the sample, a mixture of SF_6 , Ar and O_2 at 10K was used.

An image of the Silicon master can be seen in fig 3.2.



Figure 3.2: Silicon master for microfluidics

3.1.7 SEM

The scanning electron microscope is a type of electron microscope where an image is created by focusing an electron beam onto a sample.

The usual range for incident electron beam is between 0.5-40keV.

The main component of a scanning electron microscope are:

- Electron gun
- Electron lenses
- Sample stage
- Detectors
- Display

A simple schematic of a SEM can be seen in fig 3.3. The source electrons can be extracted by *thermoionic emission* or *field emission*.

In the thermoionic gun, the atoms in the metal, usually tungsten, are heated in order to raise the energy of orbital electrons through the work function value so that the electron can escape from the surface of the metal.

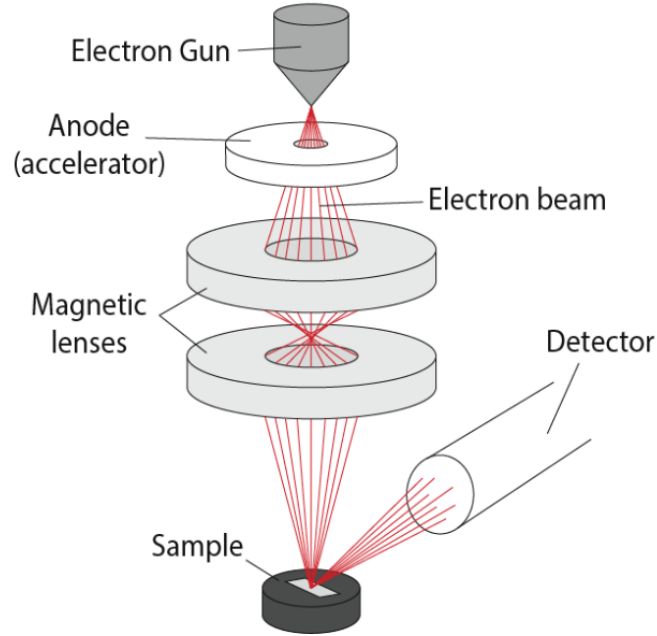


Figure 3.3: Scanning electron microscope schematic [23]

The thermoionic current density follows the *Richard's equation*

$$j_{thermoionic} = AT^2 e^{-\frac{\phi}{kT}} \quad (3.3)$$

In the field emission gun a strong electric field is applied at the tip of a tungsten wire, fashioned into a sharp point and spot welded to a tungsten hairpin, in order to decrease the potential barrier allowing the electrons to tunnel through the barrier and leave the cathode.

The field emission gun presents a series of advantages with respect to the thermoionic one: this kind of gun in fact, provides a larger brightness and monochromaticity, which results in a higher signal and in a higher resolution respectively.

The tungsten wire is usually sharpened by electrolytic etching in order to obtain a tip with a diameter ranging between 100-1000 Å.

The source beam passes then in between two lenses:

- Condenser lens: used to demagnify and condense the beam.
- Objective lens: used to focus the beam onto the specimen.

The focal length of the objective lens can be changed varying the current in it, since this will change the magnetic field strength.

Two set of coils are used to scan the electron beam accros the specimen surface in a raster pattern.

From the interaction between the sample's surface and the source beam, different signal are produced:

- Secondary electron (SE)
- Back-scattered electrons (BSE)
- X-rays
- Visible light (cathodoluminescence)

Each of these signals give different information about the sample.

The generation region of backscattered electrons is larger than that of secondary electrons (which is several tens of nm). Therefore, backscattered electrons give poorer spatial resolution than secondary electrons making them more valuable for illustrating contrasts in composition in multiphase samples.

Secondary electrons, instead, are most valuable for showing morphology and topography.

Using the signal of secondary electrons, image resolution less than 0.5 nm is possible.

For this project a *Supra VP 55* from *Zeiss* SEM was employed. This particular SEM apparatus is equipped with a field emission gun working between 1-30keV and uses *Gemini* column which optics is characterized by three main component:

- Objective lens: it combines both electrostatic and magnetic fields to maximize the performances while minimizing the fiels influences at the sample.
- Beam booster technology: integrated beam deceleration to provide small probe sizes and high signal to noise ratios.
- Inlens detection: to detect both secondary and back-scattered electrons.

When imaging with a SEM low acceleration voltages are sometimes preferred to minimize and compensate charges and irradiations on the sample surface.

If electrons hit a non conducting or only partially conducting specimens, these electrons accumulate on the surface as they cannot discharge due to the reduced conducting capacity.

Local charges are generated which affect the electron beam and may significantly deteriorate the imaging quality.

In order to avoid this situation, for the sample's imaging performed in this project a conductive resist, the *ESPACER 300AX01* has been spin-coated onto the sample for 40 seconds

at 3000rpm prior to imaging and removed afterwards in deionised (DI) water. Due to the different species that can be obtained from the electron beam/sample interaction, different kind of detectors are present in the SEM.

For the images collected in this project an *In-lense* detector has been used.

The detection efficiency of this kind of detector results from its geometric position in the beam path and from the combination with the electrostatic/electromagnetic lens. The detector is placed above the objective lens and detects directly in the beam path.

3.1.8 HCL process

The HCL process represents a powerful and simple tool in bottom-up nanofabrication that provides an effective means of patterning large surface areas with diverse functional nanoarchitectures [10].

In this section a general explanation of the process is presented, while details about the differences of the HCL process for Gold and Silicon are presented in the next sections.

A schematic of the process is shown in fig 3.4.

First the substrate is cleaned with acetone and isopropyl alcohol by sonication. Then a sacrificial layer of PMMA (polymethyl methacrylate) A4 is spin coated on the substrate at 3000rpm for 40 seconds and then soft baked in the oven for 10 minutes at 180 °C.

The resulting PMMA layer has a thickness of approximately 240 nm.

At this point the substrate is etched in oxygen for 5 seconds in order to decrease the hydrophobicity of the PMMA layer. Poly(diallyldimethylammonium) chloride (PDDA), 0.2% is applied on the surface by a pipette for 30 seconds, washed with DI water for approximately 30 seconds and then dried with nitrogen gun.

Afterwards polystyrene beads (PB) are applied with a pipette and incubated for 2 minutes and 15 seconds, the sample is then washed and dried again.

At this point a 10nm layer of gold is evaporated onto the surface to create a mask. The polystyrene beads are then separated from the surface by tape stripping.

To be able to get a reference signal during the measurements, it has been decided to perform the tape stripping only on one half of the sample; in this way the final sample will presents the desired nanostructures only on the side where the tape stripping was done. The removal of the PS beads, will form holes in the gold mask, leaving exposed the previous spin coated PMMA layer that is then oxygen etched for 4 minutes.

A glass is used to cover the tape un-stripped part during this process to make easier the removal by lift off of the unwanted part.

At this point, a second evaporation is done. The metal is evaporated through the holes defined by the previous deposited gold mask. The deposition's thickness will determine the disks' height. As a final step a lift-off of the PMMA in acetone is done.

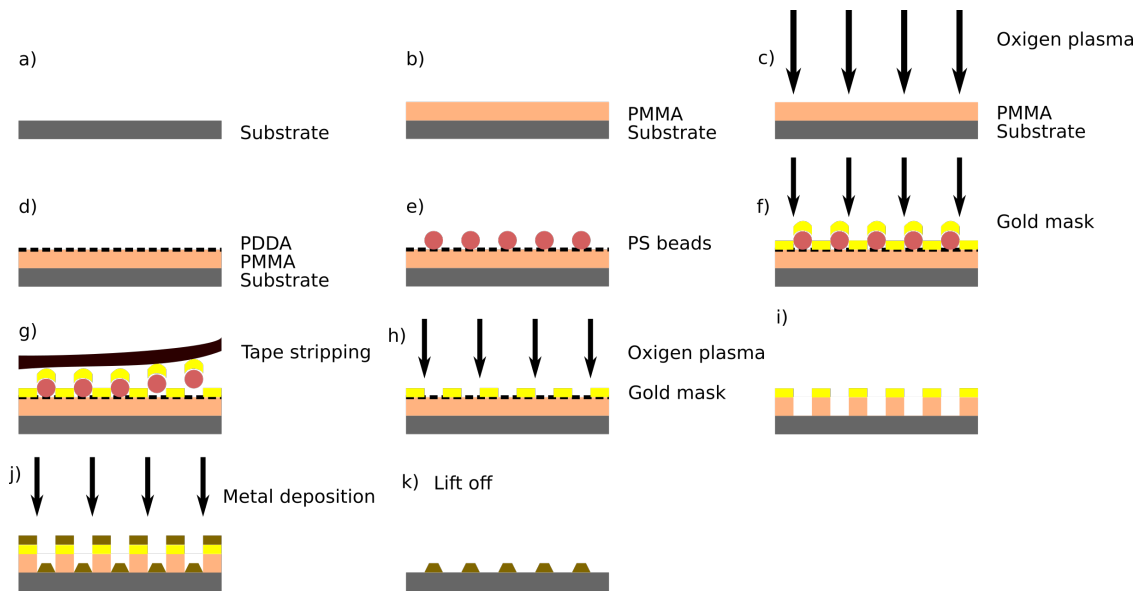


Figure 3.4: a) Cleaned substrate b) PMMA spin coating c) O_2 plasma etch d) PDDA coating e) PS deposition f) 10 nm Gold deposition g) tape stripping h) O_2 plasma etch i) O_2 PMMA etch j) Metal deposition k) Lift off

Gold

For the gold samples, a glass squared substrate with 2,5 cm side and thickness 0.1 mm was used.

In order to obtain disks with different diameter, PS beads with diameter of 100, 150, 170 and 200 nm were used while the disks' height was kept constant for each sample.

In the fabrication of gold disk, the second evaporation is performed with gold; 30 nm were deposited.

Before the gold layer, however, a prior deposition of 1 nm of Ti is done to improve the metal adhesion to the glass substrate.

After the lift off, the gold samples need a further annealing step performed at 250 °C for 10 minutes. An example of the imaging on one of the gold samples is shown in fig. 3.5

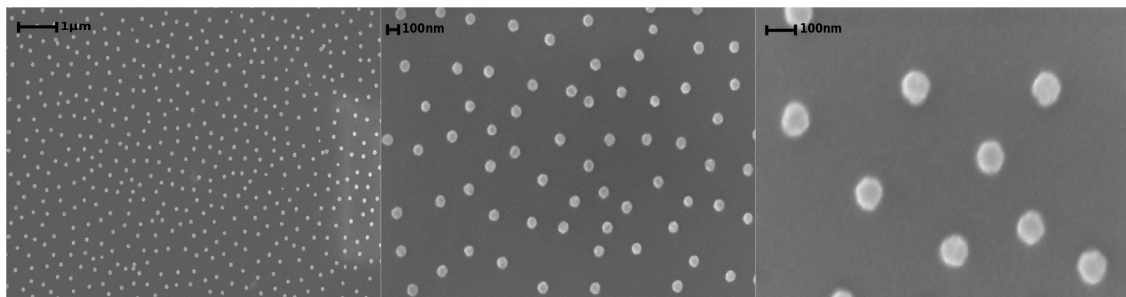


Figure 3.5: Gold nanodisks with diameter 100nm and height 30nm at different magnifications.

Silicon

For the silicon samples, a 4 inches fused silica (SiO_2) substrate was used.

First of all a layer of amorphous silicon is deposited on the substrate by LPCVD (low pressure chemical vapour deposition) technique, at 550 °C and a pressure of 250 mtorr.

The CVD process relies in the formation of a thin film from vapor phase reactants.

Between the different CVD techniques LPCVD, performed with a pressure range between 5 and 250 Pa, presents the advantage of a deposited film with excellent uniformity and purity and with low stress. The deposition was performed with silane gas (SiH_4).

Three different thicknesses of 113, 144 and 200 nm were obtained changing the deposition time.

After the deposition, in order to obtain polysilicon, the substrate is annealed with nitrogen at 1000 ° for 30 minutes.

Subsequently, the silicon on the back side of the wafer is removed by $CF_4 : O_2$ (10:1) gas mixture at a pressure of 250mT for 3 minutes.

This step is needed since during the LPCVD, amorphous silicon is deposited also on the backside of the substrate.

To protect from the etching the side that will be processed, a resist is applied on it. The resist used is *S1813*, and is spin coated for 45 seconds with a velocity of 2500 rpm, followed by a soft bake of 1 minutes at 95 °C.

At this point the wafer is cut in squares of 1 cm side, giving rise to the substrates onto which the HCL process is performed singularly.

As for the gold samples, silicon disks with 100, 150, 170 and 200 nm diameter were fabricated on each substrate.

The second metal evaporation is performed with nichel rather that gold.

In this case nichel is used as a patterning mask for the underlying silicon substrate. Nichel is a hard metal, slowly etched by chlorine, which makes it a suitable choice for this process. Once the lift-off is done, the Silicon is patterned with ICP with chlorine at 5mTorr, 25W forward power, 0 ICP (see section 3.1.4).

The remaining Nichel is removed by wet etching as mentioned in subsection 3.1.5. The samples are immerged for 6-7 minutes, then carefully washed and dried with nitrogen gun. A schematic of the process can be seen in fig 3.7.

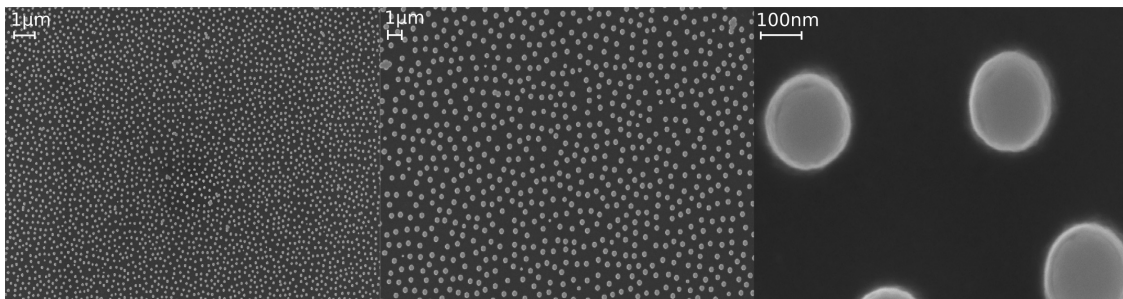


Figure 3.6: Silicon nanodisks with diameter 200nm and height 144nm at different magnifications.

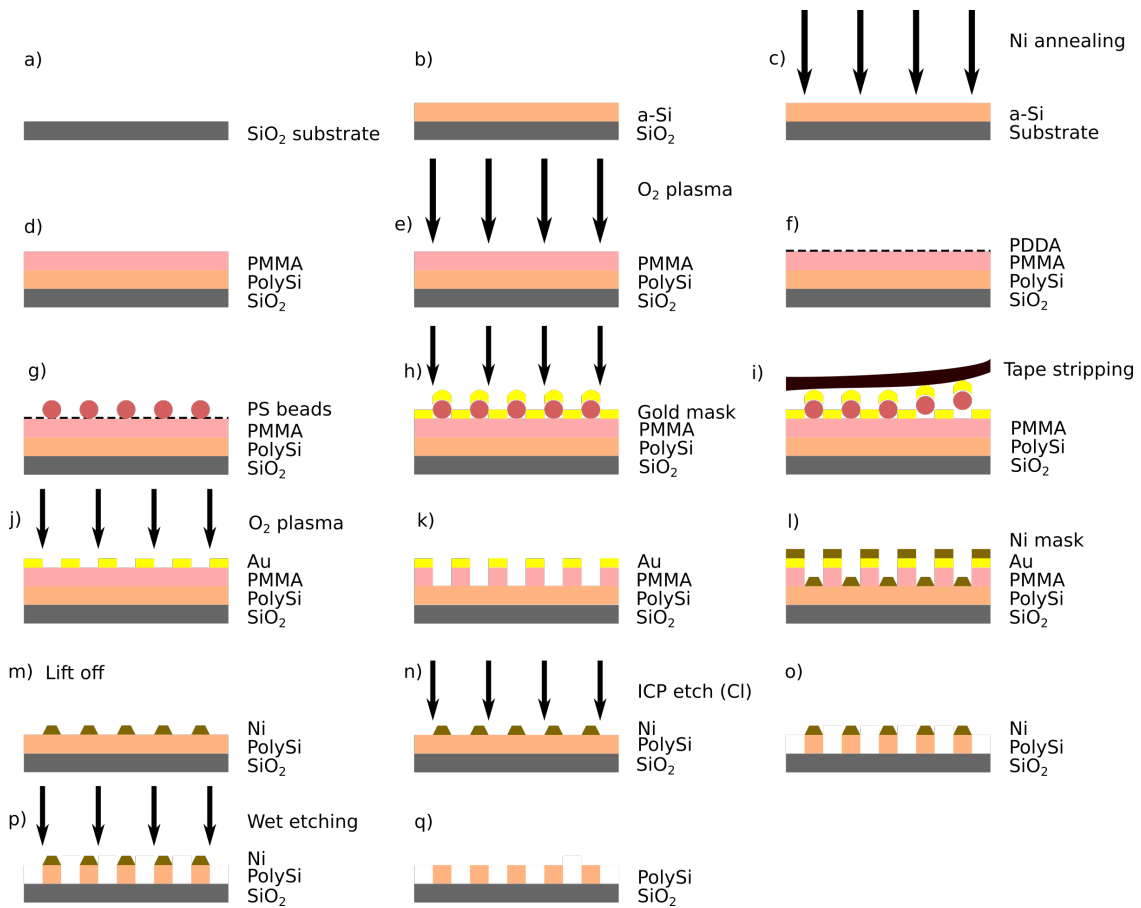


Figure 3.7: a) Cleaned substrate b) amorphous Si deposition c) Nitrogen annealing d) PMMA spin coating e) O_2 plasma etch f) PDDA coating g) PS deposition h) 10 nm Gold deposition i) tape stripping j) O_2 plasma etch k) O_2 PMMA etch l) Ni deposition m) Lift off n) ICP etching of the poly-Si with Cl o) structure after the etching p) wet etching of the remaining Ni

3.2 Measurements procedure and setup

The samples characteristics have been studied by means of transmission spectroscopy. This kind of measurements consist in two steps:

- Reference collection: measure of the reference light without the sample (I_0).
- Signal collection: measure of the light with the sample (I).

For each wavelength λ the transmission can then be defined as:

$$T = \frac{I}{I_0} \quad (3.4)$$

In this project the light source employed is an halogen lamp from *Ocean Optics*. Halogen lamps are an advanced form of incandescent lamp, where the filament is composed of ductile tungsten and located in a gas filled bulb. The gases are usually a mixture of an inert gas and iodine or bromine.

This kind of lamps produce a continuous spectrum of light, from near UV to infrared.

For translucent objects, like the samples in this project, a part of the source light will be reflected, part will be absorbed, part will be scattered and the remaining part will be transmitted.

The deviation between these variables is defined by the sample.

Due to conservation of energy, the total amount of light emitted by a light source directed onto a sample, is equal to the sum of absorption (A), reflection (R), transmission (T) and scattering (S) of that particular sample, i.e. $1 = A + R + T + S$.

In the sample made of densed packed nanodisks the scattering is assumed to be null.

A sketch of the optical setup can be seen in fig. 3.9, followed by a photo in fig. 3.8

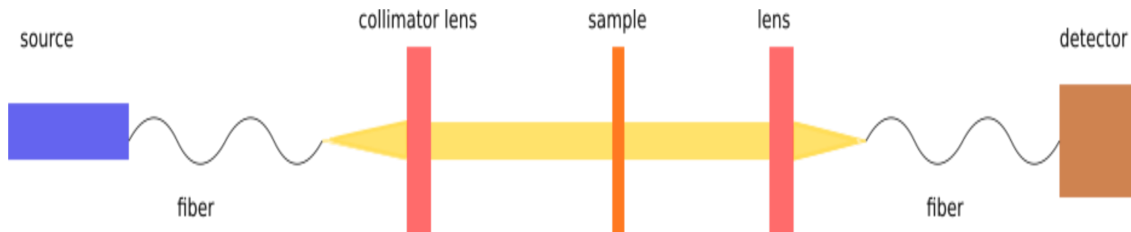


Figure 3.8: Optical setup sketch.

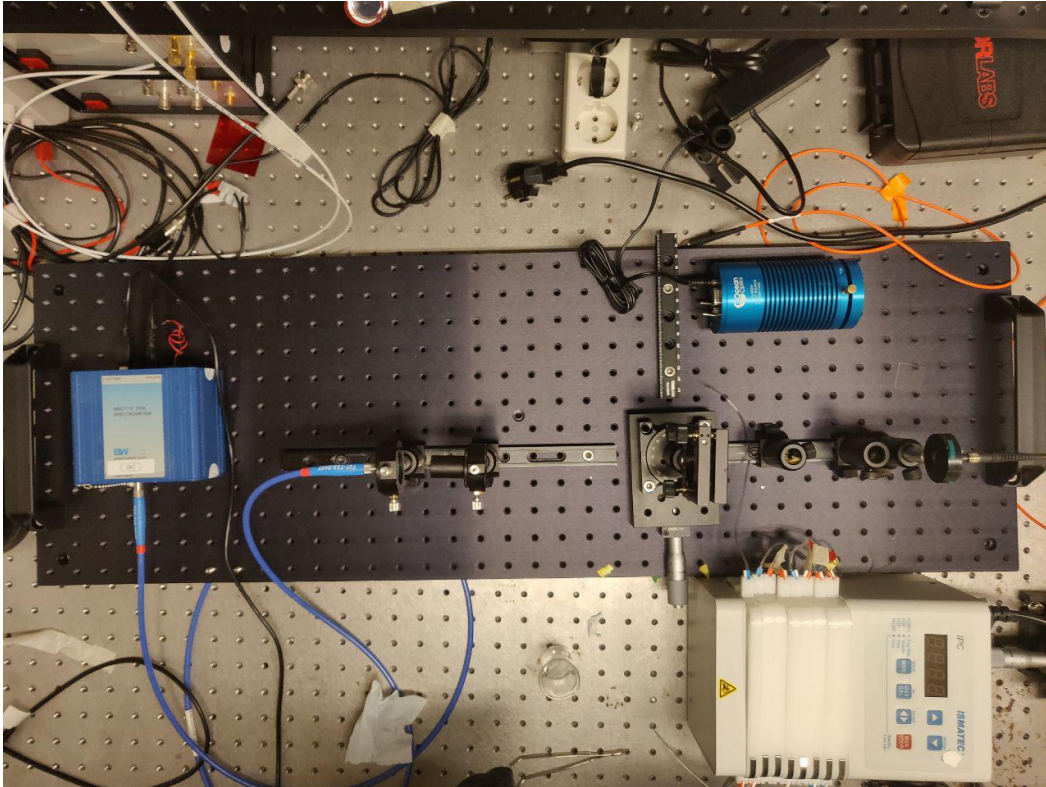


Figure 3.9: Optical setup used for the measurements

The light is sent to the optical table by a $50\mu\text{m}$ diameter optical fiber with numerical aperture (NA) equal to 0.22. The light passes through a first dispersive lens to collimate the beam.

After the interaction with the sample, the beam passes through a second lens, which focuses the beam on the fiber coupled with the spectrometer/detector system. A spectrometer is a system composed by two mirrors, a grating and a detector. Once the light enters the spectrometers, it hits a first mirror which collimates the light onto the grating. The beam will be diffracted by the grating, differently according to the wavelength. The diffracted beams are reflected towards the second mirror, which focuses them onto the detector. Each chip on the detector, detects a different wavelength.

A schematic of the spectrometer can be seen in fig 3.10

In this project a spectrometer from *B&WTEK* BRC711E PDA was employed. The detector in this spectrometer is a *NIR enhanced 512-element linear photodiode array (PDA)*. A PDA array is a linear array of discrete photodiodes on an integrated circuit. Photodiodes are based on p-n or p-i-n junctions. When the light hits the PDA, it generates an electron-hole pair. Charges feel the built-in electric field of the junction's depletion region.

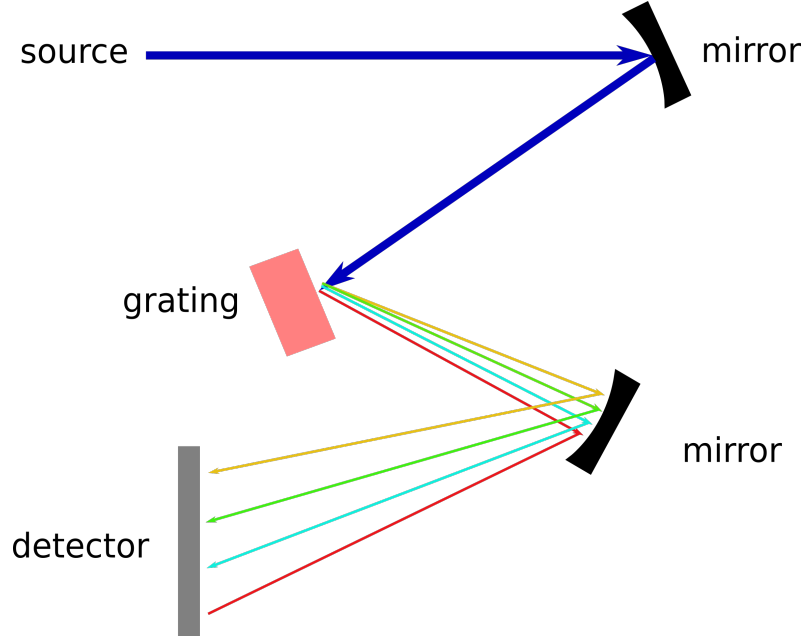


Figure 3.10: Spectrometer schematic

Electrons and holes will move towards the cathode and the anode respectively, generating a photocurrent. The I-V characteristic for a photodiode follows the modified *Shockley equation*:

$$i = i_s \left[\exp\left(\frac{eV}{k_B T}\right) - 1 \right] - i_p \quad (3.5)$$

where i_s is the *inverse saturation current*, while i_p is the *photocurrent*. In a PDA the electrical signal generated by the photodiodes is temporarily stored and then read as time-series signals via the output line by sequentially turning on the switch array connected to each photodiode.

The property in which we are interested is the extinction, calculated as:

$$ext = 1 - T \quad (3.6)$$

where T is the transmission.

3.2.1 Microfluidic

In order to perform the sensing measurements a microfluidic setup was added to the optical one.

For the fabrication of the microfluidic chips, one of the most used material is Polydimethylsiloxane (PDMS).

PDMS is a mineral-organic polymer (a structure containing carbon and silicon) of the siloxane family. For the fabrication of the device a plastic molding technique was used.

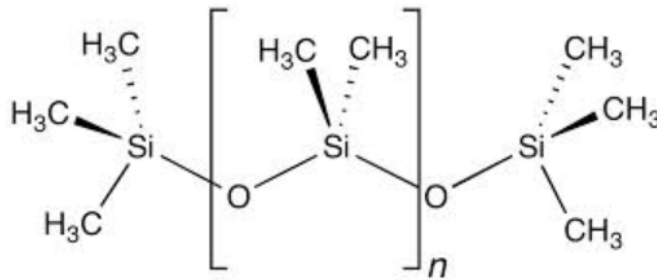


Figure 3.11: PDMS structure

The stamp was fabricated with 10:1 ratio between a base and curing agent.

In the present project the used product was *SYLGARD 184 silicone elastomer kit* from *Galindberg*.

The liquid PDMS base is poured down into a plastic glass and mixed with a cross-linking agent. The latter is added by a pipette for 10 % of the base volume.

The solution needs to be mixed very well for approximatively 5 minutes.

In order to remove bubbles from the solution the PDMS mix is put in a desiccator and pumped down to create a vacuum/low pressure. This process should last at least 30 minutes, and there should be no observables bubbles in the end.

In this project a silicon master was employed (see section 3.2) and a silanization step of the mask was needed.

The goal of silanization is to form bonds across the interface between the mineral components and the organic one. This step is simply performed moving the silicon master in a special silanization box whit a cap containig Chlorotrimethylsilane, and closing the lid of the box. The process lasts 45 minutes.

In this time the Chlorotrimethylsilane is going to evaporate and adhere on the silicon surface.

When the silanization is done, the master is placed in a plastic dish, previously covered with an aluminum foil; the PDMS mix has to be poured in it carefully, to avoid the creation of new bubbles.

The dish is then set in the oven for 2 hours at a temperature of 80 °, at the end of which the PDMS samples can be detached from the master and cut in the desired dimensions.

Once the PDMS microfluidic channels were ready, they were attached on the previously fabricated samples by means of a plasma treatment.

An oxygen plasma etching is performed on both the gold/silicon samples and the PDMS for 10 seconds. After that, the PDMS is attached to the sample and then left in the oven

at 80°C for two hours.

An example of a finished sample can be seen in figure 3.12. As can be seen from the picture

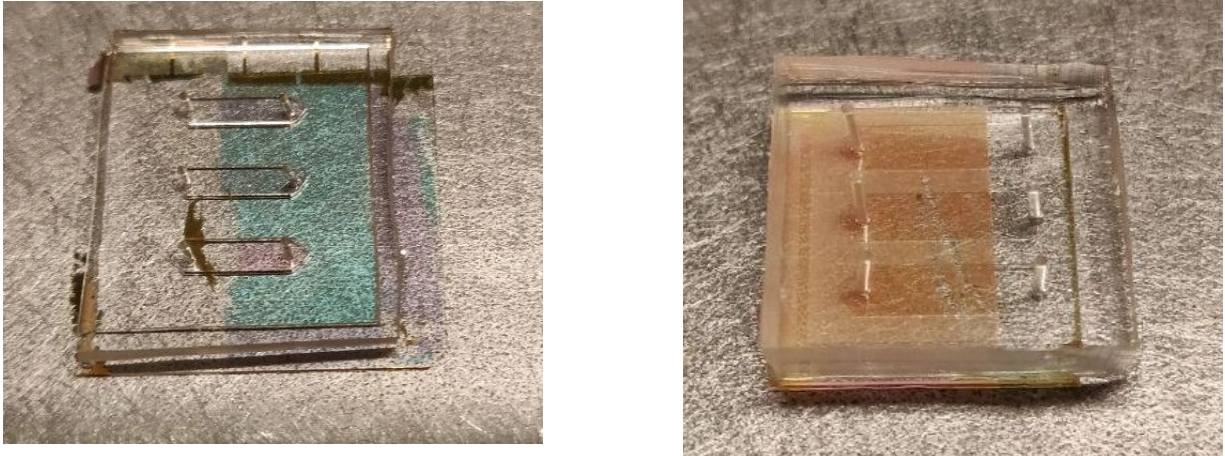


Figure 3.12: Left) Gold finished sample Right) Silicon finished sample

above, the samples are patterned just on one half of the substrate. This has been done to be able to take the reference signal on each sample at the same time. As can be seen in fig. 3.9, the sample holder can be moved horizontally, while keeping fixed the height. This allowed us to move from the patterned to the un-patterned side of the sample to take both the reference and the signal.

To flow the solutions in the micro-channels a tubing pump from *ISMATEC* was utilized. The tubes are Tygon LMT-55 from *Saint Gobain* with an internal diameter of 0.25mm. The pump was initially calibrated to set the proper flowing rate of $50 \frac{\mu\text{l}}{\text{min}}$.

3.3 Transient measurements

During the project, the extinction (see section 3.2) was collected as a function of time while changing the surrounding or local refractive index. Here we report the experimental procedure for both bulk and local sensing experiment and the variables we decided to track.

3.3.1 Resonance wavelength and Intensity

We said that in this experiment we collect the different extinction spectra when changing the refractive index in the samples' surrounding medium or locally, near the surface. Once obtained the spectrum, there are two aspect in which we're interested. The wavelength at which occur the lowest energy peak, and its intensity. The data collected on LSPR based sensors usually show a low signal to noise ratio. In order to overcome this problem, and to enhance the sensor stability, different algorithms have been proposed [6], [1]. One of this algorithm is based on the calculation of the centroid of the resonance peak [7]. The centroid is calculated on a previous fit with degree $n=20$. This fit is done to already reduce the measurement noise and to save data storage, since after that, each spectrum can be represented by just $n + 1$ values. The resonance wavelength is then calculated as:

$$\lambda_{centroid}(t) = \frac{\int_{\lambda_s}^{\lambda_s+S} \lambda(\epsilon_{fit}(\lambda, t) - \epsilon_{base})d\lambda}{\int_{\lambda_s}^{\lambda_s+S} (\epsilon_{fit}(\lambda, t) - \epsilon_{base})d\lambda} \quad (3.7)$$

where ϵ_{fit} represents the fitted spectrum, S is a wavelength span which defines the region of the spectrum used for the calculation. This value S is fitted to ϵ_{fit} to provide the left point of the interval of length S .

$$\epsilon_{fit}(\lambda) - \epsilon_{fit}(\lambda + S) = 0 \quad (3.8)$$

Once know this left point λ_s we can calculate the baseline value ϵ_{base} from:

$$\epsilon_{base} = \epsilon_{fit}(\lambda_s) = \epsilon_{fit}(\lambda_s + S) \quad (3.9)$$

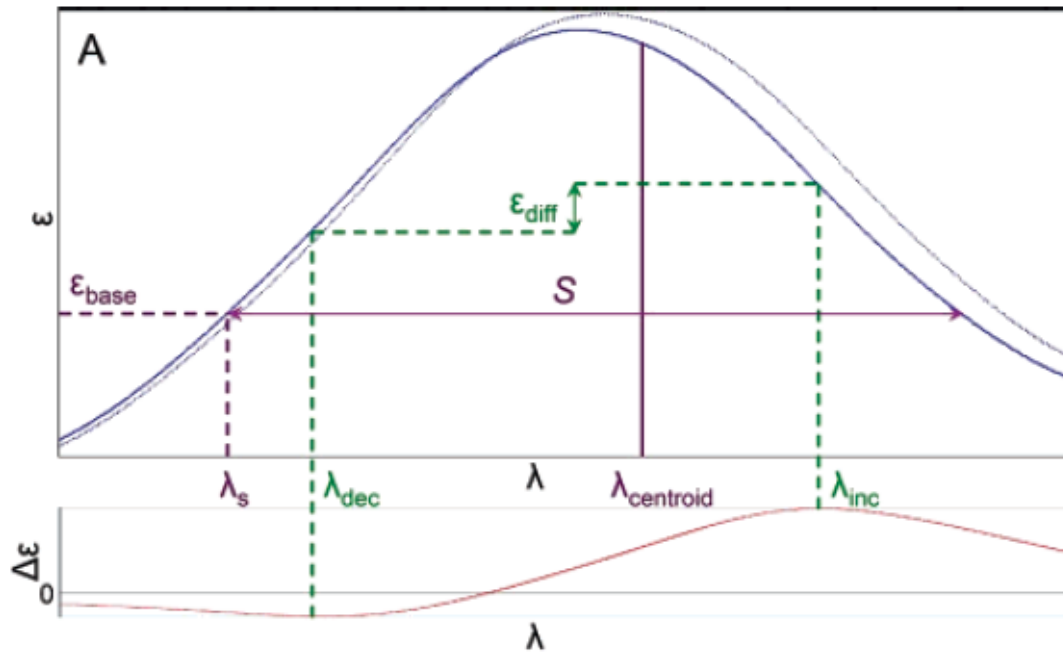


Figure 3.13: Parameters used in the centroid calculation [7].

The intensity of the peak, is then calculated at $\lambda_{centroid}$. These algorithm were proposed for LSPR based sensors, since they usually provide a smaller signal to noise ratio compared to surface plasmon resonance (SPR) based sensors [5],[9]. Despite this we will apply the same algorithm for the gold and silicon samples.

3.3.2 Bulk sensing: experimental procedure

The purpose of the bulk sensing was to investigate the sensitivity of the two different nanostructures to the refractive index change of the surrounding medium.

Different solutions of ethylene glycol at different concentrations have been prepared, respectively 2.5%, 5%, 7.5% and 10%. Ethylene glycol is an organic compound moderately toxic with formula $(CH_2OH)_2$. The refractive index of ethylene glycole aqueous solutions can be calculated from the formula [24]:

$$n = 1.3325 + 0.000982x \quad (3.10)$$

where x represents the weigth percentage of ethylene glycole.

From this we see that the refractive index of the ethylene glycol can be tuned from 1.33 to 1.43.

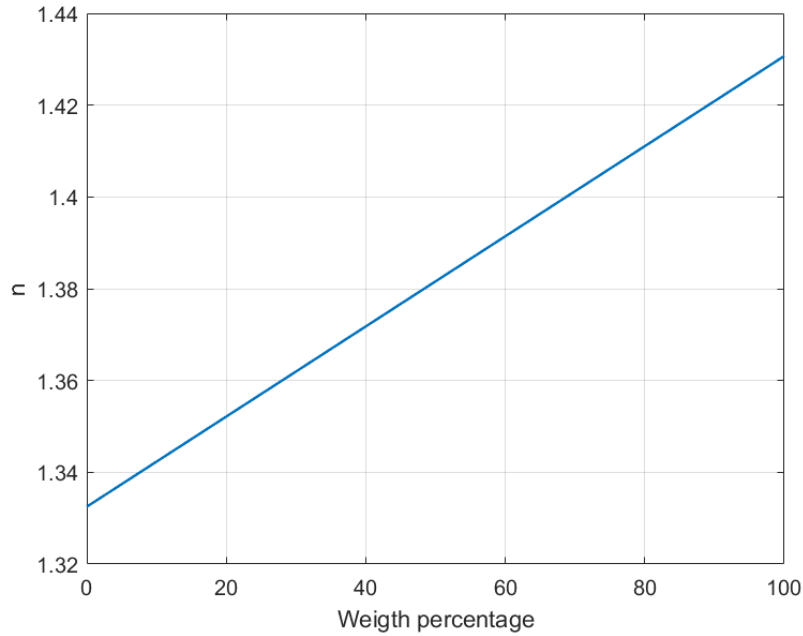


Figure 3.14: Refractive indices of aqueous ethylene glycol solutions at 25°C.

We thus have:

	0%	2.5%	5%	7.5%	10%
refractive index	1.3325	1.334955	1.33741	1.339855	1.34232

We first measure the noise induced by the pump.

To do so, the position of the resonance wavelength has been monitored for different flow rates of 0, 20, 50 and 80 $\frac{\mu\text{l}}{\text{min}}$ (see subsection 3.3.1 on details about peak monitoring).

The peak position has been fit with 1° degree polynomial and subtracted to the original signal. Each flow rate has been measured for circa 30 minutes.

The standard deviation of each signal has then been calculated.

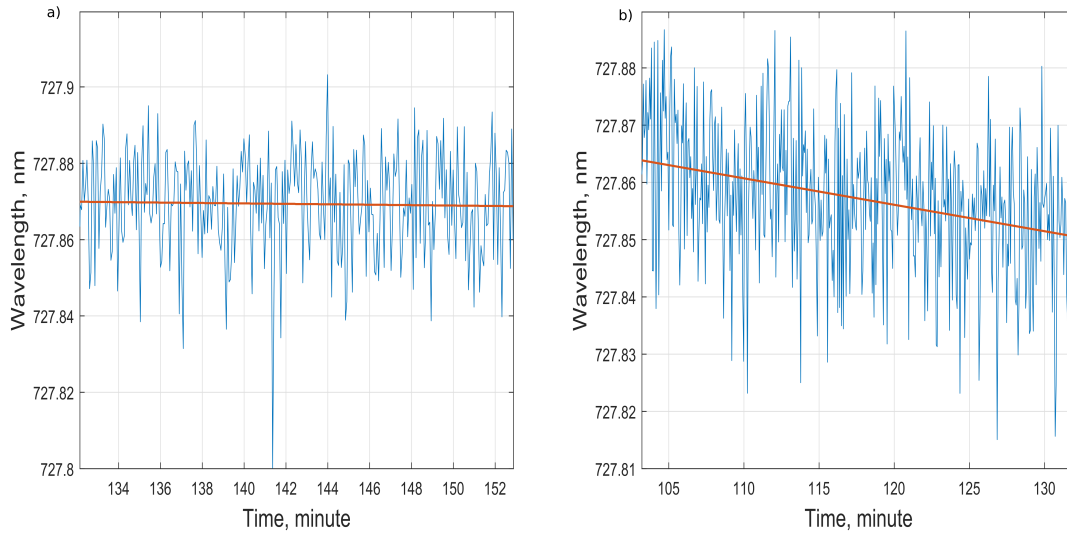


Figure 3.15: a) Resonance peak variation with static flow b) Resonance peak variation with a 20 $\frac{\mu\text{l}}{\text{min}}$ flow.

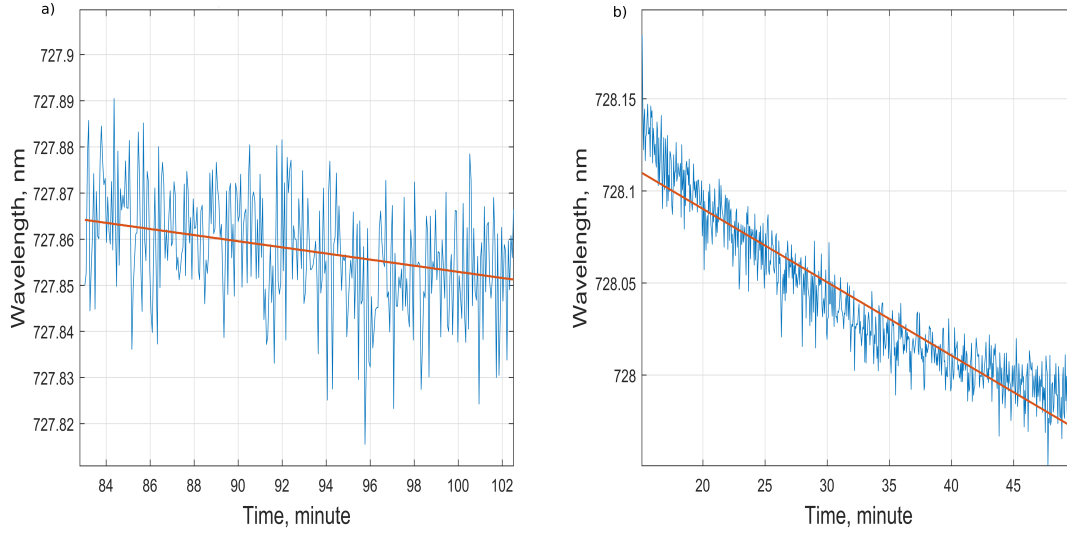


Figure 3.16: a) Resonance peak variation with $50 \frac{\mu l}{min}$ b) Resonance peak variation with $80 \frac{\mu l}{min}$.

	no flow	$20 \frac{\mu l}{min}$	$50 \frac{\mu l}{min}$	$80 \frac{\mu l}{min}$
standard deviation	0.0137	0.0121	0.0124	0.0310

As can be seen from these pictures, increasing the flow rate we notice a drift of the signal. A possible explanation, is that this is due to a reshape of the nanodisks [26], [12]. For the gold samples, the drift in fact is in the blue, which could be in agreement with the expected particles' reshape. Starting from nanodisks in fact, to minimize the surface tensions these would tend to a more spherical form. As we have seen in *Chapter 2*, spherical nanoparticles would resonate at shorter wavelengths with respect to nanodisks.

To have a good trade-off between the lowest standard deviation and the measurements' velocity a flow rate of $50 \frac{\mu l}{min}$ has been chosen and used for all the measurements taken in the project.

For the extinction spectra measurements, initial extinction and reference spectra were measured both in air and in de-ionized water.

The sample was left in water flow for 2 to 4 hours to let the system stabilize.

Starting from water, each solution was flowed for ten minutes while tracking the extinction response.

When changing the solution, the pump was stopped in order to avoid the formation of bubbles in the microfluidic channel.

For the same reason both the water and the ethylene glycol solutions have been sonicated for 30 minutes before each measurement.

To ensure the good behaviour of the experiment the extinction spectra has been measured for both increasing and decreasing ethylene glycol concentration.

3.3.3 Bio-sensing: experimental procedure

The purpose of the local sensing was to investigate the surface sensitivity of the two samples.

To do so, the surface of the sample has been functionalized with layers of bovine serum albumin (BSA), a serum albumin protein derived from cows.

To do that a precise procedure and three different solutions were used [25].

After the sample stabilization in water a Citrate buffer (10mM sodium citrate, 1mM sodium hydroxide, pH 4 at 25°C) was flowed for 5 minutes.

The first layer is created by flowing the BSA solution (500 $\mu\text{g}/\text{ml}$), for approximately 10 minutes.

After that, the sample is first washed for 5 minutes with the buffer solution in order to remove the unbounded molecules, and then with a solution of dextrane sulfate (DS) (1mg/ml) for 10 minutes.

The DS molecules are negatively charged in water, and so are adsorbed electrostatically to the positively charged surface of the BSA layer, making possible the formation of the next BSA layer.

The procedure is repeated a number of time equal to the number of layer to be deposited and each cycle creates a BSA layer with thickness around 5nm [13]. A simple sketch of the used protocol for the biosensing experimet can be seen in fig. 3.17.

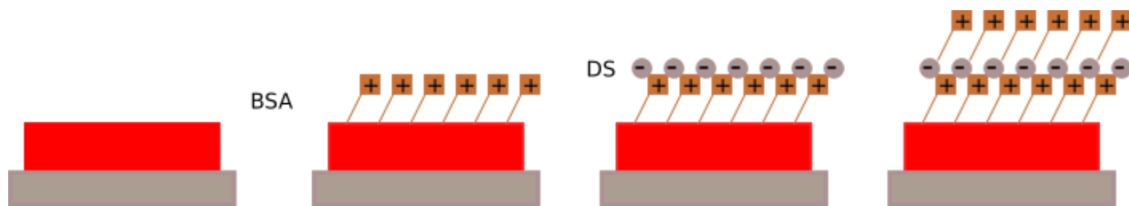


Figure 3.17: Schematic of the protocol used to grow the BSA layer on the samples' surface. From left to right: nanodisk, growth of the first BSA layer, adsorption of DS molecules, growth of the second BSA layer.

CHAPTER 4

Results and discussion

In this chapter the results of the measurements are presented and the analysis performed for the different samples are discussed. In the first part of the chapter we present a discussion on the measured extinction spectra and of their behaviour with respect to the expectations derived from the simulations presented in *Chapter 2*. We will then focus on the bulk sensing and on the main parameters that we decided to monitor, presenting the behaviour of the samples responding to the variation of the refractive index of the surrounding environment. As we will discuss in more details along the chapter, the parameter of main interest is the sensitivity. We defined two different sensitivities, one which takes into account the shift of the resonance wavelength of the lowest energy (or highest wavelength) mode, and one which takes into account the shift in the intensity at the same wavelength. In the last part we discuss the local sensing experiment, in which we changed locally the RI near the nanodisks surface growing different layers of BSA. The shift of the resonance wavelength is monitored in dependence of the number of grown layers. All the simulations we will refer to in this chapter can be found in *Chapter 2*.

4.1 Extinction spectra

The very first property that we have measured is the extinction spectrum of the two nanostructures to see their differences.

As described in *Chapter 2* the extinction spectra tell us the amount of light lost in the interaction with the sample. The extinction is defined as the sum of the light absorbed and reflected, as scattering is equal to zero.

The spectrum depends both on the nanostructure's shape and dimension and on the surrounding medium's refractive index. We present in the next subsections the extinction spectra for Gold, as a function of disks diameter, and for Silicon as a function of both diameter and thickness, in air ($n=1$).

4.1.1 Extinction spectra of Gold

We first measured the extinction of gold nanodisks with diameter of 100 nm and 150 nm and a thickness of 30 nm. The fabrication details and the SEM are shown in *Chapter 3*. The spectra of the two samples can be seen in [fig. 4.1](#).

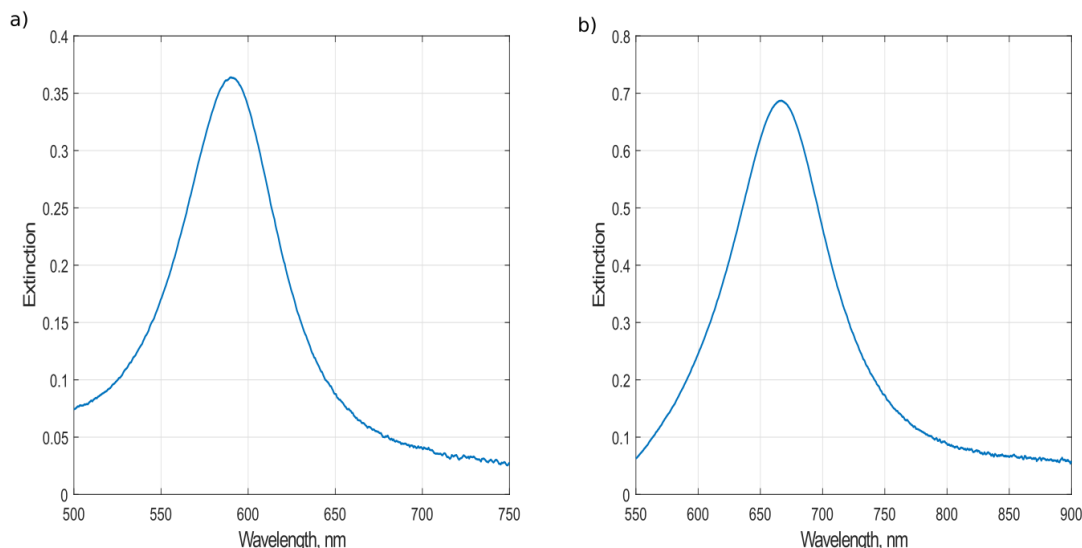


Figure 4.1: a) Extinction spectrum in air of gold nanodisks with diameter 100 nm b) Extinction spectrum in air of gold nanodisks with diameter 150 nm.

The experimental spectra agree with the simulations: as expected we observe a single peak related to LSPR. The peak red shifts and increases in intensity when increasing the diameter of the disks.

4.1.2 Extinction spectra of Silicon

Extinction spectra of silicon nanodisks were measured as a function of disks' diameter and thickness. For this reason several samples with different diameters and disks' height have been measured.

The dependency on these two parameters is shown in fig. 4.2

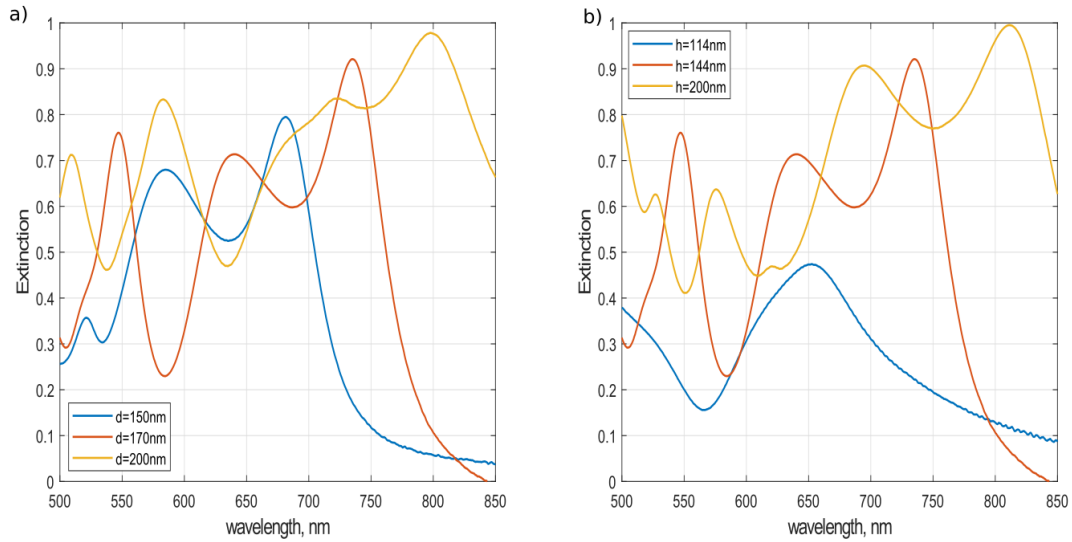


Figure 4.2: a) Extinction spectra of Silicon nanodisks in dependence of the diameter for a thickness of 144 nm b) Extinction spectra of Silicon nanodisks in dependence of the thickness for 170 nm diameter.

As predicted by the simulations, the spectra show several resonances which depend on the exact nanodisk geometry. When the thickness is kept constant, we see a red shift of the lowest energy peak and an increase of the intensity when increasing the diameter. Furthermore additional peaks start to appear. The same applies when we kept constant the diameter.

Monitoring how the magnetic and electric dipole shift increasing the diameter (of nanodisk of thickness 144 nm), it can be noticed that the distance in nm between the two decreases. This behaviour can be seen in fig. 4.3.

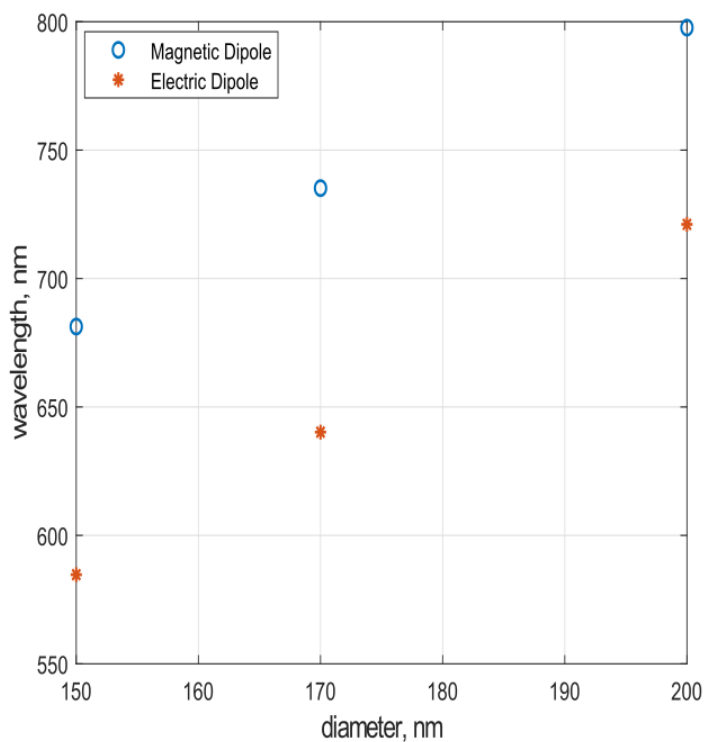


Figure 4.3: Variation of wavelength at which the magnetic and electric dipole modes appear in dependence of the diameter.

Even if the study has been done just for three different diameters, this behaviour agrees with the literature. It has been shown in fact, that the diameter can be tuned, changing the samples dimensions, to exhibit the magnetic and electric resonance at the same wavelength [31].

4.2 Bulk sensing

As briefly described in *Chapter 3*, for the bulk sensing measurements, the spectra of each sample has been monitored while flowing DI water and solutions of ethylen glycole at different concentrations. Each solution was flowed for constant time, starting from DI water to 10% ethylen glycole and vice versa. For the two different structures we were interested in different properties.

From the simulations on the gold structure is visible both a red shift of the spectra, when increasing the refractive index, and an increase of the intensity related to the peak.

For this structure then we decided to monitor the wavelength at which the resonance occur while changing the surrounding refractive index.

From the simulation on Silicon instead is clearly visible a decrease of the intensity when increasing the refractive index, while the shift of the resonance wavelength corresponding to the lowest energy, the magnetic dipole, is less evident; we decided then to monitor the variations in the intensity at the magnetic dipole resonance.

4.2.1 Gold

As said before for gold we concentrated on two different diameter dimensions, respectively 100 nm and 150 nm. The first thing we have done, was to check the extinction behaviour of the structure when it is immersed in DI water. This correspond to a change in the refractive index from $n=1$ (air) to $n \simeq 1.33$ (DI water). The spectra behaviour can be seen in fig. 4.4.

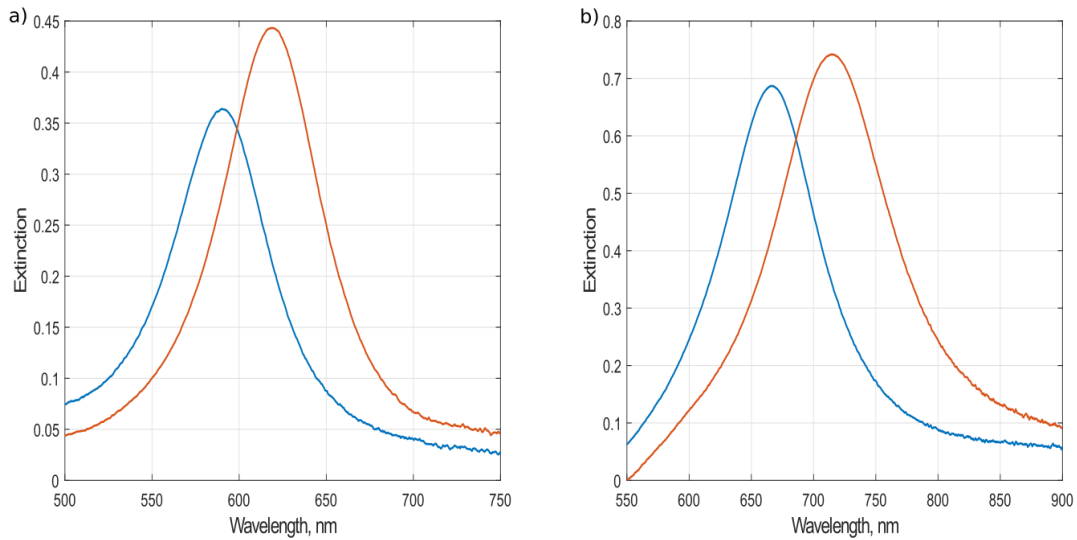


Figure 4.4: a) Gold nanodisk diam=100 nm b) Gold nanodisk diam=150 nm. The blue line represents the spectra in air while the red line represents the spectra in DI water.

As expected for both the structures we observe the spectra redshift and an increase of the intensity. We can see that the shift in the resonance wavelength for the structure in fig. 4.4 a) is of 27.93 nm while for the one in fig. 4.4 b) is of 47.9 nm, while the intensity changes respectively of 0.076 and 0.055 arbitrary unit. This gives us already a clue on the different sensitivity of the structure, which seems to depend on the structures dimensions. As mentioned before, we were interested in monitor the change in the resonance wavelength while changing the refractive index. The results of this measurements can be seen in fig. 4.5.

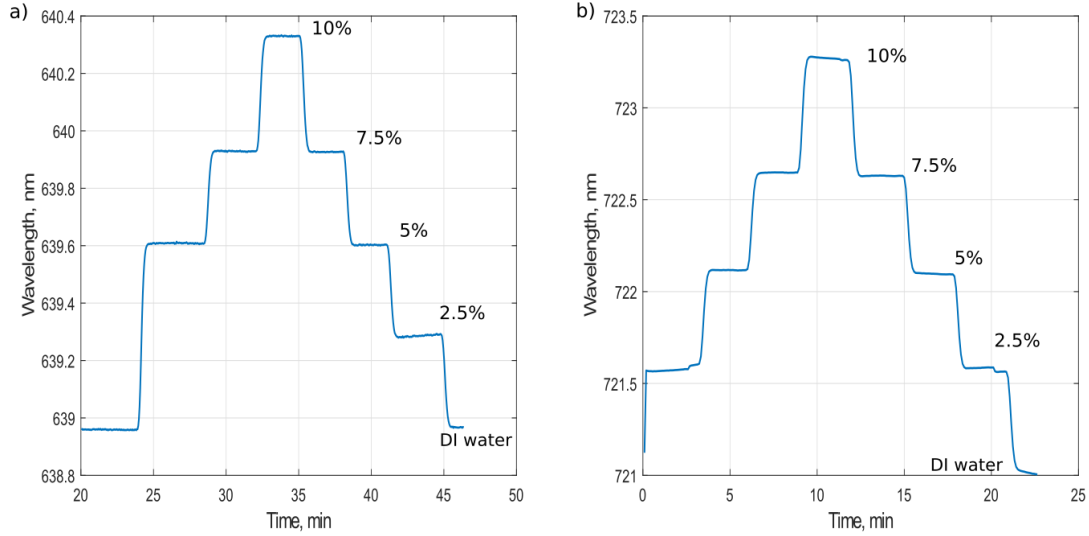


Figure 4.5: a) Gold nanodisk diam=100 nm b) Gold nanodisk diam=150 nm. Variation in time of the resonance peak in dependence of ethylen glycole concentration.

In the figure we can identify the different steps corresponding to the different concentrations of ethylen glycole. For the first sample the step corresponding to the 2.5% concentration is missing, but since the rest of the measure seemed consistent and good we decided to keep it.

In both the structures the shift for each step results almost constant. The total shift between DI water and 10% ethylen glycole results in circa 1.37 nm for the first structure and circa 2.27 nm for the second one. This agrees with the behaviour of the spectra showing the better sensitivity of the second sample.

The SNR has been calculated as well, and it results higher for the second structure where it is equal to 385.9 with respect to the 312.9 of the first structure.

In order to compare these samples to the silicon ones we wanted to look also at the intensity variations. Starting from the raw data we calculated the difference in intensity for each wavelength, which can be seen in fig. 4.6.

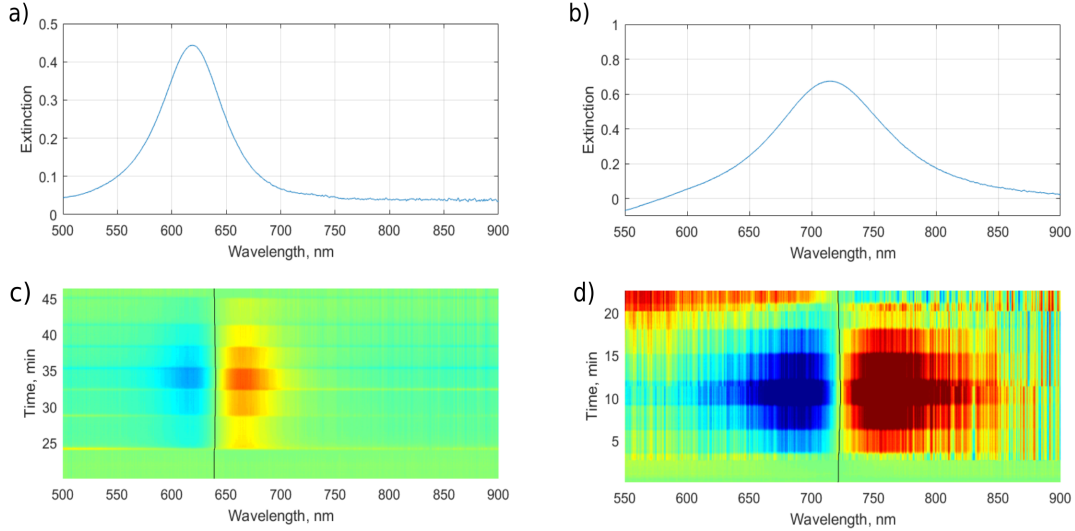


Figure 4.6: a) Extinction spectra of gold nanodisks with diam=100 nm b) a) Extinction spectra of gold nanodisks with diam=150 nm. c) d) Intensity differences as a function of time and wavelength.

In fig. 4.6 a) and b) we report the extinction spectra in water, while in fig. 4.6 c) and d) we report the difference in intensities with respect to wavelength and time. The color scale used is the same for both the structures: this highlights how the second sample shows a more sensitive behaviour not only with respect to the peak shift and with respect to the intensity.

We decided to measure the variables of interest at the wavelength corresponding to the lowest energy mode: $\lambda \simeq 638$ for the Gold sample with diameter 100 nm and $\lambda \simeq 721$ for the one with diameter 150 nm. From fig. 4.7 and interesting property is visible.

The highest change in the intensity do not occur at the resonance wavelength.

From sensing purposes could be then interesting to monitor the properties of interest at that particular wavelength instead that at the resonance one.

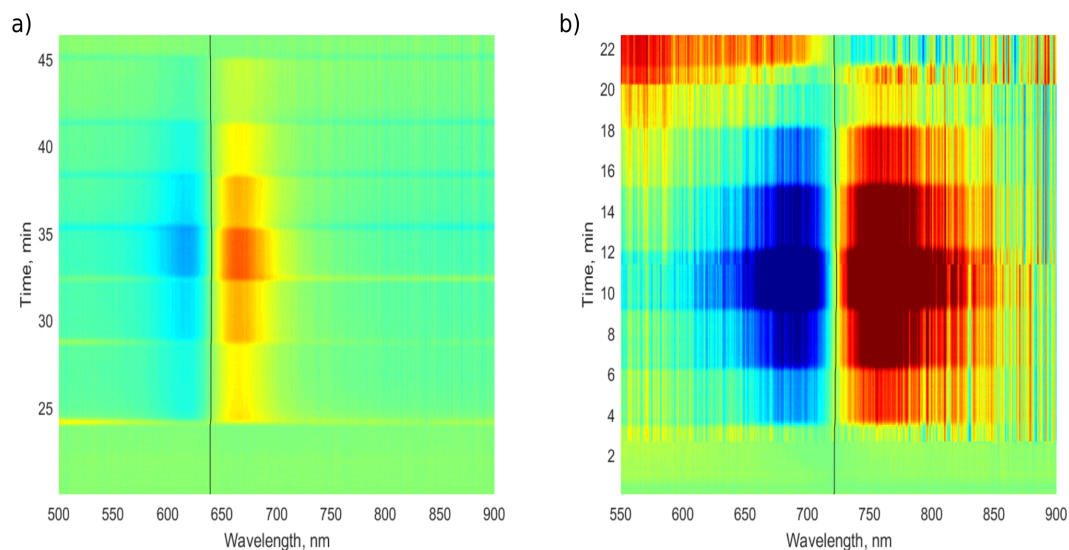


Figure 4.7: a) Gold nanodisk diam=100 nm b) Gold nanodisk diam=150 nm. Intensities differences for each wavelength with reduced range.

At last we decided to plot the differences in intensity with respect to the wavelength and the refractive index. This can be seen in fig. 4.8.

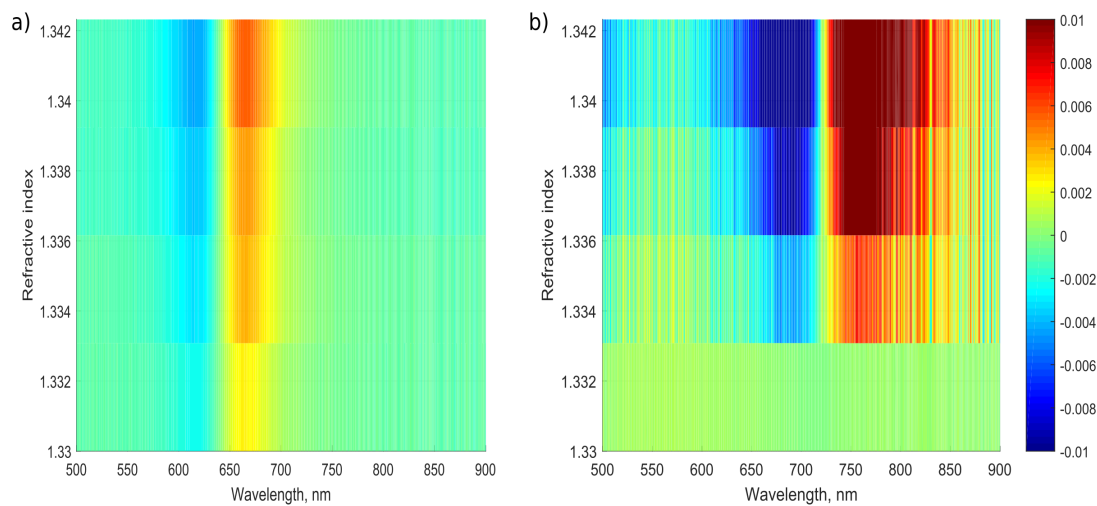


Figure 4.8: a) Gold nanodisk diam=100 nm b) Gold nanodisk diam=150 nm. Intensities differences for each wavelength and refractive index variation.

In this picture it's easy to recognize the different steps, corresponding to the different concentrations of ethylen glicole. It is also easy to notice that increasing the concentration the differences in intensity increase, reaching their maximum for the 10% glicole concentration.

The parameter we are really interested in for the sensing purposes is the sensitivity of the structure. This is defined as:

$$sens = \frac{\Delta\lambda}{\Delta n} \quad (4.1)$$

We calculated this value at the resonance wavelength obtaining what can be seen in fig. 4.9.

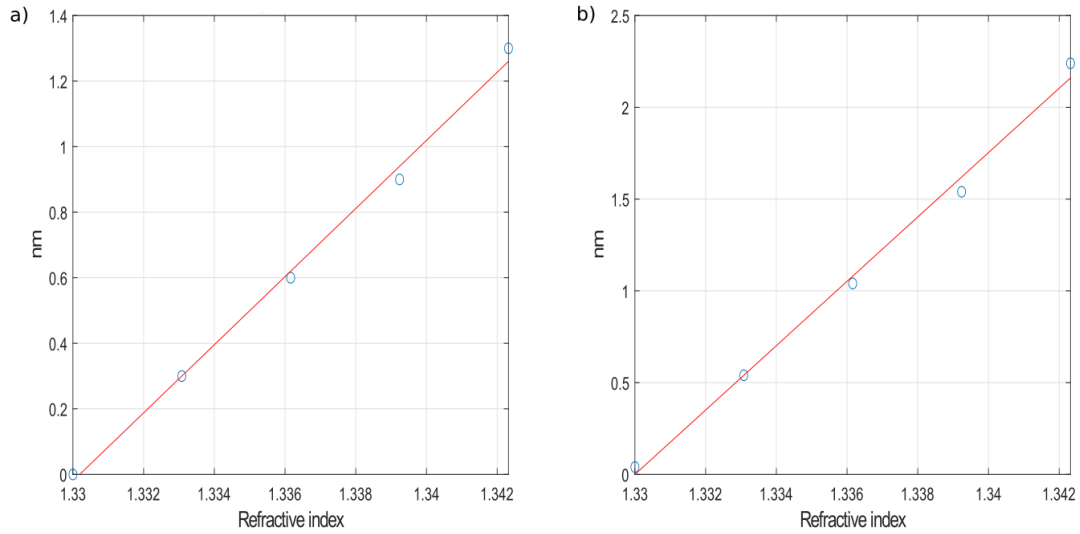


Figure 4.9: a) Gold nanodisk diam=100 nm b) Gold nanodisk diam=150 nm. Sensitivity calculated at the resonance wavelength.

As expected the structure with the largest diameter presents higher sensitivity. However, we decided to look at the sensitivity not only for this wavelength but for the entire spectrum. What we obtained can be seen in fig. 4.10.

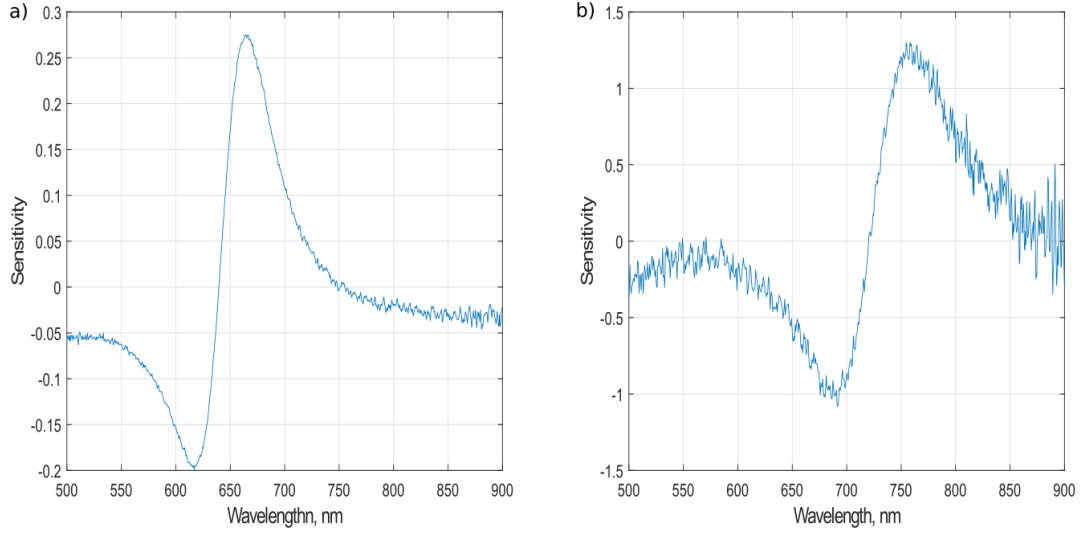


Figure 4.10: a) Gold nanodisk diam=100 nm b) Gold nanodisk diam=150 nm. Sensitivity as a function of the wavelength.

Plotting the sensitivity in function of the wavelength, we obtain an outlook on the system, which tell us at which wavelengths the system show the biggest variations in intensity. This can be useful for example, if further single wavelength measurements are needed. From the graphs in fig. 4.10 we obtain then the wavelength at which the structure is more responsive, which it appears to be different to the resonance one. From these measurements we see that the second structure seems to be the most sensitive between the two, to the refractive index variations. We will use then this structure for the local sensing measurements.

A table with a summary of the results can be seen below.

	Sample 1	Sample 2
λ_{res} air, (nm)	590.2	666.3
λ_{res} water, (nm)	619.3	714.2
λ_{res} shift from air to water, (nm)	27.9	47.42
λ_{res} shift from water to 10% glicole, (nm)	1.37	2.27
Intensity difference, (a.u.)	0.076	0.0549
Sensitivity, (nm/RIU)	103.9	175
λ highest sensitivity, (nm)	663.45	758.1

4.3 Silicon

For Silicon the same kind of analysis has been performed. Different samples with different diameters and thicknesses has been measured.

For the first part of this subsection we will focus on disks of 144 nm of thickness and 150,170 and 200 nm of diameter. At first we check for the behaviour of the extinction spectra when changing the surrounding medium from air to water. The extinction spectra can be seen in fig. 4.11

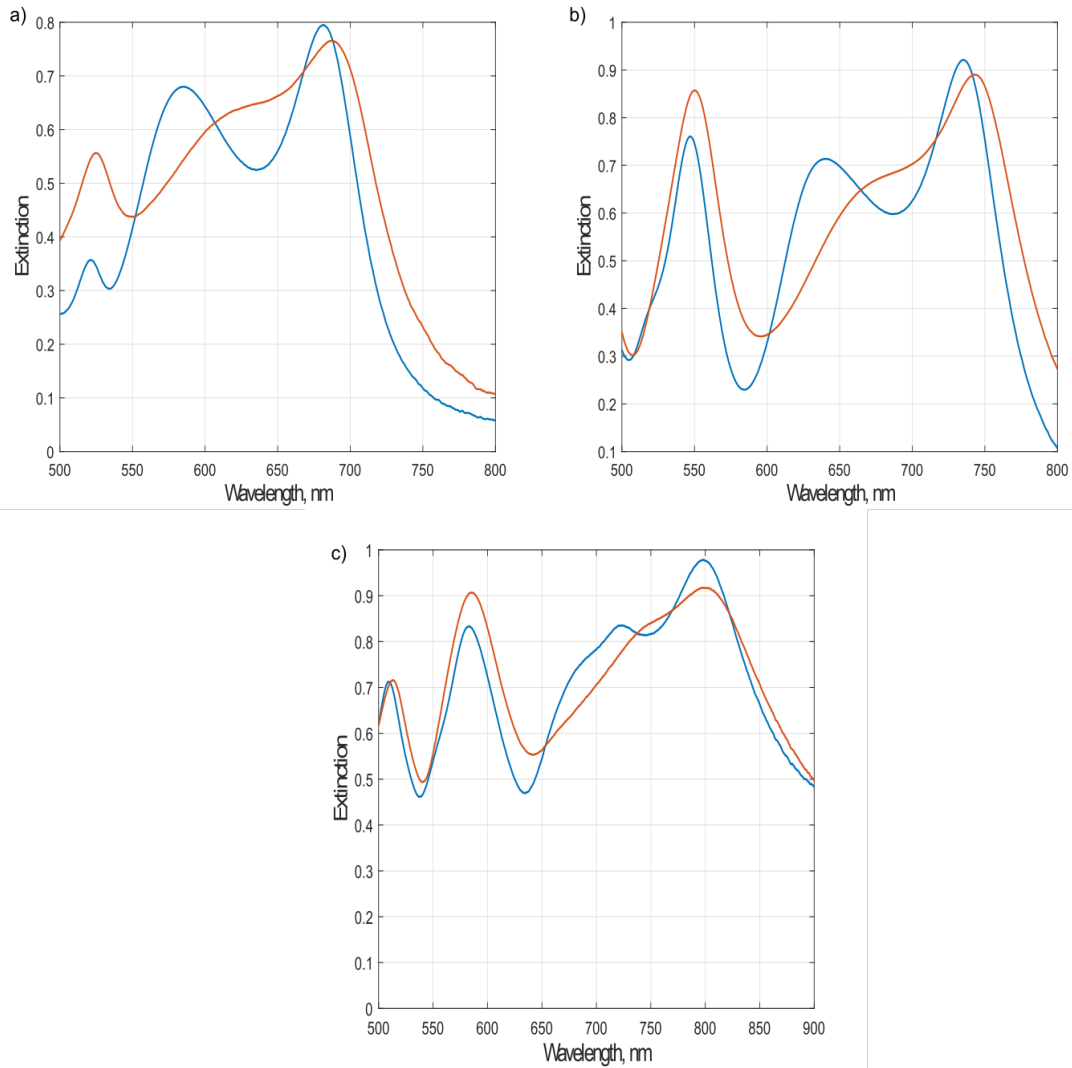


Figure 4.11: Extinction spectra in air and DI water. Blu line spectra in air, red line spectra in DI water. a) Silicon nanodisk $d=150$ nm b) Silicon nanodisk $d=170$ nm. c) Silicon nanodisk, $d=200$ nm.

As expected from the simulations, we notice a red shift of the resonance wavelength of the different modes when increasing the refractive index. We also measure a decrease of the intensity for the magnetic and electric dipole mode, while we measure an increase when looking at the quadrupolar mode.

It can be discussed that there seems to exist a trade off between the diameter and the thickness of the disk. The sample which presents the best spectrum is the one with a 170 nm as diameter. In this case three different modes can be clearly recognized, and each of them is well defined. For Silicon we decided to monitor the variation in intensity when changing refractive index. The behaviour can be seen in fig. 4.13

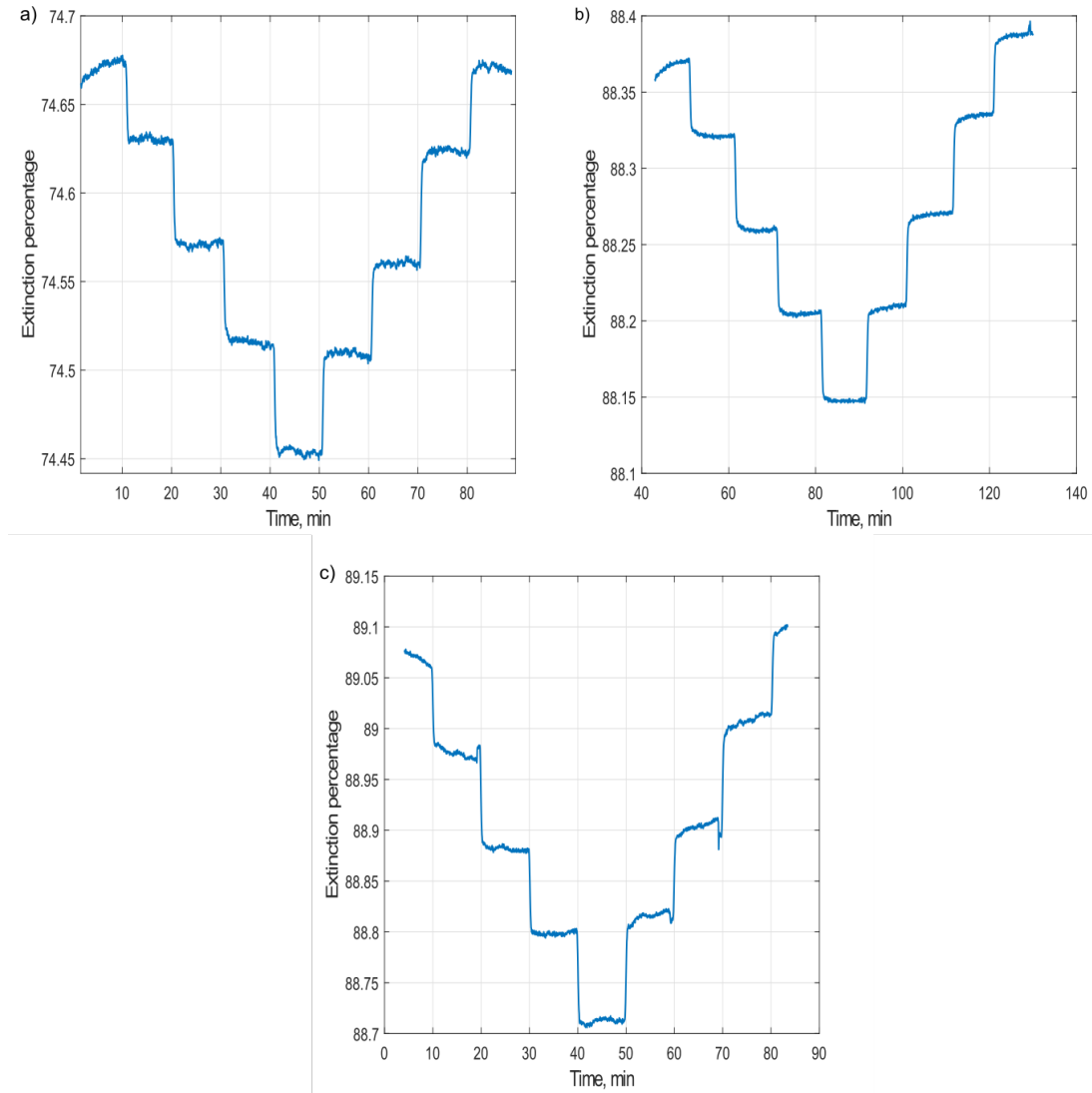


Figure 4.12: Variation of intensity when changing refractive index from DI water to different concentrations of ethylene glycol a) Silicon nanodisk $d=150$ nm b) Silicon nanodisk $d=170$ nm. c) Silicon nanodisk, $d=200$ nm.

In this picture what we see is the value of the intensity at the centroid wavelength, which refers to the peak wavelength.

From the picture we see that the intensity variations are really small, however we are able to detect them.

Despite the peak shift expected to be very small, we decided to try to monitor that as well. For some of the samples the measurement wasn't good enough; we present then here the peak shift for the sample with diameter of 150 nm and 170 nm respectively.

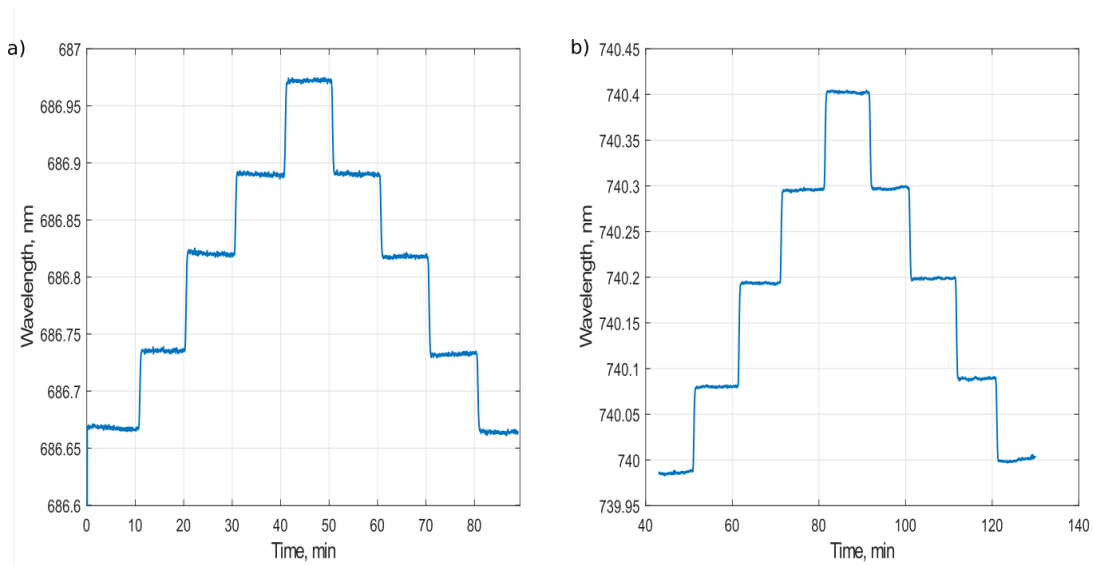


Figure 4.13: Variation of intensity when changing refractive index from DI water to different concentrations of ethylen glycole a) Silicon nanodisk d=150 nm b) Silicon nanodisk d=170 nm.

As for gold we were interested in the sensitivity of these samples. In this case we defined two different sensitivities, related to the intensity shift and on the peak shift.

$$S_{bulk,int} = \frac{\Delta I}{\Delta n} \quad (4.2)$$

$$S_{bulk,peak} = \frac{\Delta \lambda}{\Delta n} \quad (4.3)$$

As can be seen in fig. 4.14, we extrapolated the value of the intensity and/or of the peak and plotted as a function of the refractive index.

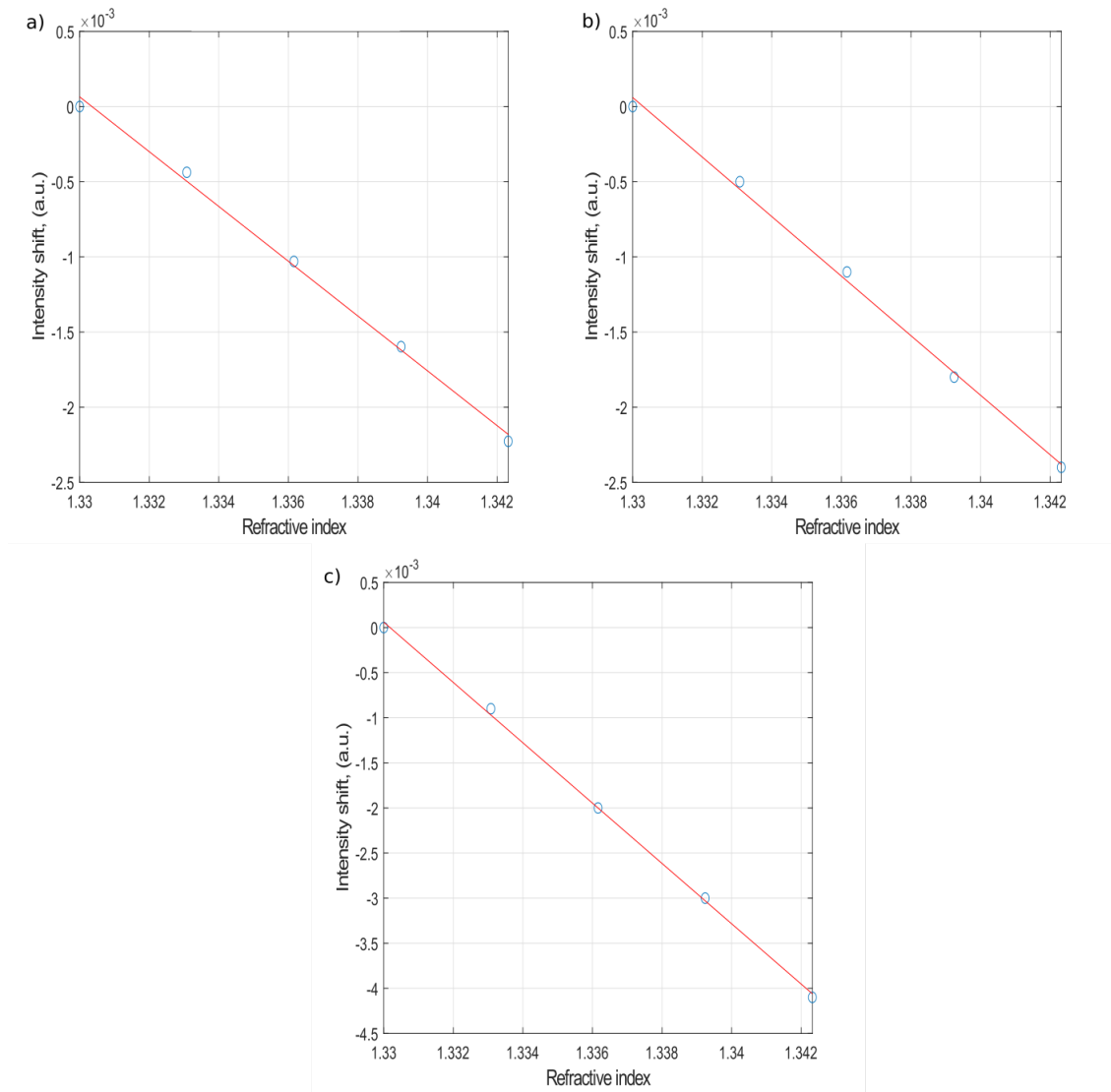


Figure 4.14: Sensitivity with respect to intensity when changing refractive index from DI water to different concentrations of ethylene glycol a) Silicon nanodisk $d=150$ nm b) Silicon nanodisk $d=170$ nm.

For what concern intensity, the sensitivity value are quite low, and the best value is the one for the 200 nm in diameter sample. In fig. 4.15 we can see the same type on plot for the resonance peak.

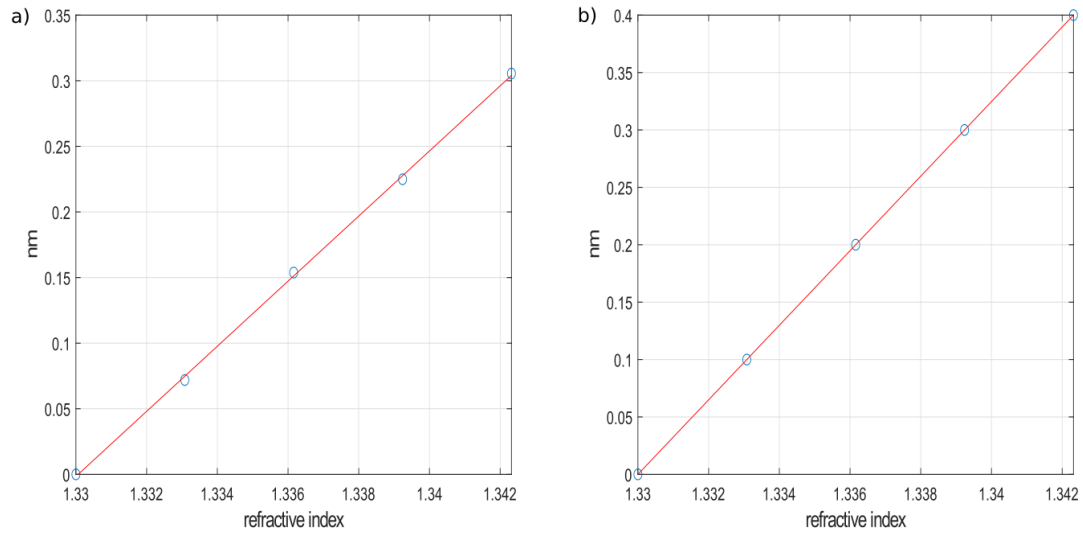


Figure 4.15: Sensitivity with respect to resonance wavelength when changing refractive index from DI water to different concentrations of ethylen glicole a) Silicon nanodisk $d=150$ nm b) Silicon nanodisk $d=170$ nm.

We notice that when looking at the peak shift, the sample giving the best sensitivity is the one with a diameter of 170 nm. Looking at the spectra, it seems like the biggest differences don't actually occur at the resonance.

As for gold we analyzed the intensity differences for each wavelength, as can be seen in fig. 4.16

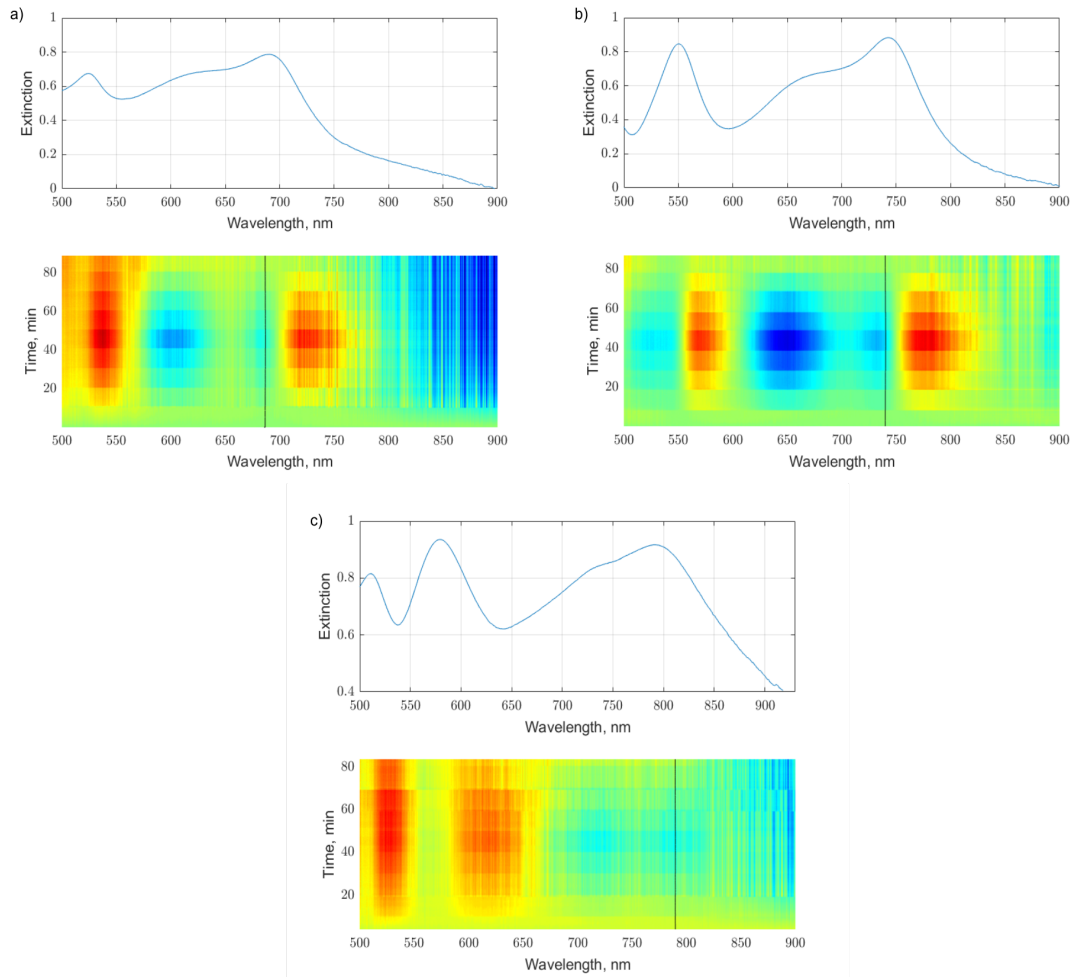


Figure 4.16: Intensities differences with respect to time and wavelength a) Silicon nanodisk $d=150$ nm b) Silicon nanodisk $d=170$ nm c) Silicon nanodisk $d=200$ nm.

As expected from the spectra we notice that the highest changes occur at the right shoulder of the resonance for every structure. And we notice that the quadrupolar mode give rise to quite high differences while the electric dipole rarely plays a big role. This can be better seen in fig. 4.17, where a zoom is presented.

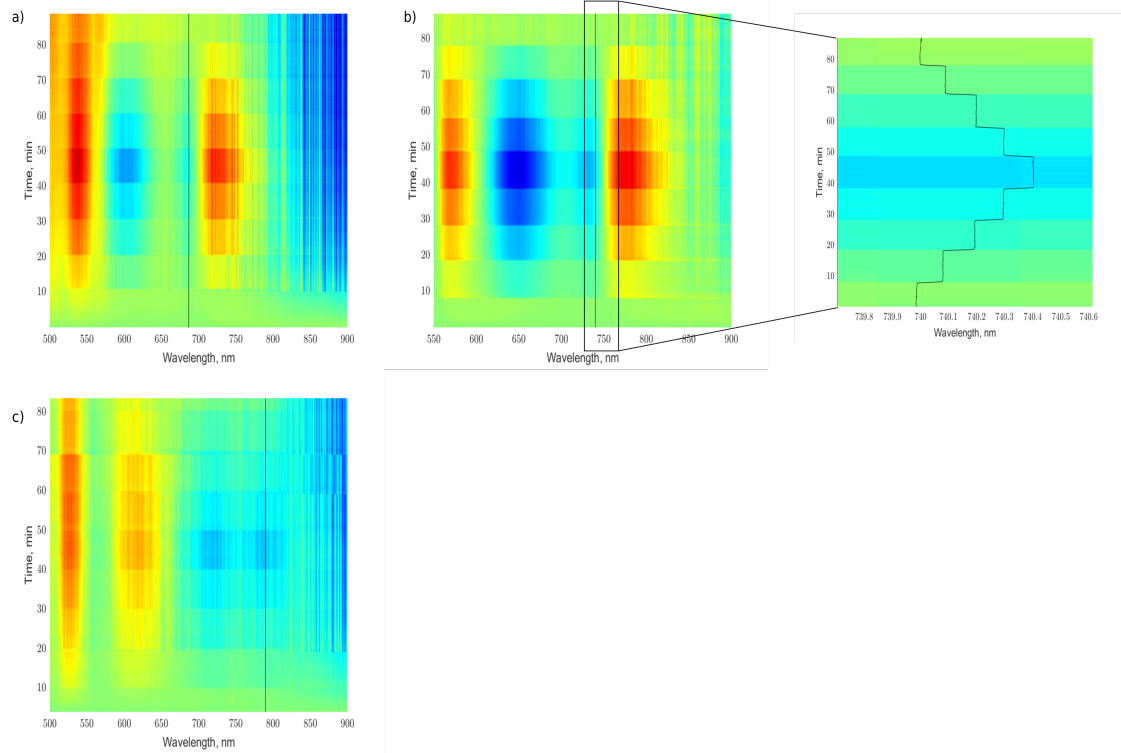


Figure 4.17: Intensities differences with respect to time and wavelength a) Silicon nanodisk $d=150$ nm b) Silicon nanodisk $d=170$ nm c) Silicon nanodisk $d=200$ nm.

In the end we plotted, as for gold, the intensity sensitivity for each wavelength, as can be seen in fig. 4.18.

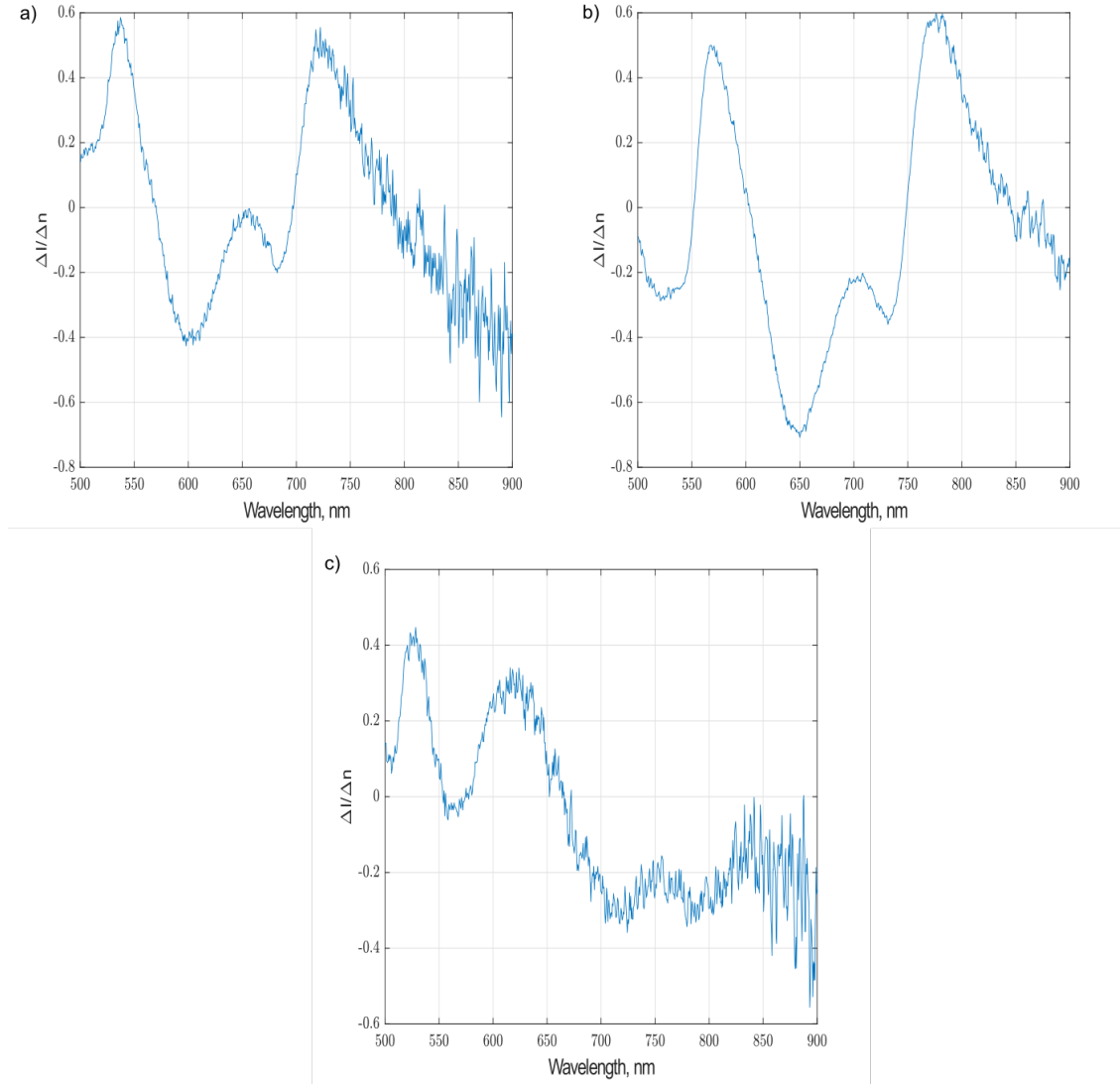


Figure 4.18: Sensitivity defined as $\frac{\Delta I}{\Delta n}$ for each wavelength a) Silicon nanodisk $d=150$ nm b) Silicon nanodisk $d=170$ nm c) Silicon nanodisk $d=200$ nm. Disk height = 144 nm.

From the picture above, what we notice is that all the sample reach a high sensitivity near the quadrupolar mode, and the first two present a high sensitivity also near the magnetic dipole mode.

The same analysis has been performed for Silicon nanodisk of different thickness. We report the result concerning the sensitivities for two samples of thickness 200 nm and diameter 150 nm and 170 nm respectively.

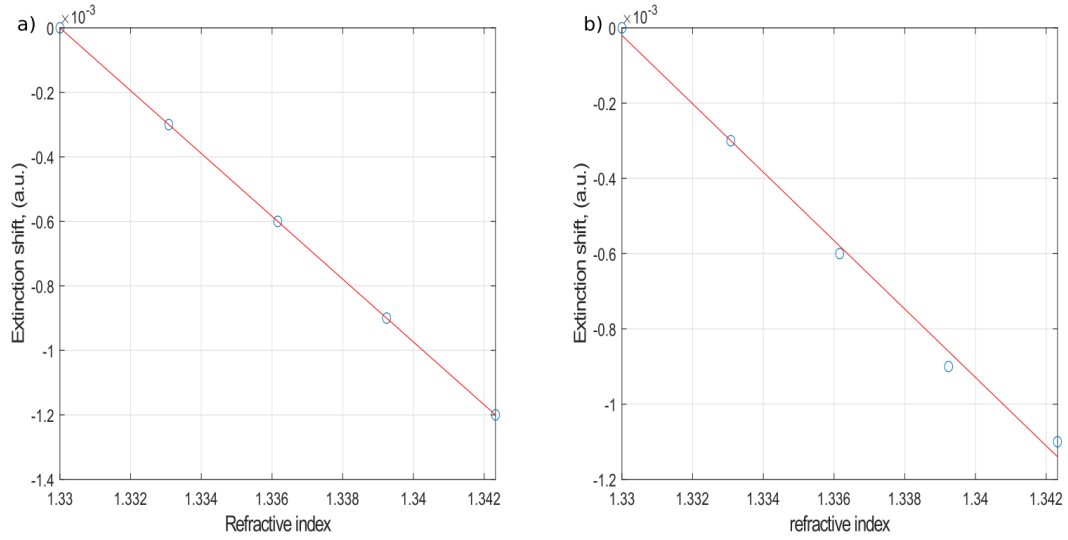


Figure 4.19: Sensitivity defined as $\frac{\Delta I}{\Delta n}$ calculated at λ_{res} a) Silicon nanodisk $d=150$ nm b) Silicon nanodisk $d=170$ nm. Disk height = 200 nm.

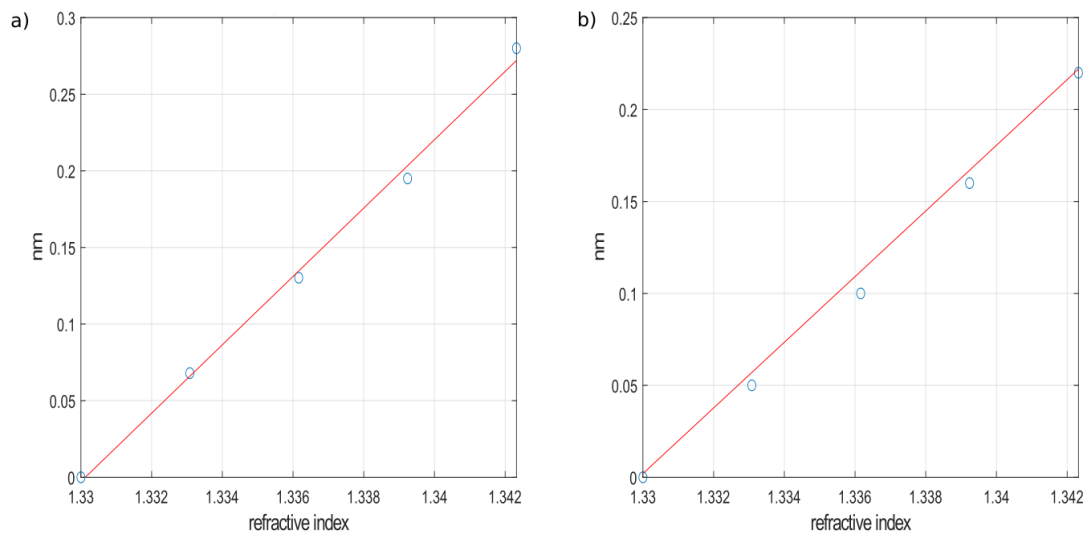


Figure 4.20: Sensitivity defined as $\frac{\Delta \lambda}{\Delta n}$ calculated at λ_{res} a) Silicon nanodisk $d=150$ nm b) Silicon nanodisk $d=170$ nm. Disk height = 200 nm.

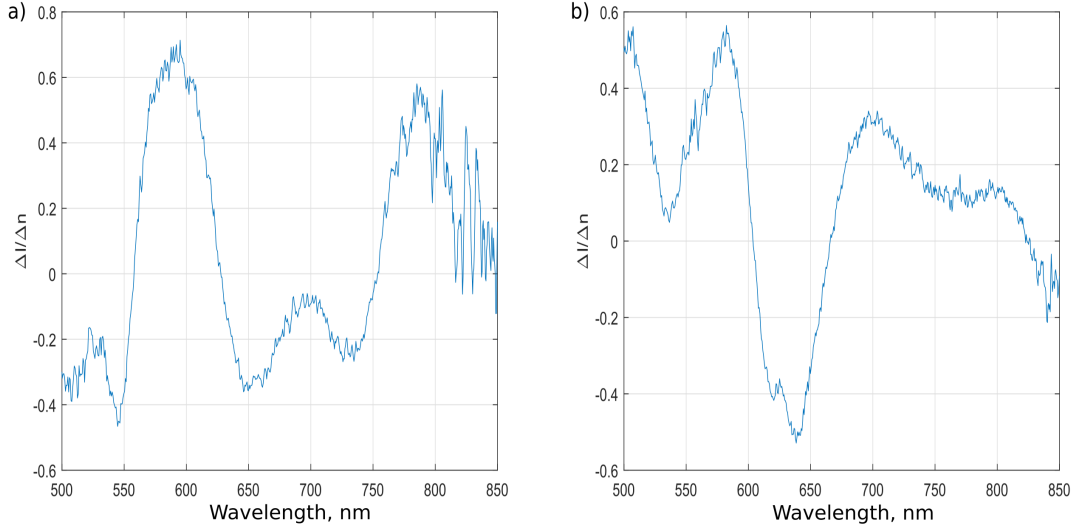


Figure 4.21: Sensitivity defined as $\frac{\Delta I}{\Delta n}$ for each wavelength a) Silicon nanodisk $d=150$ nm b) Silicon nanodisk $d=170$ nm. Disk height = 200 nm.

Above a table with the summary of the results is presented:

	Sample 1	Sample 2	Sample 3
λ_{res} air, (nm)	681.2	735.2	797.7
λ_{res} water, (nm)	687.8	743.43	799.6
λ_{res} shift from air to water, (nm)	6.58	8.23	1.9
λ_{res} shift from water to 10 % glicole, (nm)	0.3	0.4	
Intensity difference, (a.u.)	0.0294	0.0308	0.0609
Sensitivity, (nm/RIU)	24.8	32.46	
Sensitivity, (I/RIU)	0.18	0.1981	0.32
λ highest sensitivity, (nm)	537.24	781.85	528.41

	Sample 4	Sample 5
λ_{res} air, (nm)	739.3	811.78
λ_{res} water, (nm)	746.5	814.09
λ_{res} shift from air to water, (nm)	7.17	2.31
λ_{res} shift from water to 10 % glicole, (nm)	0.4	0.2
Intensity difference, (a.u.)	0.0092	0.0151
Sensitivity, (nm/RIU)	22.3	17.85
Sensitivity, (I/RIU)	0.0974	0.0909
λ highest sensitivity, (nm)	573.8	528.41

From the bulk measurements we understood that dimensions strongly influence the sensing performances. For the gold samples the height was kept constant, and we observe an higher sensitivity for the sample with the larger diameter (150 nm); for silicon instead it seems like there's a trade-off between the height and the diameter of the disks. The samples with the smaller thickness (114 nm) result in resonance peaks not well determined, and the same applies for samples with the larger thickness and diameter ($d=200$ nm, $t=200$ nm). In the first case the visible resonances are around 300 nm while in the second case the resonance of the lowest energy mode is near 900 nm, near to the limit of the spectrometer, which makes the measurement not easy and noisy. The best samples for silicon then results the intermediate ones, which means the samples with $t=144$ or 200 nm and $d=150$ or 170 nm. Despite the better performances of some samples with respect to others, the silicon always results in a worse behaviour, with respect to gold. This is visible not only from the different sensitivity values, calculated at the lowest energy resonance peak, but also from the color plots. In those cases the color scale is the same, and it results clear that gold results more sensitive even when looking at intensity.

4.4 Local sensing

After the bulk sensing we decided to perform local sensing. To do so we changed the refractive index just near the surface of the sample as explained in *Chapter 3*. For both gold and silicon we decided to monitor the shift of the resonance wavelength of the lowest energy mode. The peak shift can be seen in fig. 4.22.

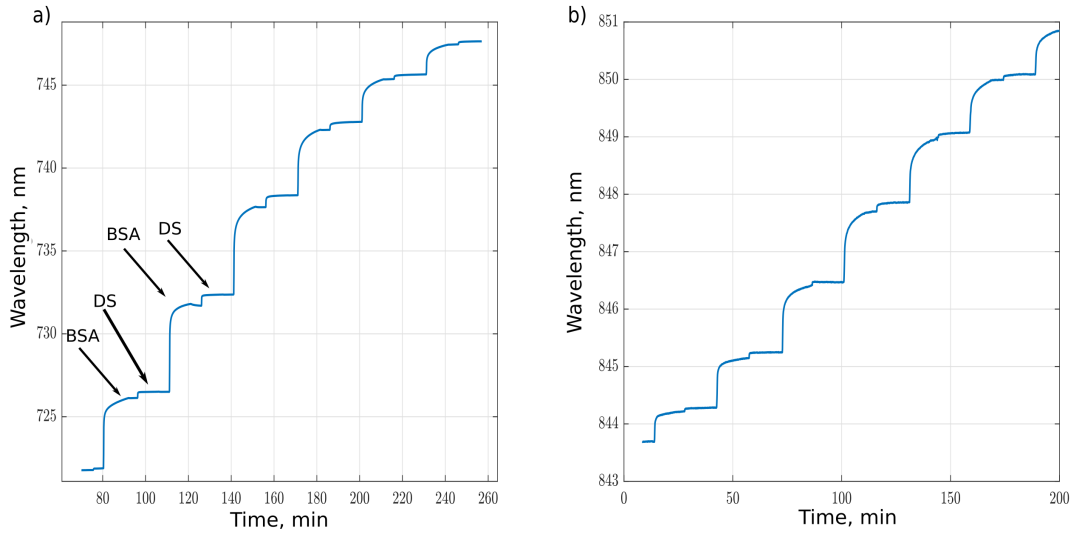


Figure 4.22: Shift of the lowest energy resonance peak as a function of time, when growing different BSA layers. The number of steps corresponds to the number of grown layers. a) Gold nanodisk $d=150$ nm b) Silicon nanodisk $d=170$ nm, disk height = 200 nm.

From the image we can recognize different steps, that correspond to the growth of a new BSA layer. The shift of the resonance wavelength can be clearly monitored for both the structures, even if they result higher for the gold sample.

We can also recognize a small shift in the resonance wavelength when the sample is washed with the DS solution. This is not surprising: the DS solution in fact, provides slightly negative charged molecules, which adsorb to the slightly positive charged BSA proteins to prepare the surface to the growth of a new BSA layers. The addition of molecules slightly increases the surface refractive index, which results in the small resonance wavelength shift. An interesting aspect of this measurement is that, even if the shift results larger for the gold sample, at the same time it seems to saturate faster with respect to what can be seen for the silicon sample. In figure 4.23 we can see an exponential fit of the resonance wavelength with respect to the number of grown layers.

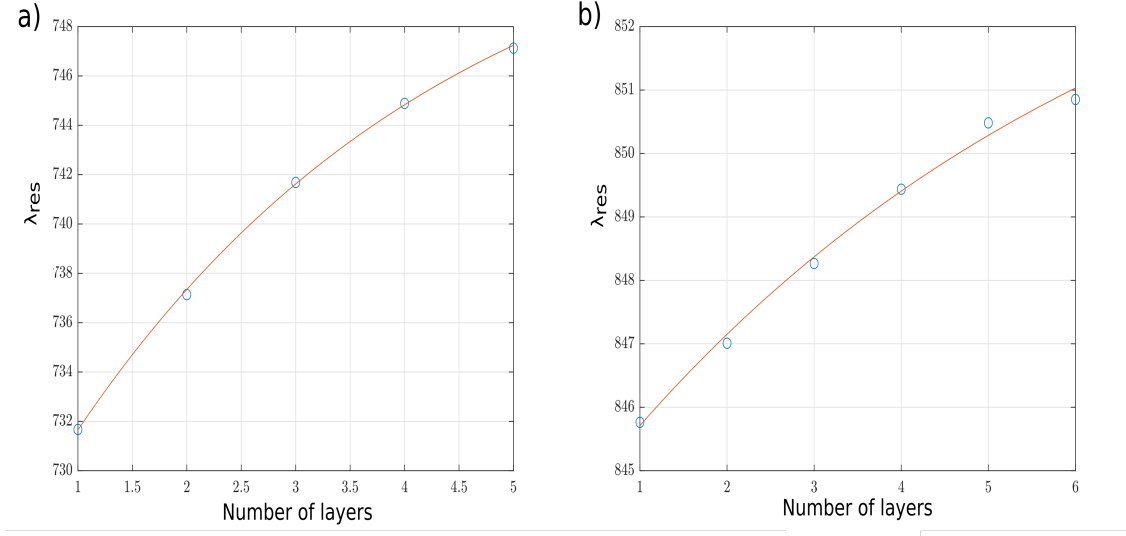


Figure 4.23: Exponential fit of the resonance peak wavelength as a function of number of BSA layers. a) Gold nanodisk $d=150$ nm b) Silicon nanodisk $d=170$ nm, disk height = 200 nm.

we fit with an exponential function of the form:

$$f(x) = A(1 - be^{-cx}) \quad (4.4)$$

where x is the number of layers. For the fit, the value of the resonance wavelength at the first layer was excluded since the BSA adsorbed directly on the samples' surface exploit different properties with respect to the ones adsorbed on the previously grown BSA monolayers [25].

The parameters in which we are more interested are A and c : c refers to the field decay, which means that the higher is that number, the nearer to the particle surface we need to be to be more sensitive, while A represents the value at which the wavelength shift saturates. In the previous subsection, we have seen both the intensity and the wavelength of the lowest energy mode change linearly with the variations of the environment refractive index. To check A then, we can extrapolate from the bulk sensing experiment the shift of the resonance wavelength that we would expect for a refractive index $n \simeq 1.5$, which is the refractive index value assumed for the BSA.

The values of the parameters of interest can be seen in the table above.

	Gold	Silicon
A	754.5	855.2
c	0.2867	0.1645

As expected looking at the shift of the resonance wavelength in fig. 4.22, the parameter c , is higher for the gold sample. This is a non intuitive results, since as seen in *Chapter 2*, the electric field in the silicon is expected to be concentrated in the internal part of the disks, while for gold the electric field results concentrated at the surface of the disk, suggesting that the surface sensitivity of gold should be higher. This result could open a real discussion

in the comparison between gold and silicon for biosensing application.

As said before we wanted to check if there is an agreement between the parameter A and the results obtained in the bulk sensing experiment. For gold, the prediction extrapolated from the bulk sensing agree with the local sensing experiment: changing the refractive index from 1.33 (DI water) to 1.5 (BSA), the bulk sensing predicts a shift of the resonance wavelength of 30 nm and from the exponential fit, when the number of layers (x) tends to infinity we expect a shift of 33 nm.

For the silicon sample we don't have such a good agreement, since from the local sensing we find an expected shift of $\simeq 10\text{ nm}$ while from the bulk sensing we would expect a total shift of just 4 nm.

Conclusion and outlook

In the previous chapter the results have been presented and discussed. We'll present now a summary of the performed experiments trying to put these results in a larger context to underline what knowledge they can bring in the present research field. Additionally, we will present some possible outlooks and further work that could be performed to go deeper in the knowledge and possible applications of sensing platforms based on high index dielectric materials.

5.0.1 Summary and conclusions

In this master's thesis the fabrication of a refractometric sensing platform was realized together with the optical setup used to study its performances. We were interested in the comparison between a sensing platform based on materials exploiting different physical properties. We chose gold, which supports plasmon resonances and silicon, which instead support the so-called mie or geometrical resonances. The property monitored during the experiments was the extinction of the samples, and this was possible with a transmission optical setup. The core of refractometric sensing is the change in the optical response of the samples, when the refractive index of the samples' surrounding environment changes. To do so together with the optical setup, we used a microfluidic setup. PDMS was used to build microchannels, then attached to the samples. This allowed us to flow solutions with different refractive indexes, and to study the induced variations in the extinction.

The performed experiments were two: a bulk sensing one, in which with solutions of ethylen glycole at different concentrations we changed the hole surrounding medium's refractive index, and a local sensing one. In the latter, flowing a solution of BSA, we were able to change the refractive index just near the surface's of the nanodisks, growing several proteins monolayers. In order to compare the two platforms, we decided to track both the wavelength at which the lowest energy resonance occur and the intensity related to the peak. We tracked the shifts of these two parameter in relation to the variations of the refractive index. As previously discussed in order to enhance the precision of the

measurements, we decided to use not just a fit of the peak position, but a centroid calculation of the latter [7]. The main results on this thesis relate to the continuous measurements of spectroscopic properties. The first result we got from these measurements is that high index dielectric nanoparticles, like silicon, can effectively be used as a sensing platform: we were able in fact, to detect variations both in the intensity and in the resonance wavelength. In the bulk sensing experiment, we were able to observe the expected decrease in intensity due to the increase of the refractive index, but also a shift of the resonance wavelength, which seemed almost null in the simulations shown in *Chapter 2*. Despite this, we found, as expected, that the performances depends on the dimensions of the nanoparticles. We fabricated samples with four different diameters of 100,150,170 and 200 nm each for three thicknesses of 114,144 and 200 nm. What we found is that the samples with the lowest diameter and thickness give rise to an extinction spectrum in the blue wavelength range, which usually present a single broaden peak. In that case a good measure was not possible. The same applies with those sample with the biggest diameter and thickness. In this case the lowest energy peak falls in the near infrared region, near to the detection limit of the used spectrometer, which resulted in an unprecise and noisy measurement. We understood then that the samples giving the best performances were the one with a 144 nm thickness and a diameter ranging from 150 to 200 nm, or the ones with a thickness of 200 nm and a diameter ranging from 150 to 170 nm. Also the measurements performed on the metallic nanoparticles showed that the performances depends on the dimensions of the nanodisks. In our case the best performances were the one of the sample with a diameter 150 nm. There's a lot of literature about plasmonic nanosensors, which enlightes how it is possible to engineer these structures to enhance the sensitivity of the device and which presents different applications [16],[14],[27]. Despite this positive result, it is clear that the gold-based sensor present a far higher sensitivity with respect to the silicon-based one. This is true both when tracking the resonance wavelength shift and the intensity shift. Performing the local sensing experiment, interesting results were found. As expected from the bulk sensing one, the variations in the resonance wavelength result bigger for the gold sample. What is interesting is that these variations seem to saturate faster for the gold sample, this actually suggests that Silicon is more sensitive.

5.0.2 Outlooks

Even if we found that for our simple system, based on a nanodisk geometry, gold nanoparticles lead to a higher sensitivity, we found that Silicon can be used for refractometric sensing. This result is in our opinion interesting enough to open the way for further investigations on high index dielectric materials for sensing purposes. First of all further investigations on different geometries and structures can be performed, leading to an engineering of the sensing platform, as it has been done for plasmonic platform. With respect to plasmonic sensor platform in fact, there's not much literature on the engineering of HID materials for sensing purposes, which could allow to better performances and enhanced sensitivity. In this project we decided to focus on the lowest energy peak when analyzing the silicon samples. Anyway analyzing the data we saw that high sensitivities were reached also near the quadrupolar mode, when this is present. We also noticed that usually the highest variations in intensity, both for gold and silicon, do not occur exactly at the resonance wavelength,

but along the shoulder of the peak. Further studies could be then performed on the different peaks presented by the sample, which could lead to higher sensitivity. Even if the data linked to these kind of materials are less with respect to plasmonic there are already some examples in which similar experiments have been performed [30],[17]. It seems that using more complicated geometries with respect to nanodisks, similar or higher sensitivities with respect to plasmonic-based sensors could be achieved. In this case, high index dielectric materials could represent a suitable alternative to plasmonic ones. This could lead to an overcome of the problems linked to plasmonic, like particles' reshape or dissipative losses which translates in Joule heating. It has to be said that not in all sensing experiments the temperature is a problem. In this project for example we used as source an halogen lamp, and the spectra were collected when flowing the solutions. This is enough to assume that we were not significantly heating the sample. Furthermore often the fabrication of exotic geometries is expensive, since requires e-beam lithography, usually more expensive than the fabrication process that can be used for nanodisks fabrication (HCL). We think anyway that the obtained results are interesting, mostly thinking about biosensing where heat can be really detrimental.

In this sense further experiments need to be performed in order to clear out some ambiguities.

Bibliography

- [1] Colin J. Alleyne et al. “Numerical method for high accuracy index of refraction estimation for spectro-angular surface plasmon resonance systems”. In: *Optic express*, Vol. 16, No. 24 (2008).
- [2] Neil W. Ashcroft and N. David Mermin. *Solid state physics*. 1976.
- [3] Craig F. Bohren and Donald R. Huffman. *Absorption and scattering of light by small particles*. 1998.
- [4] Myfab LIMS Chalmers. *Ebeam resist MCC NANO 950k PMMA A4*. URL: <http://www.myfab.se/Chalmers/UserInformation/tabid/66/Default.aspx?topic=Ebeam+resist+MCC+NANO+950k+PMMA+A4>.
- [5] Yonzon CR. et al. “A comparative analysis of localized and propagating surface plasmon resonance sensors: the binding of concanavalin a to a monosaccharide functionalized self-assembled monolayer.” In: *Journal of the american chemical society*, 126(39):12669-76 (2004).
- [6] C.Thirstrup and W.Zong. “Data analysis for surface plasmon resonance sensors using dynamic baseline algorithm”. In: *Sensors and Actuators B: Chemical Volume 106, Issue 2, 13 May 2005, Pages 796-802* (2004).
- [7] Andreas B. Dahlin, Jonas O. tegenfeldt, and Fredrik Höök. “Improving the Instrumental Resolution of Sensors Based on Localized Surface Plasmon Resonance”. In: *Analytical Chemistry*, 78, 4416-4423 (2006).
- [8] Javier Garcia de Abajo. *Nanophotonics*. URL: www.nanophotonics.es/widgets.
- [9] J. Cao et al. “Comparison of Surface Plasmon Resonance and Localized Surface Plasmon Resonance-based optical fibre sensors”. In: *Journal of physics: Conference series 307 012050* (2011).
- [10] Hans Fredriksson et al. “Hole–Mask Colloidal Lithography”. In: *Advanced materials*, 19, 4297–4302 (2007).
- [11] Adrián Fernández Gavela et al. “Last Advances in Silicon-Based Optical Biosensors”. In: *Sensors*, 16, 285 (2016).

- [12] Guillermo Gonzalez-rubio, Andres Guerrero-Mart ínez, and Luis M. Liz-Marzañ. “Reshaping, Fragmentation, and Assembly of Gold Nanoparticles Assisted by Pulse lasers”. In: *Accounts of chemical research*, 49, 678-686 (2016).
- [13] J. Homola. “Surface Plasmon Resonance Based Sensors”. In: *Springer-Verlag, Berlin-Heidelberg-New York* (2006).
- [14] Eliza Hutter and Janos H. Fendler. “Exploitation of Localized Surface Plasmon Resonance”. In: *Advanced materials*, 16, No.19 (2004).
- [15] Saman Jahani and Zubin Jacob. “All-dielectric metamaterials”. In: *Nature nanotechnology* (2016).
- [16] Hyeon-Ho Jeong et al. “Dispersion and shape engineerer plasmonic nanosensors”. In: *Nature communications* (2016).
- [17] Alex Krasnok et al. “Spectroscopy and Biosensing with Optically Resonant Dielectric Nanostructures”. In: *Advanced optical materials* (2018).
- [18] Arseniy I. Kuznetsov et al. “Optically resonant dielectric nanostructures”. In: *Science* 354 (6314), aag2472 (2016).
- [19] Stefan A. Maier. *PLASMONICS: FUNDAMENTALS AND APPLICATIONS*. 2007.
- [20] Christian Mätzler. *MATLAB Functions for Mie Scattering and Absorption*. 2002. URL: <https://omlc.org/software/mie/maetzlermie/Maetzler2002.pdf>.
- [21] Christian Mätzler. *Mie matlab*. URL: <https://scattport.org/index.php/programs-menu/mie-type-codes-menu/111-mie-matlab-maetzler>.
- [22] Yavas O. et al. “On-a-chip Biosensing Based on All-Dielectric Nanoresonators”. In: *Nanoletters* (2017).
- [23] University of Cambridge. *The Scanning Electron Microscope (SEM)*. URL: <https://www.eng-atoms.msm.cam.ac.uk/RoyalSocDemos/SEM>.
- [24] MEgloba Group of Companies. *Ethylen glycol, product guide*. 2008.
- [25] Marek Piliarik et al. “High-resolution biosensor based on localized surface plasmons”. In: *Optics express* (2012).
- [26] Wei Qian et al. “Ultrafast electronic and lattice processes of plasmonic nanoparticles of different shape”. In: *Fundamental Ultrafast Processes in Chemistry, Physics, and Biology, Pages 260-273* (2006).
- [27] Barizuddin S., Bok S., and Gangopadhyay S. “Plasmonic Sensors for Disease Detection - A Review”. In: *Journal of Nanomedicine & Nanotechnology* (2016).
- [28] Isabelle Staude and Jörg Schilling. “Metamaterial-inspired silicon nanophotonics”. In: *Nature photonics* (2017).
- [29] Frederick Wooten. *Optical properties of solids*. 1972.
- [30] Jiahao Yan et al. “New type high-index dielectric nanosensors based on the scattering intensity shift”. In: *Nanoscale*, 8, 5996 (2016).
- [31] Qian Zhao et al. “Mie resonance-based dielectric metamaterials”. In: *Materials today*, 12 (2009).